Electromagnetic Modeling and Experimental Evaluation of Plasmon-Based Molecular Sensors

Wei-Yin Chien

Photonic Systems Group
Department of Electrical and Computer Engineering
Faculty of Engineering
McGill University

June, 2008

Under the joint supervision of Professors
Andrew G. Kirk and Thomas Szkopek

A thesis submitted to McGill University in partial fulfilment of the requirements of the degree of Master of Engineering

Abstract

The advances in nanoscience and nanotechnology in recent decades have renewed the interests in the optical properties of metals. Today, the field known as Plasmonics studies the control and manipulation of the electromagnetic near-fields of metallic nanostructures in order to realize novel subwavelength optical applications.

In particular, this thesis explores the phenomenon of plasmon resonance for molecular sensing. Surface plasmon resonance (SPR) on flat metal surfaces is used for index-of-refraction sensing and localized surface plasmon resonance (LSPR) on metal nanospheres can produce surface-enhanced Raman scattering (SERS).

The operation principles and the experimental evaluation of two SPR sensing devices are presented. An integrated sensor and a 2D wavelength-angle modulated version were estimated to have an angular sensitivity of 126°/RIU and 91°/RIU, respectively. Furthermore, through an implementation of a full vector multiple-multipole light scattering method, useful for the calculations of the field focusing efficiency between assemblies of metal nanospheres, we showed that optical frequency electric fields can be enhanced in gold nanoparticle assemblies by an order of 450 in nanometer volumes.

Keywords: surface plasmons, plasmonics, optical biosensors, surface-enhanced Raman scattering, optics of metals, nanophotonics, nanomaterials, classical electrodynamics

Sommaire

L'avancée des nanosciences et de la nanotechnologie au cours des dernières décennies a suscité un renouvellement de l'intérêt pour les propriétés optiques des métaux. Aujourd'hui, la Plasmonique cherche à contrôler les champs proches électromagnétiques des nanostructures métalliques afin de bénéficier des nouvelles applications reposant sur l'optique de sous-longueur d'onde.

En particulier, ce mémoire explore l'utilisation de la résonance à plasmons pour la capture des molécules. L'étude se divise en la résonance à plasmons de surface (SPR) pour des surfaces métalliques planes et pour des nanosphères métalliques. Ces deux méthodes permettent de créer des capteurs sensibles aux variations d'indice de réfraction et d'autres qui reposent sur des effets non-linéaires tels que la diffusion Raman exaltée de surface (SERS).

Suite à l'introduction des bases, l'opération ainsi que des résultats expérimentaux de deux capteurs à plasmons de surface sont présentés. Un capteur intégré et une version 2D avec modulation de longueur d'onde et de l'angle possèdent une sensibilité angulaire d'environ 126°/RIU et 91°/RIU, respectivement. Par la suite, la réalisation de la méthode du multiple-multipole, utile pour évaluer l'efficacité de la concentration des champs entre des nanosphères métalliques, est discutée. Une amélioration de la concentration de champ optique de l'ordre de 450 par des nanospheres d'or est présentée.

Mots-clés: plasmon de surface, plasmonique, biocapteurs optiques, diffusion Raman exaltée de surface, optique des métaux, nanophotonique, nanomatériel, électro-dynamique classique

Acknowledgements

This research work would not have been possible without the support and encouragement of many people.

First of all, I wish to acknowledge the efforts of my supervisors, Professors Andrew G. Kirk and Thomas Szkopek, who shared many of their valuable wisdoms and their erudite knowledge during the pursuit of the research objectives. They made this work a pleasant, dynamic and intellectually stimulating experience. Specifically, I would like to thank Professor Kirk for his helpful guidance and frequent jokes during the group meetings. In the same manner, I would also like to thank Professor Szkopek for his endless physical insights and funny anecdotes.

Special thanks are dedicated to many of the members of the Photonic Systems Group who willingly lent me a hand when I needed, namely Chris Rolston, Colin Alleyne, Muhammad Zeeshan Khalid, Xuyen Dai Hoa, Dr. Guilin Sun, Michael Ménard, Bhavin Shastri and Dr. Odile Liboiron-Ladouceur.

Last but not least, I wish to extend my gratitude to my parents, my brother, my fiancée and her parents for their continuous encouragement, patience and perspicacity during the darker periods and their strong beliefs in my ideologies.

As for the financial assistance, this work was supported by Le Fonds québécois de la recherche sur la nature et les technologies (FQRNT), the Canadian Institute for Advanced Research (CIFAR) and a Max Stern Recruitment Fellowship from the Graduate and Postdoctoral Studies Office (GPSO) of McGill University.

Table of Contents

Chapter 1 – Introduction

1.1 Motivation

The British Museum, located in London, holds one of the most spectacular and unusual examples of optical effects produced by ancient glass artisans. The beautifully crafted Lycurgus Cup [1.1], depicting the death of Lycurgus, a king of the Thracians from Homer's *Iliad* [1.2], contains striking shades of bright red and dark green when illuminated by a white light source from behind. Dating from the fourth century A.D., the scientific explanation of why the same material shows varying colours at different spots when illuminated remained a mystery until recently. In the late 1980s, after the analysis carried out by Barber and Freestone using transmission electron microscopy and X-rays, it was found that the noticeable changes in colour are due to the plasmonic excitation of gold-silver alloy nanoparticles embedded in the glass [1.3]. In fact, the colour changes of the goblet result from light absorption and scattering occurring within the glass material; the green and blue light absorbed by smaller nanoparticles yields a reddish colour upon transmission whereas larger particles scatter for the most part in the green portion of the visible spectrum [1.4].

Obviously, the Roman glassmakers did not have much knowledge of electrodynamics nor nanofabrication infrastructure. Today, with advancements in controlled deposition of thin metallic films and synthesis of metallic nanoparticles, it is easy to excite **surface plasmons** [1] (or strictly speaking, surface plasmon-polaritons [1.5]), these collective charge density (plasma) oscillations confined to the surface of metallic nanostructures or nanoparticles. It is also possible to tailor their properties such as their particular nanoscale optical fields to alter light-matter interactions for subwavelength optical applications. For instance, much effort has been and is currently devoted to the investigation of plasmonic waveguides, ultra dense data storage, sensing, metamaterials, etc [1.6-1.8].

[1] In the language of Solid State Physics, the term **plasmon** refers to the quantum associated with a plasma oscillation (as a photon is the quantum unit of an electromagnetic oscillation).

In particular, surface plasmons are interesting for their applications in molecular sensing as the need for high sensitivity and selectivity molecular sensors is growing in the health care, pharmaceutical and environmental communities. There are currently great interests for sensors that act as portable or "lab-on-chip" devices that can be used by moderately trained individuals outside the laboratory environment or laboratory-based platforms for high-throughput of parallel screening of multiple analytes that may be present in very low concentrations. Plasmon-based molecular sensors offer great potentials for achieving these goals [1.9-1.10].

1.2 Scope of this Thesis

My research work is focused on the exploitation of plasmonic resonance for optical molecular sensing purposes, at the physical level. My study involves two sensing modalities and can be divided as follows: (a) experimental work with surface plasmon resonance (SPR) biosensors and (b) electromagnetic modeling of plasmonic resonances in metal nanoparticles for surface-enhanced Raman scattering (SERS). The plasmon resonances for biosensing supported on a planar surface and on metallic nanospheres are illustrated respectively in Fig. 1.1 (a) and Fig. 1.1 (b).

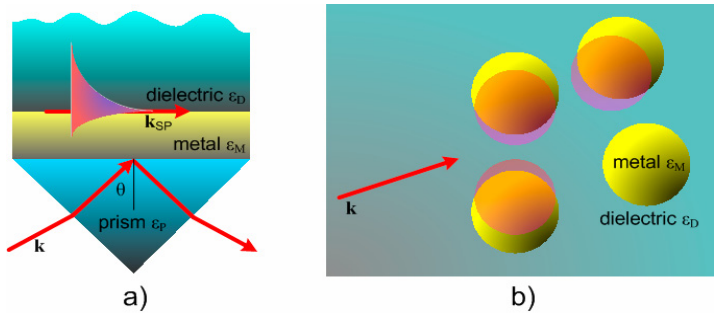

Figure 1.1 - Plasmonic effects for biosensing : (a) SPR supported on thin film, useful in SPR sensors for measuring bioaffinity reactions; (b) localized SPR (LSPR) supported on metallic nanospheres can produce surface-enhanced Raman scattering (SERS) for molecular fingerprinting.

SPR biosensing is a commercialized technique that detects molecular binding events by monitoring changes in refractive index. Following the need for fast, label-free, compact and cost effective sensitive sensing devices, two SPR sensors have been under

development with Kirk's group [1.11]. The first sensor is previously designed and fabricated to be a low-cost, disposable, and mass produced solution [1.12]. One of my tasks is to characterize this highly integrated biosensor containing microfabricated focusing diffractive optical elements (Chapter 4.3). The second sensor is intended to demonstrate enhanced sensitivity using periodic metallic structures as compared to that of conventional flat metallic films and was previously investigated theoretically by Alleyne et al. [1.13]. A part of my work was to assist the construction of the device from the ground up, which involved the assembly of light emitting components, optomechanical positioning stages and other passive elements in order to exploit the plasmonic effect for biomedical purposes (Chapter 4.4). Both tasks required experimental work at the Photonic Systems Group Laboratory.

In addition to the effort spent on SPR biosensors, I also explored a different sensing approach on the theoretical level using plasmon resonance supported by metal nanoparticles to efficiently couple far-field radiation to nanometer scale volumes, thereby producing localized optical fields. These enhancements can produce non-linear effects such as the surface-enhanced Raman scattering (SERS), commonly employed in ultrasensitive light scattering probes. An important issue in SERS is how metal particles should be arranged to produce the largest field enhancement. Various structures have shown promise (Chapter 2.3) with the advent of nanofabrication abilities (such as DNA mediated construction of discrete metallic nanostructures from the Sleiman group at McGill's Department of Chemistry [1.14]) and more powerful computing facilities. However, there is a lack of comparison between different near-field focusing structures and most descriptions have recourse to quasi-static approximation that is insufficient when coupling between particles is strong. In this light, I implemented a self-consistent full vector electromagnetic numerical code that simulates light scattering in metallic nanosphere assemblies (Chapter 5). The simulation that includes plasmonic variation on metal surfaces involves attempts to model optimal optical field focusing, as a mean to systematically design efficient couplings of far-field radiation to nanometer scale volumes.

1.3 Original Contributions

At the time of writing this thesis, my contribution to the field is: in the context of SERS, I have performed the first full electromagnetic simulation of a variety of nanoparticle assemblies for efficient field focusing. This involved a systematic comparison of the far and near-field optical response between various nanosphere assemblies arranged in linear chains, self-similar series and in discrete approximations of the truss, cone and tetrahedron [1.15] (Chapter 5).

1.4 Organization of this Thesis

The thesis is organized in the following manner. Chapter 2 is a comprehensive literature review on exploitation of plasmonic effects in biosensing. Chapter 3 provides the background knowledge of optical properties at metal-dielectric interfaces as described by classical electrodynamics, necessary for the appreciation of the subsequent chapters. Chapter 4 describes my involvement with SPR biosensors whereas Chapter 5 provides the detailed documentation of the metallic nanosphere light-scattering code implementation. These two chapters can be read separately in any order without loss of continuity. At last, Chapter 6 presents a summary of this thesis and concludes with future research directions. In Appendix A, the importance of evanescent near-fields is briefly explained.

1.5 References

[1.1] I. Freestone, N. Meeks, M. Sax, and C. Higgitt, "The Lycurgus Cup - A Roman Nanotechnology," *Gold Bulletin*, vol. 40, no. 4, pp. 270-277, 2007.

[1.2] Samuel Butler, ed., *The Iliad of Homer* (Classic Publishers, 1923).

[1.3] D.J. Barber and I.C. Freestone, "An investigation of the origin of the colour of the Lycurgus Cup by analytical transmission electron microscopy," *Archaeometry*, vol. 32, pp. 33-45, 1990.

[1.4] L. Novotny and B.Hecht, *Principles of Nano-Optics* (University Press, Cambridge, 2006).

[1.5] E. Burstein and F. de Martini, ed., *Polaritons* (Pergamon Press, London, 1974).

[1.6] W.L. Barnes, A. Dereux, and T.W. Ebbesen, "Surface Plasmon Subwavelength Optics," *Nature*, vol. 424, pp. 824-830, 2003.

[1.7] E. Ozbay, "Plasmonics: Merging Photonics and Electronics at Nanoscale Dimensions," *Science*, vol. 311, pp. 189-193, 2006.

[1.8] J.R. Lakowicz, "Plasmonics in Biology and Plasmon-Controlled Fluorescence," vol. *Plasmonics*, vol. 1, pp. 5-33, 2006.

[1.9] T.A. Klar, "Biosensing with plasmonic nanoparticles," in *Nanophotonics with Surface Plasmons*, V.M. Shalaev, and S. Kawata, ed. (Elsevier, 2007), pp. 219-270.

[1.10] J. Homola, ed., *Surface Plasmon Resonance Based Sensors* (Springer-Verlag, Berlin, 2006).

[1.11] X.D. Hoa, A.G. Kirk, and M. Tabrizian, "Towards integrated and sensitive surface plasmon resonance biosensors: A review of recent progress," *Biosensors and Bioelectronics*, vol. 23, pp. 151-160, 2007.

[1.12] M.Z. Khalid, *A highly integrated Surface Plasmon Resonance Sensor based on a Focusing Diffractive Optic Element* (Master's thesis, McGill University, 2007).

[1.13] C.J. Alleyne, A.G. Kirk, R.C. McPhedran, N.-A.P. Nicorovici, and D. Maystre, "Enhanced SPR sensitivity using periodic metallic structures," *Optics Express*, vol. 15, pp. 8163-8169, 2007.

[1.14] F.A. Aldaye, H.F. Sleiman, "Dynamic DNA Templates for Discrete Gold Nanoparticle Assemblies: Control of Geometry, Modularity, Write/Erase and Structural Switching," *J. Am. Chem. Soc.*, vol. 129, pp. 4130-4131, 2007.

[1.15] W.-Y. Chien, T. Szkopek, "Multiple-multipole simulation of optical near-fields in discrete metal nanosphere assemblies," *Optics Express*, vol. 16, pp. 1820-1835, 2008.

Chapter 2 – Literature Review

2.1 General Plasmonics

The interest in surface modes dates back a century ago, to the pioneering works carried by Zenneck [2.1], Mie [2.2] and Sommerfeld [2.3]. In 1907 and 1909 respectively, Zenneck and Sommerfeld studied surface radio waves confined near the ground. Their contemporary, Mie, formulated in 1908 a full vector electromagnetic theory for the modes of a single sphere. Later, in the 1950s, Ritchie [2.4] investigated electromagnetic properties at flat conductor-insulator interfaces. At first, the surface modes were extensively studied only for their fundamental physical properties as is presented by Raether [2.5], Kreibig and Vollmer [2.6], Boardman [2.7], Bohren and Huffman [2.8]. However, by the third quarter of 20th century, analytical chemists started to recognize the potentials of surface plasmons in sensing and the attention has temporarily moved from the physics to analytical chemistry communities [2.9].

Since the electromagnetic fields of the surface plasmon modes decay exponentially from a surface, they cannot be directly observed using conventional far-field measurements. The visualization of the near-fields at proximity of object surfaces and advanced studies of the modes such as their localization, scattering, propagation and interference properties had to wait until the development of scanning near-field optical microscopes (SNOM) [2.10-2.16]. In recent decades, revival of interests in the optics communities is mainly due to the advances in modern nanoscale surface characterization methods such as SNOM, along with nanofabrication techniques such as electron-beam lithography and self-assembly [2.17]. The appearances of faster computers with larger memory capacity that allow for more accurate electromagnetic simulations prior to nanostructure fabrication also contributed largely.

Along with the biosensing applications that have already started to arise, much effort has also been directed to miniaturization of photonics devices and integration with

electronics in the sub-100-nm-size regime [2.18]. The reason is that the integration of electronics and photonics circuitries has traditionally been limited by their respective dimension. Electronic interconnects have already been scaled down to sub-micron size while many photonic devices (for example, lenses, fibers, directional couplers, etc.) still rely on working principles that prohibit subwavelength operations. The minimum size of photonic devices is limited when dielectric waveguides are used.

Today, the designation "plasmonics" has been proposed [2.19] for all the researches in nanophotonics that involve manipulation of these highly localized surface modes. The field now comprises a variety of experts, ranging from physicists, chemists, engineers, material scientists to biologists. In fact, the number of researches in this field has increased tremendously, especially in recent years. However, we will from here on solely discuss two sensing modalities: surface plasmon resonance (SPR) and the localized surface plasmon resonance (LSPR) that is confined on metallic nanoparticles for non-linear optical enhancement applications such as surface-enhanced Raman scattering (SERS).

2.2 Surface Plasmon Resonance Sensors

In the late 1960s, Kretschmann [2.20] and Otto [2.21] demonstrated the excitation of surface plasmons by coupling configurations named after them. Their setups are shown in Fig. 2.1 below.

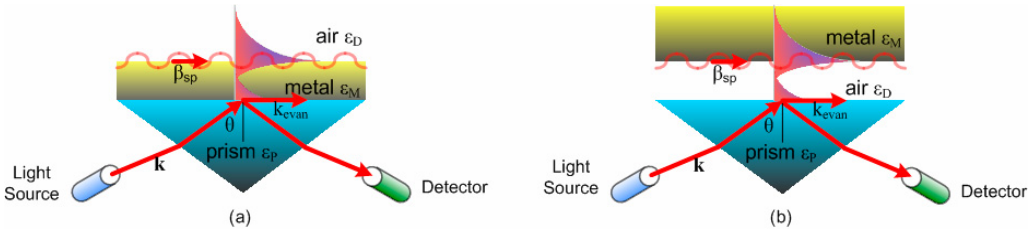

Figure 2.1 – Excitation of surface plasmons (a) Kretschmann and (b) Otto configurations.

Their attenuated total reflection (ATR) approaches provided a method to increase the incident free-space photon momentum and to measure the reflected intensities (Chapter 4). The Kretschmann's prism coupling scheme is more experimentally convenient than

Otto's because of the difficulty for accurately maintaining a subwavelength air gap between the interfaces in the latter case. The prism coupling altogether with other coupling techniques such as diffraction grating or waveguide form the essential methods for the excitation of surface plasmons (Chapter 4.2).

Shortly later, in the 1970s, the use of surface plasmon resonance (SPR) to characterize thin films [2.22] and monitor electrochemical processes at metal surfaces [2.23] was recognized because the coupling condition is highly sensitive to refractive index changes. In 1982, Nylander and Liedberg et al. demonstrated the use of SPR for gas detection and biosensing [2.24, 2.25]. Since then, many other implementations of SPR sensors have emerged and can be classified by their coupling or modulation schemes (angular or spectral).

A SPR sensor based on prism coupling and angular modulation was reported in 1988 by Matsubara et al. [2.26]. Their optical imaging system involved the use of low-cost light emitting diode (LED), a few spherical lenses and a photodiode array detector positioned in the back-focal plane. A few years later, many sensors with improved index-of-refraction resolution have shown their faces [2.27-2.29]. A notable incremental change in these implementations is the use of cylindrical lenses to allow multiple sensing channels. The improved optical systems were then commercialized by Biacore in 1990 [2.30].

Following the trend of monolithic integration to achieve compactness, improve performance and allow mass-production, commercialization of highly integrated sensors was forwarded by Spreeta [2.31]. Later, Thirstrup et al. [2.32] presented an integrated implementation containing diffractive optical coupling elements. In this system, two chirped diffraction gratings focus the incoming light on the sensing spots and subsequently on the detector plane. In this light, the monolithically integrated SPR sensor in Kirk's group that uses only one focusing diffractive optical element was designed and fabricated [2.33, 2.34]. Several other wavelength interrogation systems and

intensity modulation also exist [2.35, 2.36]. There are fiber-optic SPR sensors [2.37] and few other integrated optical waveguide ones [2.38, 2.39] as well.

SPR sensors based on surface plasmons excited on the surface of metallic diffraction gratings have also been reported [2.40], although not as much as prism coupler based ones. The periodic textured metal surface allows the enhancement of sensitivity [2.41], the addition of wavelength division multiplexing (WDM) [2.42] and incorporation of recent optical phenomena such as photonic bandgap [2.41, 2.43]. A combined wavelength-angular modulation scheme has been theoretically investigated by Alleyne et al. [2.41].

2.3 Surface-Enhanced Raman Scattering

The discovery of the Raman effect took place in 1928 [2.44]. In Raman scattering, the shift between the incident and the inelastically scattered light is caused by the vibrational, rotational or electronic states of a molecule. This phenomenon is widely used in Raman spectroscopy to identify chemical structure within a given sample. However, this light-matter interaction is extremely weak and an enhancement of such effect is highly desired [2.45]. In fact, the chemical structural information provided by Raman spectroscopy and the high sensitivity of fluorescence are combined in a novel spectroscopy that employs surface-enhanced Raman scattering (SERS). In the late 1970s and early 1980s, the cause which results in such an enhancement has been studied in further depth [2.46, 2.47]: SERS is an enhancement of Raman scattering due in large part to enhancement of local electric fields. It is now known that the Raman scattered optical power due to SERS scales with the fourth power of local electric field enhancement [2.48].

The role played by plasmons is first pointed out by Moscovits [2.49]. Plasmon resonance in metal nanostructures provides one means to efficiently couple far-field radiation to nanometer scale volumes, at a so-called “hot-spot”, to produce a localized electric-field. For this reason, the question of how metal particles should be arranged with respect to each other to produce the strongest field enhancement at the “hot-spots”

remains an important one. Various metallic nanostructures have therefore been studied for their near-fields, namely, nanorods, triangular particles, cylindrical and needle-like nanoparticles [2.50]. It is known that linear chains of silver nanoparticles provide a way to concentrate the electromagnetic field in nanoscale regions between the particles [2.51]. A more efficient field enhancing structure consists of a self-similar chain of particles with decreasing diameters and gaps [2.52]. Tapered, continuous plasmonic waveguides are a third instance of efficient nanofocusing structures [2.53]. Moreover, the local optical field can also be controlled using a dielectric core-metal shell nanoparticle [2.54].

Plasmon resonance in noble metal bispheres was measured by Reinhard et al. [2.55] to demonstrate nanometer scale distance calibration. Further, the ability to organize gold nanoparticles into discrete and well-controlled structures using programmable DNA templates [2.56] provides the possibility for rational design and synthesis of efficient near-field focusing structures for applications such as SERS.

In this part of my research work, I have simulated the optical response of discrete assemblies of nanospheres in linear, self-similar and other arrangements using a multiple-multipole technique (also known as the T-matrix method) [2.57-2.59]. The mathematical construction of the multiple-multipole method has already been established and simulations on some simple geometries have been performed [2.60-2.64]. The most relevant is the recent work by Pellegrini et al., in which metal bispheres and clusters of small spheres dressing a large sphere have been analyzed. Thus far, there has been no full electromagnetic analysis of the focusing properties of sphere assemblies explicitly designed for efficient field focusing, such as the self-similar structure. The quasi-static approximation or dipole approximation is often made in studies of light scattering by assemblies of spherical nanoparticles; Khlebtsov et al. have conclusively shown that a multipole approach is needed for accurate prediction of far-field light scattering even for simple sub-wavelength bispheres [2.65].

2.4 Relevance in Biology and Medicine

In the past few decades, remarkable advances have taken place in the fields of molecular biology and biomedical diagnostics: genomics is marked by the completion of human genome decoding in 2003 [2.66] and proteomics – the large-scale studies of proteins, especially about their structures and functions – is currently on the rise [2.67-2.69]. The post-human genome era is fuelled by even more challenging scientific ambitions: that of understanding gene-expressed proteins and their targeted reactions [2.69], molecular level disease diagnosis and drug screening [2.70], etc. In addition, in other important areas such as environmental and food safety monitoring, detection of biochemical agents with high specificity in real-time on the field is highly desired [2.71]. Scientists and engineers are thus pressured to come up with "reporters" that will be able to recognize biomolecular events at the nanoscale [2.70]. In this light, plasmon-based molecular sensors offer great potentials.

Unlike the fluorescence detection method, surface plasmon resonance (SPR) provides real-time measurements without recourse to labelling of analytes. Many attempts to apply SPR in various biological contexts have been reported: for proteomics [2.69, 2.72, 2.73], antigen-antibody interactions [2.74], DNA hybridization events [2.75], detection of polymerase chain reaction (PCR) products [2.76], as well as detection of hormones, viruses, steroids, etc. [2.77]. An overview of SPR in health related applications is given by Homola [2.71].

On the other hand, the relevance of SERS in biomedicine is no less in comparison to SPR sensing, despite of its shorter history [2.70]. In SERS, the analyte of interest is attached to the metal surfaces of some nanostructure designed to enhance the light scattering. To name a few examples, Xu et al. demonstrated the detection of molecular vibrations of hemoglobin (Hb) at a single molecule level [2.78]. Glucose sensing using SERS has also been suggested [2.79]. In 2002, Vo-Dinh, Allain and Stokes developed a Cancer gene detection scheme [2.80]. The appearances of papers related to SERS are currently increasing at an incredible pace [2.81].

Both the SPR and LSPR methods in sensing have shown to be very promising. As such, comparisons of these approaches are made by a few researchers [2.82, 2.83]. Although SPR sensors are a more mature technology, LSPR may not require elaborate optical imaging systems. Moreover, plasmonics effects are not limited to the two sensing applications mentioned above; a review paper on the combination of the two in a single improved sensing scheme, together with plasmon-controlled fluorescence, has also been made [2.84]. In addition, plasmonics has also a role to play in optofluidics, an ongoing field which merges photonics and microfluidics [2.85, 2.86].

2.5 References

[2.1] J. Zenneck, "Über die Fortpflanzung ebener elektromagnetischer Wellen längs einer ebenen Leiterfläche und ihre Beziehung zur drahtlosen Telegraphie," *Ann. Physik (4th series)*, vol. 23, pp. 846, 1907.

[2.2] G. Mie, "Beiträge zur Optik trüber Medien, speziell kolloidaler Metallösungen," *Ann. Phys.*, vol. 330, pp. 377–445, 1908.

[2.3] A. Sommerfeld, "Über die Ausbreitung der Wellen in der drahtlosen Telegraphie," *Ann. Physik (4th series)*, vol. 28, pp. 665, 1909.

[2.4] R. H. Ritchie, "Plasma Losses by Fast Electrons in Thin Films," *Phys. Rev.*, vol. 106, pp. 874, 1957.

[2.5] H. Raether, *Surface Plasmons on Smooth and Rough Surfaces and on Gratings* (Springer-Verlag, New Tork, 1983).

[2.6] U. Kreibig, M. Vollmer, *Optical Properties of Metal Clusters* (Springer, Berlin, 1995).

[2.7] A.D. Boardman, *Electromagnetic Surface Modes* (Wiley-Interscience, Toronto, 1982).

[2.8] C.F. Bohren, D.R. Huffman, *Absorption and Scattering of Light by Small Particles* (Wiley, New York, 1983).

[2.9] S.A. Maier, H. A. Atwater, "Plasmonics: Localization and guiding of electromagnetic energy in metal/dielectric structures," *J. Appl. Phys.*, vol. 98, 011101, 2005.

[2.10] R.C. Reddick, R.J. Warmack and T.L. Ferrell, "New form of scanning optical microscopy," *Phys. Rev. B*, vol. 39, pp. 767, 1989.

[2.11] D.A. Courjon, J.-M. Viroureux, M. Spajer, K. Sarayeddine and S. Leblanc, "External and internal reflection near field microscopy: experiments and results," *Appl. Opt.*, vol. 29, pp. 3734-3740 , 1990.

[2.12] P.M. Adam, L. Salomon, F. de Fornel and J. P. Goudonnet, "Determination of the spatial extension of the surface-plasmon evanescent field of a silver film with a photon scanning tunneling microscope," *Phys. Rev. B*, vol. 48, pp. 2680-2683, 1993

[2.13] D. P. Tsai, J. Kovacs, Zhouhang Wang, Martin Moskovits, Vladimir M. Shalaev, J. S. Suh and R. Botet, "Photon scanning tunneling microscopy images of optical excitations of fractal metal colloid clusters," *Phys. Rev. Lett.*, vol. 72, pp. 4149-4152, 1994.

[2.14] S.I. Bozhevolnyi, I.I. Smolyaninov and A.V. Zayats, "
Near-field microscopy of surface-plasmon polaritons: Localization and internal interface imaging," *Phys. Rev. B*, vol.51, pp. 17916-17924, 1995.

[2.15] H. Ditlbacher, J.R. Krenn, N. Felidj, B. Lampretch, G. Schider, M. Salerno, A. Leitner, F.R. Aussenberg, "Fluorescence imaging of surface plasmon fields," *Appl. Phys. Lett.*, vol. 80, pp. 404-406, 2002.

[2.16] A.V. Zayats and I.I. Smolyaninov, "Near-field photonics: surface plasmon polaritons and localized surface plasmons," *J. Opt. A: Pure Appl. Opt.*, vol. 5, pp. 16-50, 2003.

[2.17] W.L. Barnes, A. Dereux, T.W. Ebbesen, "Surface Plasmon Subwavelength Optics," *Nature*, vol. 424, pp. 824-830, 2003.

[2.18] E. Ozbay, "Plasmonics: Merging Photonics and Electronics at Nanoscale Dimensions," *Sciences*, vol. 311, pp. 189-193, 2006.

[2.19] S.A. Maier, M.L. Brongersma, P.G. Kik, S. Meltzer, A.A.G. Requicha and H.A. Atwater, "Plasmonics - A Route to Nanoscale Optical Devices,", *Adv. Mater.*, vol. 13, pp. 1501-1505, 2001.

[2.20] E. Kretschmann, H. Raether, "Radiative decay of non-radiative surface plasmons excited by light," *Z. Naturforsch.*, vol. 23A, pp. 2135–2136, 1968.

[2.21] A. Otto, "Excitation of surface plasma waves in silver by the method of frustrated total reflection," *Z. Physik*, vol. 216, pp. 298-410, 1968.

[2.22] I. Pockrand, J.D. Swalen, J.G. Gordon, M.R. Philpott, "Surface plasmon spectroscopy of organic monolayer assemblies," *Surface Sci.*, vol. 74, pp. 237-244, 1978.

[2.23] J.G. Gordon, S. Ernst, "Surface plasmons as a probe of the electrochemical interface," *Surface Sci.*, vol.101, pp. 499-506, 1980.

[2.24] C. Nylander, B. Liedberg, T. Lind, "Gas detection by means of surface plasmons resonance," *Sensors and Actuators*, vol. 3, pp. 79-88, 1982.

[2.25] B. Liedberg, C. Nylander, I. Lundström, "Surface plasmons resonance for gas detection and biosensing," *Sensors and Actuators*, vol. 4, pp. 299-304, 1983.

[2.26] K. Matsubara, S. Kawata, and S. Minami, "Optical chemical sensor based on surface plasmon measurement," *Appl. Opt.*, vol. 27, pp. 1160-1163, 1988.

[2.27] B. Liedberg, I. Lundström, and E. Stenberg, "Principles of biosensing with an extended coupling matrix and surface plasmon resonance," *Sensors and Actuators B Chem.*, vol. 11, pp. 63-72, 1993.

[2.28] S. Sjölander, C. Urbanitzky, "Integrated fluid handling system for biomolecular interaction analysis," *Anal. Chem.*, vol. 63, pp. 2338-2345, 1991.

[2.29] S. Löfas, M. Malmqvist, I. Rönnberg, E. Stenberg, B. Liedberg, and I. Lundström, "Bioanalysis with surface plasmon resonance," *Sensors and Actuators B Chem.*, vol. 5, pp. 79-84, 1991.

[2.30] "Biacore Life Sciences," http://www.biacore.com.

[2.31] J. Melendez, R. Carr, D.U. Bartholomew, L. Kukanskis, J. Elkind, S. Yee, C. Furlong, and R. Woodbury, "A commercial solution for surface plasmon sensing," *Sensors and Actuators B Chem.*, vol. 35, pp. 212-216, 1996.

[2.32] C. Thirstrup, W. Zong, M. Borre, H. Neff, H.C. Pedersen and G. Holzhueter, "Diffractive optical coupling element for surface plasmon resonance sensors," *Sensors and Actuators B Chem.*, vol. 100, pp.298-309, 2004.

[2.33] M.Z. Khalid, *A highly integrated Surface Plasmon Resonance Sensor based on a Focusing Diffractive Optic Element* (Master's thesis, McGill University, 2007).

[2.34] Z. Khalid, X. Hoa, C. Alleyne, M. Tabrizian, J. Beauvais, P. Charette, N.A. Nicorovici, R.C. McPhedran, and A.G. Kirk, "Integrated Surface Plasmon Resonance Sensor with periodic nanostructures for sensitivity enhancement," *Proceedings of SPIE*, vol. 6450, 2007.

[2.35] J. Homola, H.B. Lu, and S.S. Yee, "Dual-channel surface plasmon resonance sensor with spectral discrimination of sensing channels using dielectric overlayer," *Elect. Lett.*, vol. 35, pp. 1105-1106, 1999.

[2.36] A. Zybin, Ch. Grunwald, V. M. Mirsky, J. Kuhlmann, O. S. Wolfbeis, and K. Niemax, "Double-wavelength technique for surface plasmon resonance measurements: basic concept and applications for single sensors and two-dimensional sensor arrays." *Anal. Chem.*, vol. 77, pp. 2393-2399, 2005.

[2.37] R.C. Jorgenson and S.S. Yee, "A fiber-optic chemical sensor based on surface plasmon resonance," *Sensors and Actuators B Chem.*, vol. 12, pp. 213-220, 1993.

[2.38] C.R. Lavers, J.S. Wilkinson, "A waveguide-coupled surface-plasmon sensor for an aqueous environment," *Sensors and Actuators B Chem.*, vol. 22, pp. 75-81, 1994.

[2.39] J. Dostálek, J. Ctyroký, J. Homola, E. Brynda, M. Skalský, P. Nekvindová, J. Spirková, J. kvor, and J. Schröfel, "Surface plasmon resonance biosensor based on integrated optical waveguide," *Sensors and Actuators B Chem.*, vol. 76, pp. 8-12, 2001.

[2.40] M.J. Jory, P.S. Vukusic, and J.R. Sambles, "Development of a prototype gas sensor using surface plasmon resonance on gratings," *Sensors and Actuators B Chem.*, vol. 17, pp. 203-209, 1994.

[2.41] C.J. Alleyne, A.G. Kirk, R.C. McPhedran, N.-A.P. Nicorovici, and D. Maystre, "Enhanced SPR sensitivity using periodic metallic structures," *Optics Express*, vol. 15, pp.8163-8169, 2007.

[2.42] P. Adam, J. Dostálek and J. Homola, "Multiple surface plasmon spectroscopy for study of biomolecular systems," *Sensors and Actuators B Chem.*, vol. 113, pp. 774-781, 2006.

[2.43] S.C. Kitson, W.L. Barnes, and J.R. Sambles, "Full photonic band gap for surface modes in the visible," *Phys. Rev. Lett.*, vol. 77, pp. 2670-2673, 1996.

[2.44] C.V. Raman and K.S. Krishnan, "A new type of secondary radiation," *Nature*, vol. 121, pp. 501-502, 1928.

[2.45] K. Kneipp, H. Kneipp, I. Itzkan, R.R. Dasari, and M.S. Feld, "Ultrasensitive chemical analysis by Raman spectroscopy," *Chem. Rev.*, vol. 99, pp. 2957-2975, 1999.

[2.46] D.L. Jeanmaire, R.P. Van Duyne, "Surface Raman Electrochemistry Part I. Heterocyclic, Aromatic and Aliphatic Amines Adsorbed on the Anodized Silver Electrode," *J. Electroanal. Chem.*, vol. 84, pp. 1-20, 1977.

[2.47] M.G. Albrecht, J.A. Creighton, "Anomalously Intense Raman Spectra of Pyridine at a Silver Electrode". *J. Am. Chem. Soc.*, vol. 99, pp. 5215-5219, 1977.

[2.48] K. Kneipp, M. Moskovits, and H. Kneipp, *Surface-Enhanced Raman Scattering: Physics and Applications* (Springer, Berlin, 2006).

[2.49] M. Moskovits, "Surface-enhanced spectroscopy," *Rev. Mod. Phys.*, vol. 57, no. 3, pp. 783-826, 1985.

[2.50] E. Hutter and J.H. Fendler, "Exploitation of Localized Surface Plasmon Resonance," *Adv. Mater.*, vol. 16, pp. 1685-1706, 2004.

[2.51] L. A. Sweatlock, S. A. Maier, and H. A. Atwater, "Highly confined electromagnetic fields in arrays of strongly coupled Ag nanoparticles," *Phys. Rev. B*, vol. 71, 235408, 2005.

[2.52] K. Li., M. I. Stockman, and D. J. Bergman, "Self-similar chain of metal nanospheres as an efficient nanolens," *Phys. Rev. Lett.*, vol. 91, 227402, 2003.

[2.53] M. I. Stockman, "Nanofocusing of optical energy in tapered plasmonic waveguides," *Phys. Rev. Lett.*, vol. 93, 137404, 2004.

[2.54] J. B. Jackson, S. L. Westcott, L. R. Hirsch, J. L. West, and N. J. Halas, "Controlling the surface enhanced Raman effect via the nanoshell geometry," *Appl. Phys. Lett.*, vol. 82, pp. 257-259, 2003.

[2.55] B. M. Reinhard, M. Siu, H. Argarwal, A. P. Alivisatos, and J. Liphardt, "Calibration of dynamic molecular rulers based on plasmon coupling between gold nanoparticles," *Nano Lett.*, vol. 5, pp. 2246-2252, 2005.

[2.56] F. Aldaye, H. F. Sleiman, "Dynamic DNA templates for discrete gold nanoparticles assemblies: Control of geometry, modularity, write/erase and structural switching," *J. Am. Chem. Soc.*, vol. 129, pp. 4130-4131, 2007.

[2.57] Y. Xu, "Electromagnetic scattering by an aggregate of spheres," *Appl. Opt.*, vol. 34, pp. 4573-4588, 1995.

[2.58] D. W. Mackowski, "Analysis of radiative scattering for multiple sphere configurations," *Proc. R. Soc. London Ser. A*, vol. 433, pp. 599-614, 1991.

[2.59] J. H. Bruning and Y. T. Lo, "Multiple scattering of EM waves by spheres Part I - Multipole Expansion and Ray-Optical Solutions," *IEEE Tran. Antennas Propag. AP-19*, pp. 378-390, 1971.

[2.60] Y. Xu, "Calculation of the addition coefficients in electromagnetic multisphere-scattering theory," J. Comput. Phys., vol. 127, pp. 285-298, 1996.

[2.61] F. J. Garcia de Abajo, "Multiple scattering of radiation in clusters of dielectrics," *Phys. Rev. B*, vol. 60, pp. 6086-6102, 1999.

[2.62] G. Pellegrini, G. Mattei, V. Bello, and P. Mazzoldi, "Interacting metal nanoparticles: Optical properties from nanoparticle dimers to core-satellite systems," *Mat. Sci. Eng. C*, vol. 27, pp. 1347-1350, 2007.

[2.63] H. Xu, "Calculation of the near field of aggregates of arbitrary spheres," *J. Opt. Soc. Am. A*, vol. 21, pp. 804-809, 2004.

[2.64] R.-L. Chern, X.-X. Liu and C.-C. Chang, "Particle plasmons of metal nanospheres: Application of multiple scattering approach," *Phys. Rev. E*, vol. 76, 016609, 2007.

[2.65] B. Khlebtsov, A. Melnikov, V. Zharov, and N. Khlebtsov, "Absorption and scattering of light by a dimer of metal nanospheres: comparison of dipole and multipole approaches," *Nanotechnology*, vol. 17, pp. 1437-1445, 2006.

[2.66] "National Human Genome Research Institute,"
http://www.genome.gov/10001772.

[2.67] N.L. Anderson, N.G. Anderson, "Proteome and proteomics: new technologies, new concepts, and new words," *Electrophoresis*, vol. 19, pp. 1853–1861, 1998.

[2.68] M.A. Alaoui-Jamali and Y.-J. Xu, "Proteomic technology for biomarker profiling in cancer: an update," *J. Zhejiang Univ. Sci. B*, vol. 7, pp. 411-420, 2006.

[2.69] J.S. Yuk and K.-S. Ha, "Proteomic applications of surface plasmon resonance biosensors: analysis of protein arrays," *Experimental and Molecular Medecine*, vol. 37, pp. 1-10, 2005.

[2.70] T.A. Klar, "Biosensing with plasmonic nanoparticles," in *Nanophotonics with Surface Plasmons*, V.M. Shalaev, and S. Kawata, ed. (Elsevier, 2007), pp. 219-270.

[2.71] J. Homola, ed., *Surface Plasmon Resonance Based Sensors* (Springer-Verlag, Berlin, 2006).

[2.72] D.G. Myszka, and R.L. Rich, "Implementing surface plasmon resonance biosensors in drug discovery," *Pharm. Sci. Tech. Today*, vol. 3, pp. 310-317, 2000.

[2.73] J.M. Brockman, A.G. Frutos, and R.M. Corn, "A Multistep Chemical Modification Procedure To Create DNA Arrays on Gold Surfaces for the Study of Protein-DNA Interactions with Surface Plasmon Resonance Imaging," *J. Am. Chem. Soc.*, vol. 121, pp. 8044-8051, 1999.

[2.74] J. Luo, J. Zhou, P. Shen, Antibody-antigen interactions measured by surface plasmon resonance: Global fitting of numerical interaction algorithms," *J. Biochem.*, vol. 130, pp. 553-559, 2001.

[2.75] A.J.Thiel, A.G. Frutos, C.E. Jordan, R.M. Corn, L.M. Smith, "In situ surface plasmon resonance imaging detection of DNA hybridization to oligonucleotide arrays on gold surfaces," *Anal. Chem.*, vol. 69, pp. 4948-4956, 1997.

[2.76] E. Kai, S. Sawata, K. Ikebukuro, T. Ida, T. Honda, I. Karube, "Detection of electrochemical enzymatic reactions by surface plasmon resonance measurement," *Anal. Chem.*, vol. 71, pp. 796-800, 1999.

[2.77] A. Ramanavieius, F.W. Herberg, S. Hutschenreiter, B. Zimmermann, I. Lapenaite, A. Kausaite, A. Finkelsteinas, A. Ramanavieiene, *Acta Medica Lithuanica*, vol. 12, pp. 1-9, 2005.

[2.78] H. Xu, E.J. Bjerneld, M. Käll, and L. Börjesson, "Spectroscopy of Single Hemoglobin Molecules by Surface Enhanced Raman Scattering," *Phys. Rev. Lett.*, vol. 83, pp.4357-4360, 1999.

[2.79] K.E. Shafer-Peltier, C.L. Haynes, M.R. Glucksberg, and R.P. Van Duyne, "Toward a Glucose Biosensor Based on Surface-Enhanced Raman Scattering," *J. Am. Chem. Soc.*, vol. 125, pp. 588-593, 2003.

[2.80] T. Vo-Dinh, L.R. Allain, D.L. Stokes, "Cancer gene detection using surface-enhanced Raman scattering (SERS),", *J. Raman Spectroscopy*, vol. 33, pp. 511-516, 2002.

[2.81] B. Smith, "25 years of lasers and analytical chemistry: A reluctant pairing with a promising future," *Trends in Anal. Chem.*, vol. 26, pp. 60-64, 2007

[2.82] A.J. Haes and R.P. Van Duyne, "A Unified View of Propagating and Localized Surface Plasmon Resonance Biosensors," *Anal. and Bioanal. Chem.*, vol. 379, pp. 920-930, 2004.

[2.83] M.P. Kreuzer, R. Quidant, G. Badenes, M.-P. Marco, "Quantitative detection of doping substances by a localised surface plasmon sensor," *Biosens. Bioelectron.*, vol. 21, pp. 1345-1349, 2006.

[2.84] J.R. Lakowicz, "Plasmonics in Biology and Plasmon-Controlled Fluorescence," *Plasmonics*, vol. 1, pp. 5-33, 2006.

[2.85] D. Psaltis, S.R. Quake, C. Yang, "Developing optofluidic technology through the fusion of microfluidics and optics," *Nature*, vol. 442, pp. 381-386, 2006.

[2.86] M. Wang, N. Jing, I.-H. Chou, G.L. Cote, and J. Kameoka, "An optofluidic device for surface enhanced Raman spectroscopy," *Lab Chip*, vol. 7, pp. 630 - 632, 2007.

Chapter 3 – Fundamental Notions

3.1 Introduction

The entire Chapter 3 sets the theoretical foundation necessary for the understanding of the research work carried on plasmonics. Section 3.2 examines the permittivity of metals and discusses some of the unique properties. The classical picture of excitation of bound electrons is first described in Subsection 3.2.1 to depict the interband transitions that occur when higher-energy photons promote electrons from one band to another [3.1, 3.2]. Then, this classical resonator picture will be further reduced to a simpler real-valued Drude model in Subsection 3.2.2. Subsection 3.2.3 will provide the permittivities of real metals obtained from experiments. The rest of the chapter (Section 3.3 and 3.4) will discuss the electromagnetic field distributions on two specific geometries: the optical fields supported by plasmon resonance on a single planar metallic-dielectric interface (Section 3.3) and a small metallic sphere (Section 3.4). A clear understanding of how plasmon resonances enter the scenario and affect the near-fields at the surface of each of these geometries will justify the work carried out in the subsequent chapters on SPR sensors and nanospheres simulation for SERS.

3.2 Dielectric Constant under Plasmonic Effects

3.2.1 Interband Transitions Model

The dielectric constant is determined by the dynamics between the incident light and the charge polarization inside the material. Consider the dielectric displacement field **D** inside a metal under illumination,

$$\mathbf{D}(\omega) = \varepsilon_0 \mathbf{E} + \mathbf{P}(\omega) \tag{3.2.1}$$

where the alignment of dipoles with electric field **E** is described by the polarization vector **P**. An incident electromagnetic plane wave $\mathbf{E} = \mathbf{E}_0 e^{-i\omega t}$ drives the electrons inside the metal to oscillate at a frequency ω. This results in time-varying displacements

$\mathbf{r} = \mathbf{r}_0 e^{-i\omega t}$ that cause charge polarizations via $\mathbf{P} = -ne\mathbf{r}$ with n and e denoting respectively the electron density and the fundamental charge unit. At certain resonant frequencies, the polarization of oscillating charges can create an enhancement of local fields. The electron oscillation due to a time-varying potential is treated here using a classical damped harmonic oscillator. Mathematically, the oscillator is described by

$$m_e \frac{\partial^2 \mathbf{r}}{\partial t^2} + m_e \gamma \frac{\partial \mathbf{r}}{\partial t} + \alpha \mathbf{r} = -e\,\mathbf{E}_0 e^{-i\omega t} \tag{3.2.2}$$

where m_e denotes the effective mass of bound electron, γ is the radiative damping constant for finite resistivity [3.2] and α represents the spring strength constant of the potential that holds the electron [3.1]. The solution of the differential equation gives a complex displacement amplitude of

$$\mathbf{r}_0 = \frac{-e}{m_e} \frac{1}{\left(\omega_0^2 - \omega^2\right) - i\omega\gamma} \mathbf{E}_0 . \tag{3.2.3}$$

Inserting the displacement back in Eq. (3.2.1), the displacement field becomes

$$\mathbf{D}(\omega) = \varepsilon_0 \varepsilon_{interband}(\omega)\mathbf{E}(\omega) \tag{3.2.4}$$

with the relative permittivity of the metal given by

$$\varepsilon_{interband}(\omega) = \left(1 + \frac{\omega_p^2}{(\omega_0^2 - \omega^2) - i\omega\gamma}\right) \tag{3.2.5}$$

or with its real and imaginary parts shown explicitly,

$$\varepsilon'(\omega) + i\varepsilon''(\omega) = \left(1 + \frac{\omega_p^2(\omega_0^2 - \omega^2)}{(\omega_0^2 - \omega^2)^2 + (\omega\gamma)^2}\right) + i\left(1 + \frac{\omega_p^2(\omega\gamma)}{(\omega_0^2 - \omega^2)^2 + (\omega\gamma)^2}\right). \tag{3.2.6}$$

The above expressions contain the plasma frequency $\omega_p = \sqrt{(ne^2)/(m_e\varepsilon_0)}$ and a resonant angular frequency $\omega_0 = \sqrt{\alpha / m_e}$. The refractive index of the metal takes the final form of $m(\omega) = \sqrt{\varepsilon_0 \varepsilon_{interband}(\omega)}$.

In summary, when the metal is illuminated near the resonant frequency, the resulting charge density oscillation can be used to our advantage – it is the tuning control of the refractive index of the metal that makes the subject of plasmonics interesting.

3.2.2 Simplified Drude Free-Electron Model

To highlight some properties of plasmonic effects that can later be utilized, this subsection proceeds with some further simplification of the previous discussion. In this model, the electrons are free and no longer assumed in bound states, the spring constant α is suppressed and the effective mass m_e is substituted with the electron rest mass. Furthermore, the resistive damping γ is further removed in order to have a real-valued permittivity for simple illustration. With all the above mentioned adjustments, Eq. (3.2.5) reduces to the familiar Drude dielectric constant [3.3-3.4],

$$\varepsilon_{Drude}(\omega) = \left(1 - \frac{\omega_p^2}{\omega^2}\right). \tag{3.2.7}$$

By assuming an incident plane wave of the form $\mathbf{E}(\mathbf{r},t) = \mathbf{E}_0 e^{i(\mathbf{k}\cdot\mathbf{r}-\omega t)}$, the two curl Maxwell's equations are combined to form a description of the electromagnetic waves inside a non-magnetic metal in time and spatial frequency domains, respectively,

$$\nabla \times \nabla \times \mathbf{E} = -\mu_0 \mu \frac{\partial^2 \mathbf{D}}{\partial t^2} \tag{3.2.8}$$

$$\mathbf{k}(\mathbf{k}\cdot\mathbf{E}) - k^2\mathbf{E} = -\frac{\omega^2}{c^2}\varepsilon(\mathbf{k},\omega)\mathbf{E} \tag{3.2.9}$$

where $\varepsilon(\mathbf{k},\omega)$ is the relative dieclectric constant inside the metal depending on the direction and the frequency of an illumination. Two kinds of waves are distinguished from Eq. (3.2.9). At instances where $\varepsilon(\mathbf{k},\omega) = 0$, Eq. (3.2.9) reveals a wave of longitudinal nature since the wavevector **k** must be parallel to the electric field oscillation **E**. This solution is often referred to as the *bulk plasmon mode*. For a transverse wave solution $(\mathbf{k}\cdot\mathbf{E} = 0)$, Eq. (3.2.9) yields the familiar propagation relationship subject to variations of the relative dielectric constant,

$$k^2 = \frac{\omega^2}{c^2}\varepsilon(\mathbf{k},\omega). \tag{3.2.10}$$

By inserting the real-valued Drude dielectric constant (3.2.7) into the above expression and defining a complex propagation constant $k = \beta - i\alpha/2$, Eq. (3.2.10) becomes $k^2 = (\omega^2/c^2)(1-\omega_p^2/\omega^2)$, for which we can notice different propagation behaviours depending on the sign of the right hand side. If the frequency is above that of plasma

$(\omega > \omega_p)$, the wavenumber is real and the metallic medium acts as a lossless dielectric with a characteristic propagation constant $\beta = (\omega^2 - \omega_p^2)^{1/2}/c$ and a refractive index $m = \sqrt{\varepsilon} = (1 - \omega_p^2/\omega^2)^{1/2}$. This transparent region is referred to as the *plasmonic band* or simply *region of propagation*. On the other hand, if $(\omega < \omega_p)$, the wavenumber becomes imaginary and attenuation takes place instead of a propagation with a constant $\alpha = 2k_0(\omega_p^2/\omega^2 - 1)^{1/2}$. The permittivity constant (3.2.7) is negative in this region and the wave impedance is imaginary. Recall that electromagnetic waves are reflected at an interface between imaginary and real impedances, which is consistent with the fact that metallic surfaces are often used for mirrors. Again, this band is known as the *forbidden band*, or *region of attenuation*. The results obtained from the real-valued Drude model are plotted in Fig. 3.1. In general, the relative dielectric constant is complex and wave propagation is also attenuated.

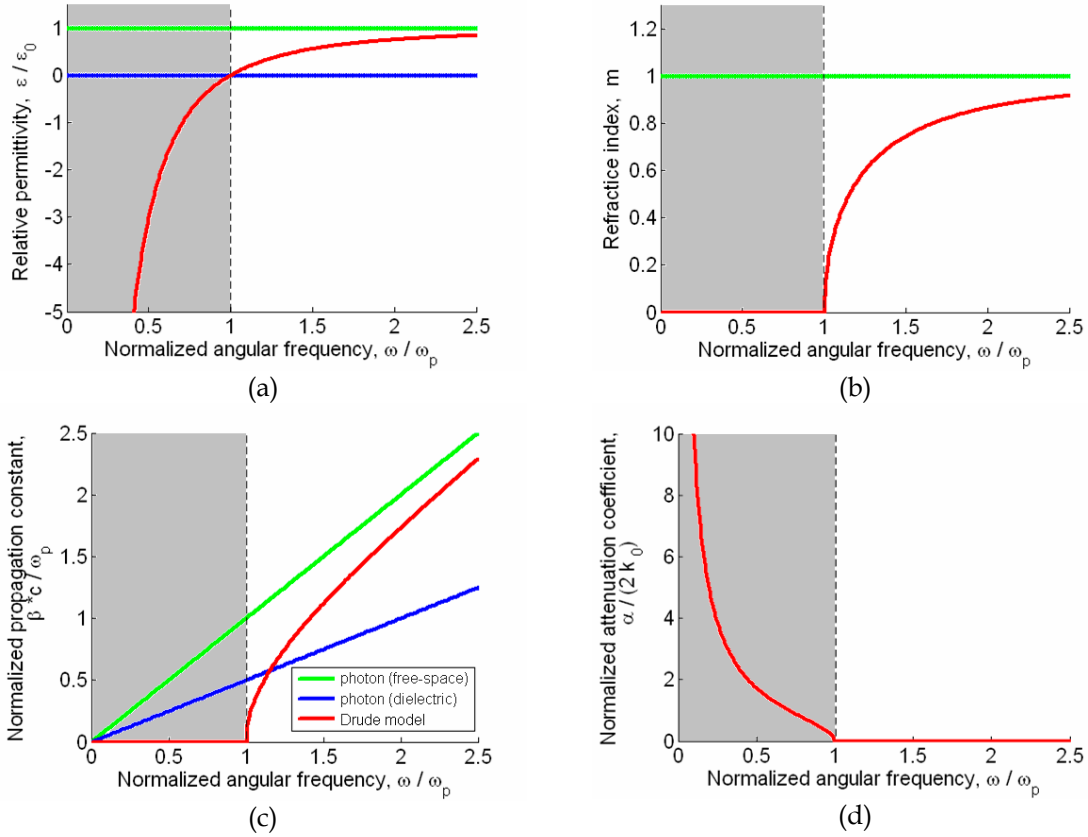

Figure 3.1 – Various quantities from the simplified real-valued Drude free-electron model: (a) relative permittivity $\varepsilon/\varepsilon_0$ (b) refractive index m (c) normalized propagation constant $\beta c/\omega_p$ (d) normalized attenuation coefficient $\alpha/(2k_0)$.

3.2.3 Permittivity from Real Metals

The real-valued Drude model discussed previously only gives us a qualitative picture of what is happening in reality. In order to fully account for the interband transitions in real metals, permittivity obtained from direct measurements are preferred. Johnson and Christy [3.5] is a well cited source of such data. From reflection and transmission measurements on vacuum-evaporated thin film, they obtained the refractive index n and the optical absorption constant κ of noble metals such as gold, silver and copper for the visible and near-infrared portions of the electromagnetic spectrum. From the definitions of complex refractive index and permittivity,

$$\begin{aligned} m(\omega) &= n + i\kappa \\ \varepsilon(\omega) &= \varepsilon'(\omega) + i\varepsilon''(\omega) = m^2 \end{aligned} \tag{3.2.11}$$

the measured quantities can be readily translated into a complex permittivity via $\varepsilon' = n^2 - \kappa^2$ and $\varepsilon'' = 2n\kappa$. The permittivity for many wavelengths are tabulated and plotted in Table B.1 (Appendix B) and Fig. 3.2. The refractive index and the absorption constant are also shown. These values are used in simulations or in designing apparatus.

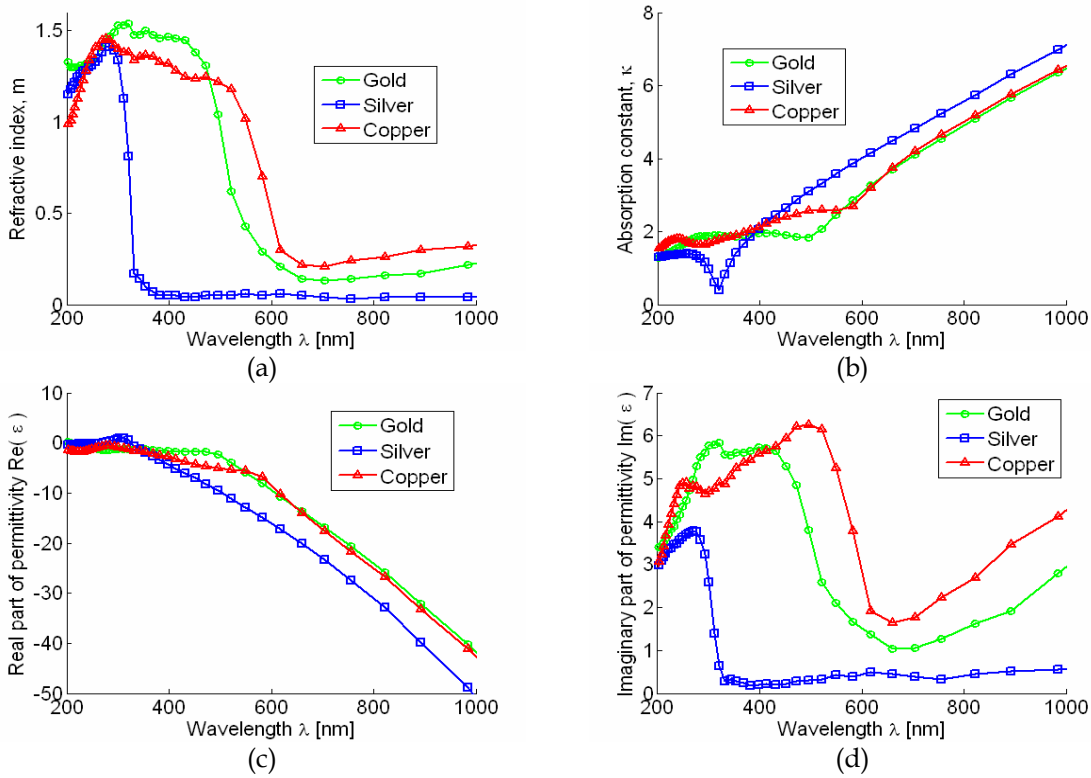

Figure 3.2 – Data curves plotted from real metals (gold Au, silver Ag, copper Cu) for their (a) refractive index m (b) absorption constant κ (c) real and (d) imaginary part of permittivity ε.

3.3 Plasmon Resonances Supported on a Planar Interface

3.3.1 Geometry and Problem Setup

The problem for obtaining the near-fields in a two-region planar geometry drawn in Fig. 3.3 consists of solving the Maxwell's equation using rectangular coordinates [3.6, 3.7]. The plane $z = 0$ separates the metallic layer from the dielectric. The dielectric and metal layers are characterized respectively by permittivities ε_D and ε_M .

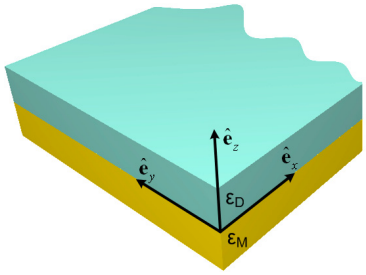

Figure 3.3 – A dielectric-metallic interface. The indices D and M denote respectively the dielectric and the metal layers.

3.3.2 The Field Distributions for Transverse Magnetic

The transverse magnetic wave (TM or p-polarized) at the vicinity of a metal-dielectric interface carry interesting properties. The non-trivial fields are [3.2],

$$\begin{aligned} H_y(z) &= Ae^{i\beta x}e^{-\gamma_D z} \\ E_x(z) &= \frac{i\gamma_D A}{\omega\varepsilon_0\varepsilon_D}e^{i\beta x}e^{-\gamma_D z} \\ E_z(z) &= \frac{-\beta A}{\omega\varepsilon_0\varepsilon_D}e^{i\beta x}e^{-\gamma_D z} \end{aligned} \qquad (3.3.1a)$$

inside the dielectric region $z > 0$, and

$$\begin{aligned} H_y(z) &= Ae^{i\beta x}e^{\gamma_M z} \\ E_x(z) &= \frac{-i\gamma_M A}{\omega\varepsilon_0\varepsilon_M(\omega)}e^{i\beta x}e^{\gamma_M z} \\ E_z(z) &= \frac{-\beta A}{\omega\varepsilon_0\varepsilon_M(\omega)}e^{i\beta x}e^{\gamma_M z} \end{aligned} \qquad (3.3.1b)$$

for the metal region $z < 0$. An oscillatory behaviour is exhibited in the x-direction (wavenumber β) while the field decays exponentially normal to the interface

(wavenumber γ). The solutions are spatially invariant in y-direction. The usual boundary conditions at the interface yield the condition $\gamma_D / \gamma_M = -\varepsilon_D / \varepsilon_M(\omega)$ [3.2]. With the signs defined in the arguments of the decaying exponential factor, the real part of the metal permittivity needs to be negative, $\mathrm{Re}\{\varepsilon_M\} < 0$ while that of the dielectric remains positive, $\varepsilon_D > 0$ in order for the fields to be confined on the interface. Many metals fulfill this condition in the visible and near-infrared range [3.8]. An expression relating the propagation constant of the surface wave and the permittivities is given by [3.2, 3.8],

$$\beta = k_0 \sqrt{\frac{\varepsilon_M(\omega)\,\varepsilon_D}{\varepsilon_M(\omega) + \varepsilon_D}} \tag{3.3.2}$$

where $k_0 = \omega / c$ denotes the free-space wavenumber. The propagation constant becomes extremely large ($\beta \to \infty$) when the denominator inside the radicand becomes null. The fields therefore acquire an electrostatic character and permeate uniformly the whole surface. In general, the metal permittivity is a complex quantity, so the propagation constant in Eq. (3.3.2) contains both a propagation and attenuation parts. Due to the damping, the propagation constant β will remain finite. The 1/e distance can be used to define a *propagation length* in the x-direction and a *penetration depth* along the z-direction. Also, a *concentration of field* can be defined as the spatial integral (the area under the curve) of the fields inside some region. These quantities characterize how compactly local fields are confined. Homola has tabulated such values for the silver and gold metals at two distinct wavelengths in the visible and near-infrared ranges [3.8], which is borrowed and presented in Table 3.1 below. In fact, metals are highly lossy in these ranges and this results in a high attenuation. The distribution of the fields is highly asymmetric in the metal and dielectric layers and most of the field is concentrated in the latter. The distribution of electromagnetic fields given by Eq. (3.3.1) is plotted in Fig. 3.4 for a gold-water interface.

metal	**silver**		**gold**	
wavelength	**630nm**	**850nm**	**630nm**	**850nm**
Propagation length [μm]	19	57	3	24
Penetration depth into metal [nm]	24	23	29	25
Penetration depth into dielectric [nm]	219	443	162	400
Concentration of field in dielectric [%]	90	95	85	94

Table 3.1 – Major characteristics of surface plasmons at the metal-water interface [3.8].

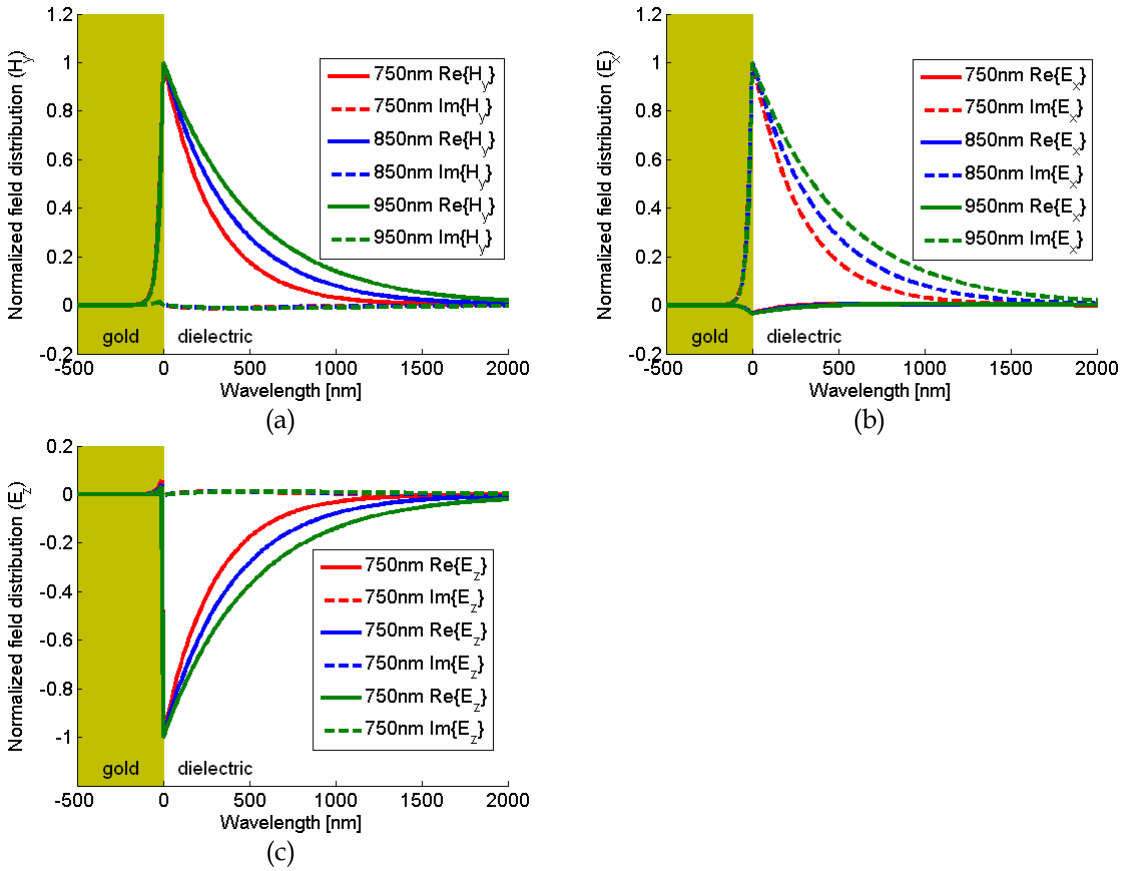

Figure 3.4 – Normalized electric and magnetic fields distribution of a surface plasmon mode at the interface of a metal (gold) and dielectric medium (water m = 1.33) for three different wavelengths. (a) H_y (b) E_x (c) E_z.

3.3.3 The Field Distributions for Transverse Electric

To complete our discussion of the metal-dielectric interface, the transverse electric wave (TE or s-polarized) needs to be considered as well. However, it will be revealed shortly that no surface plasmon mode is supported for this wave polarization. Using a similar procedure from the previous section, the non-trivial field distributions in the dielectric region $z > 0$ are given by

$$E_y(z) = Ae^{i\beta x}e^{-\gamma_D z}$$
$$H_x(z) = \frac{-i\gamma_D A}{\omega\mu_0}e^{i\beta x}e^{-\gamma_D z} \qquad (3.3.3a)$$
$$E_z(z) = \frac{\beta A}{\omega\mu_0}e^{i\beta x}e^{-\gamma_D z}$$

where as in the metal region $z < 0$, they are

$$H_y(z) = Ae^{i\beta x}e^{\gamma_M z}$$
$$E_x(z) = \frac{i\gamma_M A}{\omega\mu_0}e^{i\beta x}e^{\gamma_M z} \qquad (3.3.3b)$$
$$E_z(z) = \frac{\beta A}{\omega\mu_0}e^{i\beta x}e^{\gamma_M z}.$$

The boundary conditions on the fields at the interface result in $A(\gamma_D + \gamma_M) = 0$ [3.2]. The signs adopted above force the real part of both wavenumbers to be positive ($\mathrm{Re}\{\gamma_D\} > 0$ and $\mathrm{Re}\{\gamma_M\} > 0$) in order to have field confinement at the interface. This imposes the amplitude A of the fields to be zero. The plasmon resonance is thus not supported on the transverse electric mode.

3.3.4 Multiple Interfaces

In multiple metal-dielectric interfaces, the surface plasmon modes confined on each boundary can couple to each other if the evanescent tails from the decaying fields overlap [3.2]. For example, a three-layer insulator/metal/insulator (IMI) illustrated in Fig. 3.5 (a) is used in prism coupled SPR sensors. In these systems, the far-field radiations are totally attenuated at the first insulator-metal interface. Then, the evanescent tail will couple to the surface plasmon mode at a second interface. More about SPR sensing apparatus will be presented in Chapter 4. On the other hand, metal/insulator/metal systems (MIM), illustrated in Fig. 3.5 (b), have been investigated for their potential in interconnect applications. Several discussions about surface plasmon propagation and confinement using MIM structures can be found in [3.9-3.11].

(a) (b)

Figure 3.5 – Three-layer system (a) IMI and (b) MIM geometries.

3.4 Plasmon Resonances Supported on a Single Sphere

3.4.1 Geometry and Problem Setup

We now turn our attention to plasmon resonance supported on a single metallic sphere of radius *a*, with permittivity ε_M and buried in a dielectric medium characterized by a permittivity ε_D (Fig. 3.6). Surface plasmon mode can enhance the near-fields confined at the interface when a proper illumination is set. For a sphere, the electromagnetic fields can be solved approximately using the quasi-static approximation or exactly using Mie Theory.

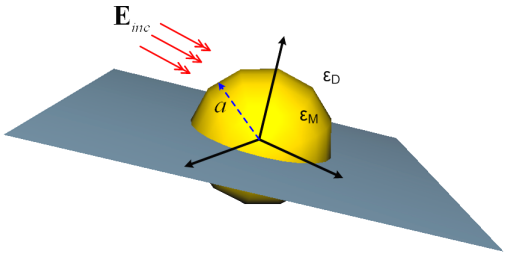

Figure 3.6 – Geometry of a metallic sphere.

3.4.2 The Field Distributions from the Electrostatic Approximation

When the radius of the sphere is much smaller than the wavelength of the driving electromagnetic field, that is, $a << \lambda$, the sphere experiences an uniform incident field (with magnitude $\mathbf{E}_0$) since the spatial dependence to $\exp(i\mathbf{k}\cdot\mathbf{r})$ is slow varying. This is known as the Rayleigh limit. An electrostatic (or quasi-static) approach can therefore be used to solve the fields scattered from the sphere. Solving the Laplacian of the electric potential $\nabla^2\phi = 0$ in spherical coordinates yields solution $\phi(\mathbf{r},\theta)$ in terms of Legendre polynomials $P_l^m(\cos\theta)$ and $Q_l^m(\cos\theta)$ [3.12], with no azimuthal dependance. The electric field inside and outside the sphere can be obtained via $\mathbf{E} = -\nabla\phi$ as [3.1, 3.2],

$$\mathbf{E}_{in} = \frac{3\varepsilon_D}{\varepsilon_M(\omega) + 2\varepsilon_D}\mathbf{E}_0 \tag{3.4.1a}$$

$$\mathbf{E}_{out} = \mathbf{E}_0 + \frac{3\mathbf{u}(\mathbf{u}\cdot\mathbf{p}) - \mathbf{p}}{4\pi\,\varepsilon_0\varepsilon_D}\frac{1}{r^3} \tag{3.4.1b}$$

where **u** is an unit vector in Cartesian coordinate (x, y, z). The dipole moment is expressed as $\mathbf{p} = \alpha\varepsilon_0\varepsilon_D\mathbf{E}_0$, with an induced polarizability α in the form of the well known Clausius-Mossotti expression [3.13],

$$\alpha = 4\pi a^3 \frac{\varepsilon_M(\omega) - \varepsilon_D}{\varepsilon_M(\omega) + 2\varepsilon_D}. \tag{3.4.2}$$

Eq. (3.4.1) describes a dipole radiation pattern whose field strength is affected by the size of the sphere and the permittivity of the metal at different frequencies. It is to be noted that the tuning of the metal dielectric via a certain frequency directly affects the induced polarization, and hence the local field reach near the sphere. Two instances of the magnitude of the electric field (at two different wavelengths and polarization of incident field) are plotted in Fig. 3.7. The measurable far-field quantities such as the scattering and absorption cross-sections (given by $C_{sca} = k^4 |\alpha|^2 / (6\pi)$ and $C_{abs} = k\,\mathrm{Im}\{\alpha\}$ [3.2]) are also directly influenced by the size of the sphere and the plasmonic variation.

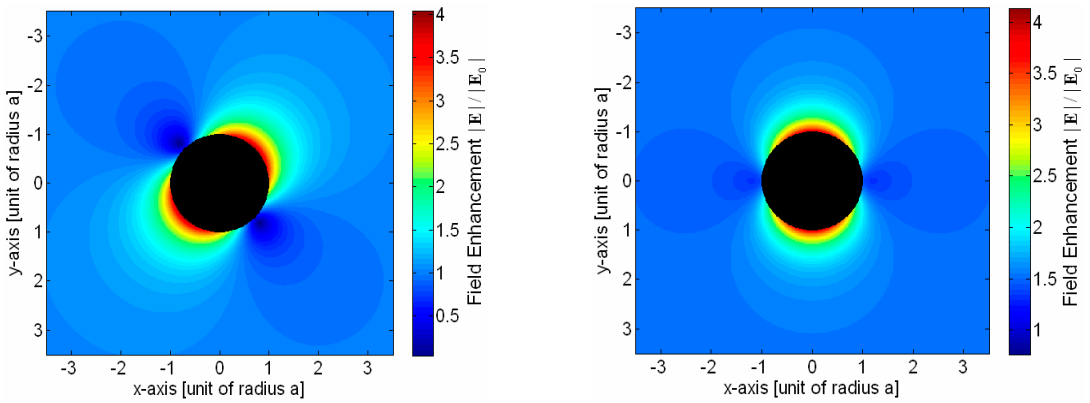

Figure 3.7 – Quasi-static dipole radiation patterns. The field enhancement $|\mathbf{E}|/|\mathbf{E}_0|$ for (a) xy-polarized **E**, ε_M = -13.648 + *i* 1.035, ε_D = 1.7689 and (b) y-polarized **E**, ε_M = -1.692 + *i* 5.649, ε_D = 1.7689. The fields internal to the sphere are not shown.

3.4.3 The Field Distributions from Full Vector Mie Theory

It happens that the dipole radiation patterns provided using the quasi-static approximation fail to describe accurately the field distributions around a large sphere. This is especially true if the sphere experiences the phase changes of the driving electric fields. In this case, recourse to a rigorous model is necessary. In 1908, Gustav Mie solved

the light scattering and absorption of a sphere exactly, using a full vector electrodynamics approach. In his paper [3.14], he decomposed the optical fields **E** and **H** inside and outside the sphere into well known vector spherical harmonics basis $\mathbf{N}^{(1)}$, $\mathbf{M}^{(1)}$, $\mathbf{N}^{(3)}$, $\mathbf{M}^{(3)}$ [3.12]. Essentially, the fields are described as superposition of appropriately weighted multipole radiation patterns, or the so-called *normal modes*, illustrated in Fig. 3.8. The higher orders complete the description of the electromagnetic fields near a sphere. A comparison between dipole and multipole approaches has been given [3.15].

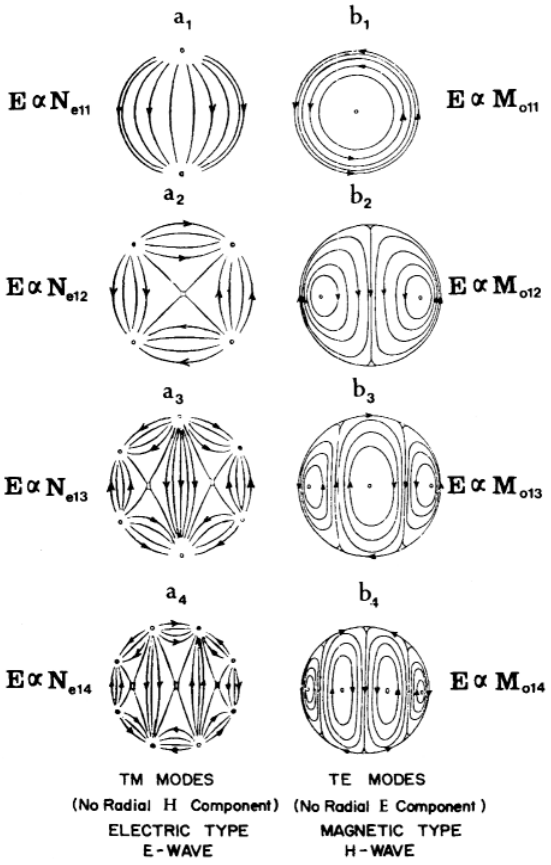

Figure 3.8 – Normal modes from Mie Theory [3.12, 3.14]

Since Chapter 5 is entirely devoted to the proper implementation of a generalized Mie Theory (or multiple-multipole methods), appropriate for light scattering problems involving an ensemble of strongly coupled spheres, only a brief qualitative discussion of the single-sphere Mie Theory will be given. For a detailed treatment on the subject, the following references are suggested [3.16-3.18]. Two important parameters that should be mentioned are the Lorenz-Mie coefficients that directly affect the strength of the

scattered fields around the sphere. These coefficients for the *n*-th order harmonics are given as functions of the normalized radius $x = 2\pi m_{out}\, a / \lambda_{vacuum}$ and refractive index contrast $m = m_{in} / m_{out}$ as [3.16],

$$\alpha_n = \frac{m\psi_n'(x)\psi_n(mx) - \psi_n(x)\psi_n'(mx)}{m\xi_n'(x)\psi_n(mx) - \xi_n(x)\psi_n'(mx)}$$
$$\beta_n = \frac{\psi_n'(x)\psi_n(mx) - m\psi_n(x)\psi_n'(mx)}{\xi_n'(x)\psi_n(mx) - m\xi_n(x)\psi_n'(mx)} \qquad (3.4.3)$$

where $\psi_n(\rho) = \rho\, j_n(\rho)$ and $\xi_n(\rho) = \rho\, h_n^{(1)}(\rho)$, with j_n and $h_n^{(1)}$ the spherical Bessel and spherical Hankel functions of first kind. Note that the above equations vanish as the contrast *m* approaches unity; no scattering occurs since there is no sphere at all! The plasmonic effects enter this formalism through the refractive index of the sphere given that $m_{in}(\omega) = \sqrt{\varepsilon_{in}(\omega)}$. Expressions for the far-field scattering and absorption cross sections also exist in Mie Theory [3.16].

3.5 References

[3.1] L. Novotny and B.Hecht, *Principles of Nano-Optics* (University Press, Cambridge, 2006).

[3.2] S.A. Maier, *Plasmonics – Fundamentals and Applications* (Springer, Bath, 2007).

[3.3] B.E.A. Saleh, M.C. Teich, *Fundamentals of Photonics*, 2nd ed. (Wiley-Interscience, 2007)

[3.4] C. Kittel, Introduction to Solid State Physics, 8th ed. (Wiley, 2005), chapter 14.

[3.5] P.B. Johnson and R.W. Christy, "Optical constants of the noble metals," *Phys. Rev. B*, vol. 6, pp. 4370-4379, 1972.

[3.6] K. Okamoto, *Fundamentals of Optical Waveuides* (Academic Press, San Diego 2000).

[3.7] C. Pollack, M. Lipson, *Integrated Photonics* (Kluwer Academic Publishers, 2003).

[3.8] J. Homola, S.S. Yee, G. Gauglitz, "Surface plasmon sensors: review," *Sensors and Actuators B*, vol. 54, pp. 3-15, 1999.

[3.9] E.N. Economou, "Surface Plasmons in Thin Films," *Phys. Rev.*, vol. 182, pp. 539-554, 1969.

[3.10] R. Zia, M.D. Selker, P.B. Catrysse, and M.L. Brongersma, "Geometries and materials for subwavelength surface plasmon modes," *J. Opt. Soc. Am. A*, vol. 21, pp. 2442, 2004.

[3.11] G. Veronis and S. Fan, "Theoretical investigations of compact couplers between dielectric slab waveguides and two-dimensional metal-dielectric-metal plasmonic waveguides", *Optics Express*, vol. 15, pp. 1211-1221, 2007.

[3.12] G. Arfken and H.J. Weber, *Mathematical Methods for Physicists*, 6th ed. (Academic, Orlando, 2005).

[3.13] J.D. Jackson, *Classical Electrodynamics*, 3rd ed. (Wiley, 1998).

[3.14] G. Mie, "Beiträge zur Optik trüber Medien, speziell kolloidaler Metallösungen," *Ann. Phys.*, vol. 330, pp. 377–445, 1908.

[3.15] B. Khlebtsov, A. Melnikov, V. Zharov, and N. Khlebtsov, "Absorption and scattering of light by a dimer of metal nanospheres: comparison of dipole and multipole approaches," *Nanotechnology*, vol. 17, pp. 1437-1445, 2006.

[3.16] C.F. Bohren and D.R. Huffman, Absorption and Scattering of Light by Small Particles (Wiley, New York, 1983).

[3.17] U. Kreibig and M. Vollmer, *Optical Properties of Metal Clusters* (Springer, Berlin, 1995).

[3.18] H.C. van de Hulst, *Light Scattering by Small Particles* (Dover, New York, 1981).

Chapter 4 – Sensing with Surface Plasmon Resonance

4.1 Introduction

One of the established applications of plasmon resonance is in index-of-refraction sensing. Surface plasmon resonance (SPR) sensors utilize the coupling condition to surface modes confined at an interface between two materials that have permittivities of opposite signs to report the presence of biochemical analytes. This chapter is devoted to the experimental work carried on SPR sensors. After briefly explaining the principles of operation including the different photons to surface plasmons coupling schemes, two SPR systems will be presented (shown in Fig. 4.1 (a) and (b)). The features of an integrated SPR sensor and a 2D SPR sensor will be discussed in Section 4.3 and Section 4.4, respectively, along with their characterization using NaCl solutions. For a detailed discussion on the working principles and the performance of other SPR sensors, please refer to Homola [4.1].

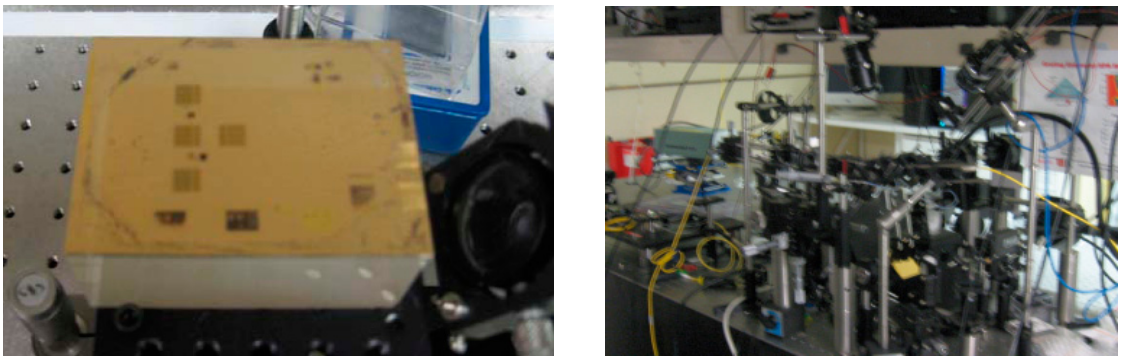

(a) (b)

Figure 4.1 – Two SPR systems at the Free-Space Laboratory of Photonic Systems Group: (a) integrated SPR sensor (b) 2D SPR sensor with combined wavelength-angle modulation.

4.2 Sensing Principle

4.2.1 Index-of-refraction Sensing Modality

The strongly localized electromagnetic fields at a dielectric-metal interface presented in Chapter 3.3 can be further employed for index-of-refraction sensing. In a

SPR sensor, the coupling of far-field radiation to the surface plasmon mode occurring near the metal and sensing layer is monitored while the refractive index of the sensing layer is subject to variation. To understand the operating principle of SPR sensors, a discussion about the excitation of such a surface charge density wave is necessary.

From Eq. (3.3.2), it can be noticed that the propagation constant for the surface mode β_{SP} is always larger than the wavevector in free space, given simply by $k = \omega c$. This implies that the surface plasmons always have more momentum than free-space photons of the same frequency. It is therefore not possible to excite the surface modes directly from free-space since no solution satisfy the matching of energy and momentum. Therefore, in order to increase the momentum up to $k = \omega c\, n_P \sin\theta$, a third insulating substrate layer can be added while launching the incident light at an angle θ. This prism arrangement is commonly known as the Kretschmann configuration which consists of a dielectric-metal-dielectric multilayer. It is shown in Fig. 4.2 [4.2].

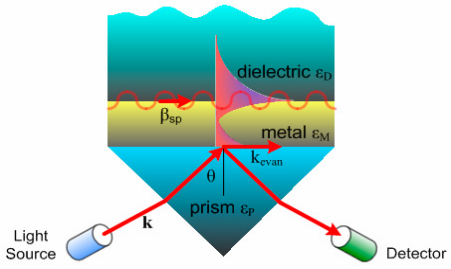

Figure 4.2 – Prism coupled SPR sensing geometry.

Using a TM-polarized illumination source, an attenuated total reflection (ATR) occurs at the prism-metal boundary; a part of the energy is reflected and a part is exponentially attenuated in the metal. The intensity of the reflected wave is captured and monitored in real-time using a detector. Inside the metal, the evanescent decaying field can couple to a surface plasmon mode at the metal-dielectric boundary if the metal film is thin enough and if the surface plasmon resonance condition is fulfilled. The resonance condition refers to the precise wavelength and angle of the incident light that matches the energy and momentum of the evanescent wave and the surface plasmons, that is

$$\frac{2\pi}{\lambda} n_P \sin\theta = \mathrm{Re}\{\beta_{SP}\}. \qquad (4.2.1)$$

At the resonance, the energy of the photons is transferred to the plasmons and a sharp dip is observed in the reflected intensity when plotted with respect to wavelength λ or the angle of incidence θ. For a detailed description about the factors that influence the reflectance, the following references are suggested [4.1, 4.3]. At this point, recall that the surface plasmon mode is a solution to only the TM-polarization; therefore, the incident wave needs to be of that polarization (Section 3.3.3).

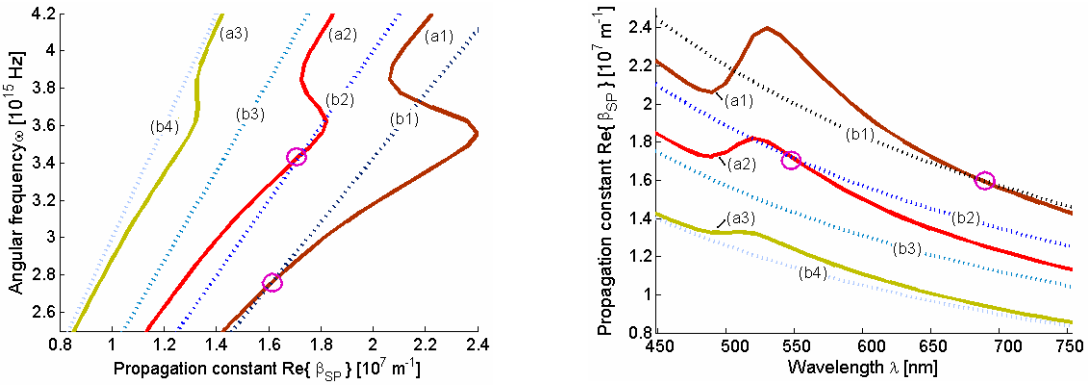

(a) (b)

Figure 4.3 - Dispersion relations of the SP mode for a dielectric-metal-dielectric. The metal is taken as gold (Au). (a) On the left, ω vs. Re{β_{SP}} is displayed. (b) On the right, the corresponding curves are potted with respect to the illumination wavelength λ. On both sides, the solid lines represents Re$\{\beta_{SP}\}$ in different sensing layers: (a1) $\varepsilon_D = 1.60^2$ (a2) $\varepsilon_D = 1.30^2$ (a3) $\varepsilon_D = 1.00^2$ (square of refractive indices) . The dotted lines are the curves for the wavelength of the incident light $(2\pi/\lambda)\, n_P \sin\theta$ at different angles or prism coupling refractive index: (b1) $n_P \sin\theta = 1.75$; (b2) $n_P \sin\theta = 1.50$ (b3) $n_P \sin\theta = 1.25$ (b4) $n_P \sin\theta = 1.00$. The intersection of a dotted line with a solid line is a solution fulfilling the coupling condition.

SPR sensing relies on the short penetration depth of the evanescent tail decaying into the top dielectric layer (of ε_D). Any change taking place at the vicinity of that interface is subject to a perturbation of the coupling condition to the surface plasmon mode. The left and right-hand sides of Eq. (4.2.1) for a prism-gold-water expressed in terms of the light frequencies and wavelengths are plotted in Fig. 4.3 (a) and (b). Illustrated is the water medium that experiences different value of dielectric constant ε_D. The angle of incidence θ or the wavelength λ of the light source that satisfies the resonance condition changes with the sensing layer. A SPR sensing apparatus can thus be designed to interrogate the angle θ, or the wavelength λ, or both.

The local perturbation at the vicinity of the metal-sensing layer interface serves as the sensing principle for detecting molecules bound onto the metal surface. For example, the binding of an analyte is illustrated in Fig. 4.4. Molecules are selectively captured by chemically-engineered receptors so that only the target analytes perturb the coupling condition [4.4]. Then, the recorded changes of local refractive index in time offer a label-free method to identify analytes and their concentrations.

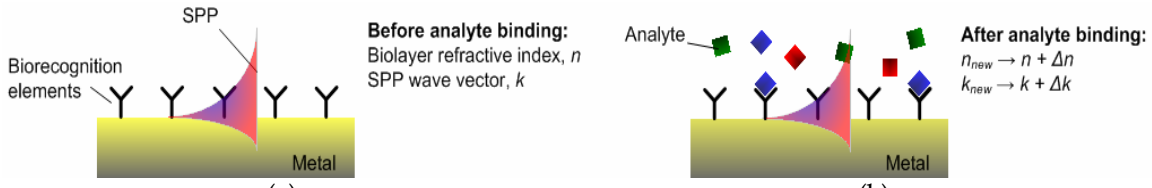

Figure 4.4 – Binding of analytes (a) before and (b) after.

4.2.2 Other Coupling Schemes

In addition to the prism coupling scheme discussed in Section 4.2.1, other methods to couple far-field radiation to surface plasmon mode on a planar surface also exist, namely the direct and indirect grating couplings and the guided wave coupling [4.1] , as illustrated in Fig. 4.5.

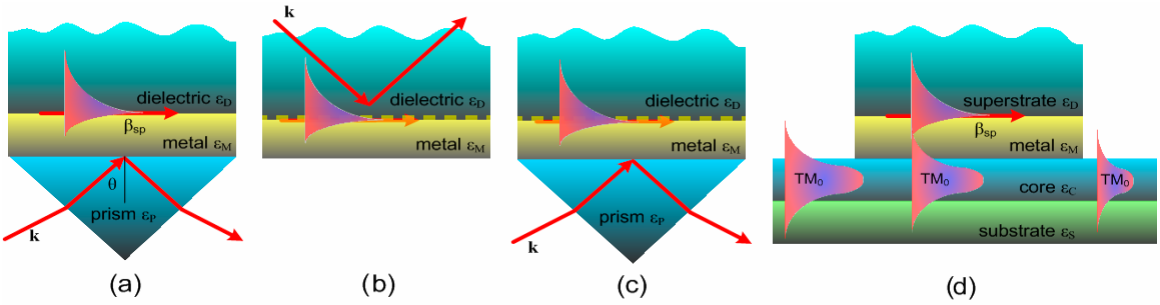

Figure 4.5 – Different methods to excite surface plasmons: (a) prism coupling (b) direct grating coupling (c) indirect grating coupling (d) waveguide coupling.

A special attention is given to the grating coupling methods, in particular the indirect one. When a grating is formed by adding corrugation to a metallic surface, optical excitation of the surface plasmons is achieved through the diffraction of light if the required momentum matching is satisfied for a given diffracted mode [4.1]. In the direct grating method, the light is incident from the sensing dielectric layer, as shown in

Fig. 4.5 (b). However, this actually requires the sample medium to be optically transparent, thus limiting the number of substances which can be analyzed. On the other hand, the indirect grating method combines the benefits of the prism coupling scheme with additional control of the perturbation of the surface plasmon propagation. In fact, under certain circumstances, the periodicity of the corrugation on the metal surface may prohibit the propagation of the surface plasmon modes over some range [4.5], thus creating a bandgap. For example, if the pitch of the grating corrugation is half of the surface plasmon wavelength along the propagation axis, then Bragg scattering of the modes might lead to surface plasmon standing waves at different energies and an opening of the energy gap in the dispersion relation [4.6]. An illustration from [4.7] is given in Fig 4.6.

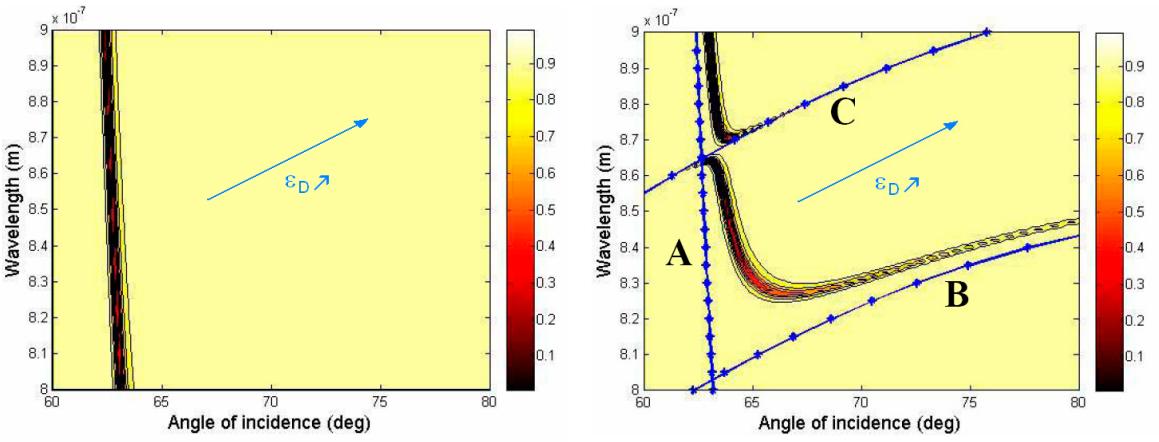

Figure 4.6 – Dispersion curves for (a) flat metal surface (b) sinusoidal grating with 20nm of grating height and 300nm of periodicity. [4.7] The normalized reflection intensity is shown.

In Fig. 4.6, simulated two-dimensional reflection intensities plotted for a range of wavelengths and angles (λ, θ) near 850nm is shown. Fig 4.6 (a) shows the dispersion curves for a flat metal surface (without grating) whereas Fig. 4.6 (b) displays the counterpart for a periodically corrugated metal surface. An opening of a bandgap is seen. For comparison, the vertical dotted line A represents the curve without the bandgap where as lines C and B represent respectively the backward propagating surface plasmon mode and the substrate mode. For both figures, the curves are subject to move toward the top-right as the dielectric constant of the sensing layer increases.

One interesting improvements to existing SPR sensors is the enhancement of sensitivity near the bandgap by using these periodic metallic structures. Numerical results from Alleyne et al. [4.7] suggest that a six-fold enhancement of the SPR sensitivity can be obtained if a sinusoidal silver grating is used instead to just a flat metallic surface.

4.3 System #1: Integrated SPR using Focusing DOE

4.3.1 Overall Device Presentation

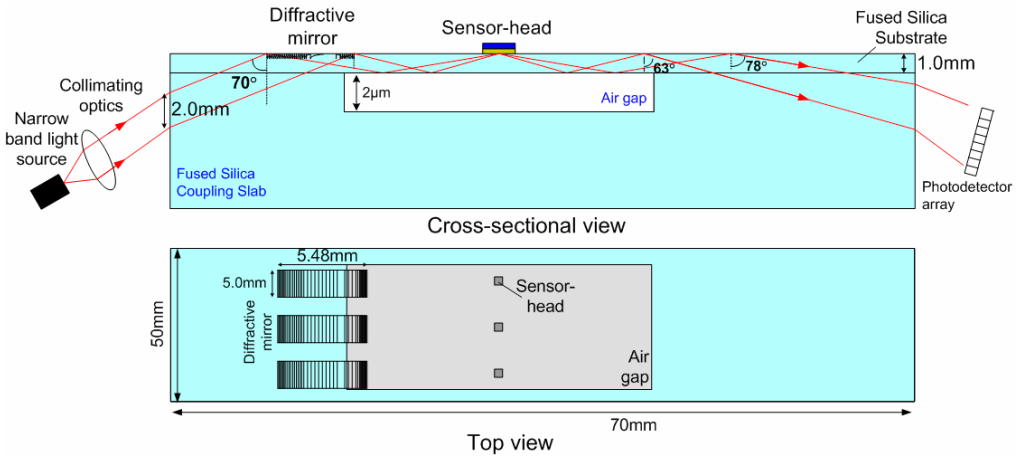

Figure 4.7 – Integrated SPR device diagram [4.8]. A three channel scheme is implemented in this integrated prototype.

In the health care and pharmaceutical communities, portable devices that can be used outside the laboratory for screening of analytes are highly desirable. The integrated SPR sensor (Fig. 4.1 (a)) at the Photonic Systems Group using focusing diffractive optical element (DOE) is designed to achieve this goal. This sensing device is fabricated using micro-optic fabrication techniques to demonstrate the possibility of miniaturization and integration with microfluidic platforms. The design details and fabrication have been previously documented in [4.8, 4.9]. The sensor uses the prism coupling scheme and operates at a fixed wavelength. At the output, light of different incident angles is directed to different pixel positions of a photodetector. Its schematic is shown in Fig. 4.7.

In this device, diffraction is used for light focusing whereas refractive optics is used in the rest of the device. The key component that allows miniaturization is a

focusing DOE (a 1D Fresnel lens) playing the role of a conventional cylindrical lens. This system is based on angular interrogation because the DOE operates at a fixed wavelength. Microfabrication processes, similar to that in microelectronics, are applied to make this DOE. However, in order to fabricate this diffractive element in-house with minimum feature sizes above submicron scales, a constraint is set on the location of the light source. The narrow band collimated laser source incident onto the diffractive mirror has to enter at an oblique angle. For a normal incidence, the DOE with submicron features will need to be fabricated using laser beam holography combined with an injection molding process [4.8] and the reported diffraction efficiency is quite low [4.10].

According to the design [4.8], a 70° off-axis illumination is adopted to cover an aperture size of 5.484mm, imposed by the DOE. The fused silica coupling slab is chosen to be 30mm thick. The polarization of the light is transverse magnetic, as required for the excitation of the surface plasmons and the center wavelength is around 850nm, which allows us to attain the maximum field penetration depth while using glass [4.7]. At the output of the DOE, the beam is focused in such a way that the marginal rays emanate at respectively 63° and 78°, for a total angular range of 15°. Just below the sensor head (formed by metal-dielectric layers), an air gap of 2μm is etched in the fused silica in order to achieve total internal reflection of the light, as required in prism coupling.

Sample solutions are placed above the sensor head where a surface plasmon mode is excited for a given angle. A photodetector is placed at the far end of the device to provide an image of the various angles of light reflected away from the metal-dielectric interface. The shift in the reflection intensities minimum (dip) as the index-of-refraction changes is therefore captured. Finally, as the standard microfabrication techniques allow patterns to be repeated on a single substrate, a three channel scheme is implemented in this first integrated prototype. This is shown in Fig. 4.7 (top view). Furthermore, integration with microfluidic channels on top of the device is an envisioned possibility.

4.3.2 Optical Testbench for Integrated SPR

To mount the testbench for the integrated SPR sensor, a set of passive optical components, optomechanical supports and a laser source are employed. The schematic and an actual photograph are shown respectively in Fig. 4.8.

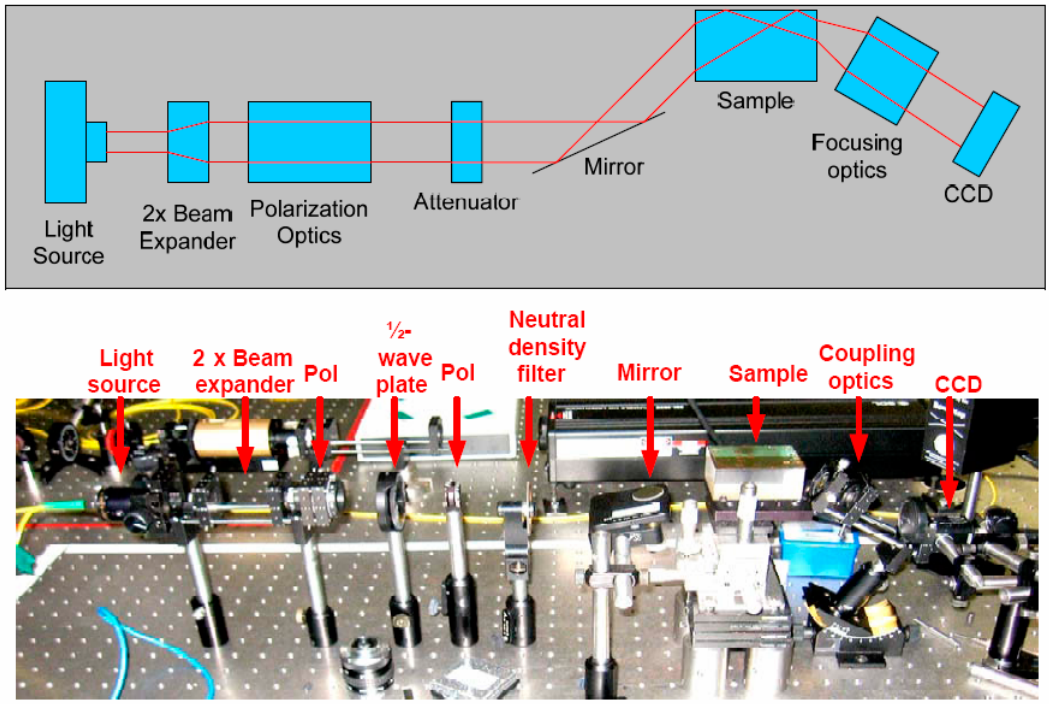

Figure 4.8 – Testbench for the integrated SPR sensor [4.8].

The light source consists of a monochromatic SDL 8360 laser diode whose lasing wavelength is centered at 852nm [4.8]. The light coming from the fiber is coupled and collimated in free-space. Subsequently, the expander formed with two lenses is responsible to reshape the beam to 2mm of diameter so incident light can cover the whole diffractive mirror at 70º. A transverse magnetic polarization is selected via a half-wave plate followed by an available polarizer. The intensity is variably reduced with a neutral density filter in order to avoid damage occurring at the detector. The integrated SPR device is placed on an optomechanical positioning stage with degrees of freedom in all three dimensions permitting precise alignments to one of the three available sensing channels on the SPR sensor. Finally, some focusing optics are used to project the light onto the screen of a Watec 502B monochrome CCD camera that has a sensing area of 5mm x 8mm.

Since the sensor is to be used as a cheap, compact and disposable device outside the laboratory, there is concern about the size of the overall system including the sources and detectors. In fact, the sensing elements, as well as the surrounding optics, can be miniaturized and mass reproduced using commercially available packaging techniques. For example, the substrate is only needed for its top and sides and is extremely flat, thus, it can be fabricated using suitable injection molding and imprinting process with a polymer material [4.8]. The size of the testbench can also be miniaturized by employing a convenient packaging to include a diode laser, the collimating optics, a photodetector and some specialized signal processing electronics. This will prevent users from worrying about the alignment issues of the overall system when porting the system from a place to another.

4.3.3 Experimental Results with NaCl

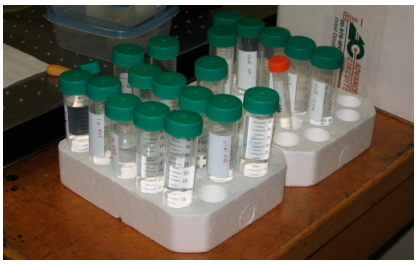

Figure 4.9 – Prepared Solutions

NaCl Concentration (M)	Refractive index (RIU)
0	1.3288
1	1.3387
2	1.3535
3	1.3655

Table 4.1 - Selected values of refractive index at different molar concentrations [4.8]

During the experiment, the bias current of the laser is set above the threshold so lasing would occur to ensure sufficient optical power to be delivered to the sensor. The neutral density filter is rotated to the appropriate position to avoid saturation of the CCD. The entire process can be monitored in real-time. Then, various prepared NaCl solutions ranging from 0.1M to 4M are used for the characterization of the SPR sensor. Initially, the sensor contains only distilled water solution in its sample holder. As NaCl of increasing molarity is added, the local refractive index above the metal changed. This can be seen in the captured images in Fig. 4.7 which show the normalized reflection intensities scanned across an angular range of 15°. The horizontal axis denotes the

angular span whereas the vertical axis is the spatial dimension. A reading of the reflection minimum only requires one horizontal slice of the images.

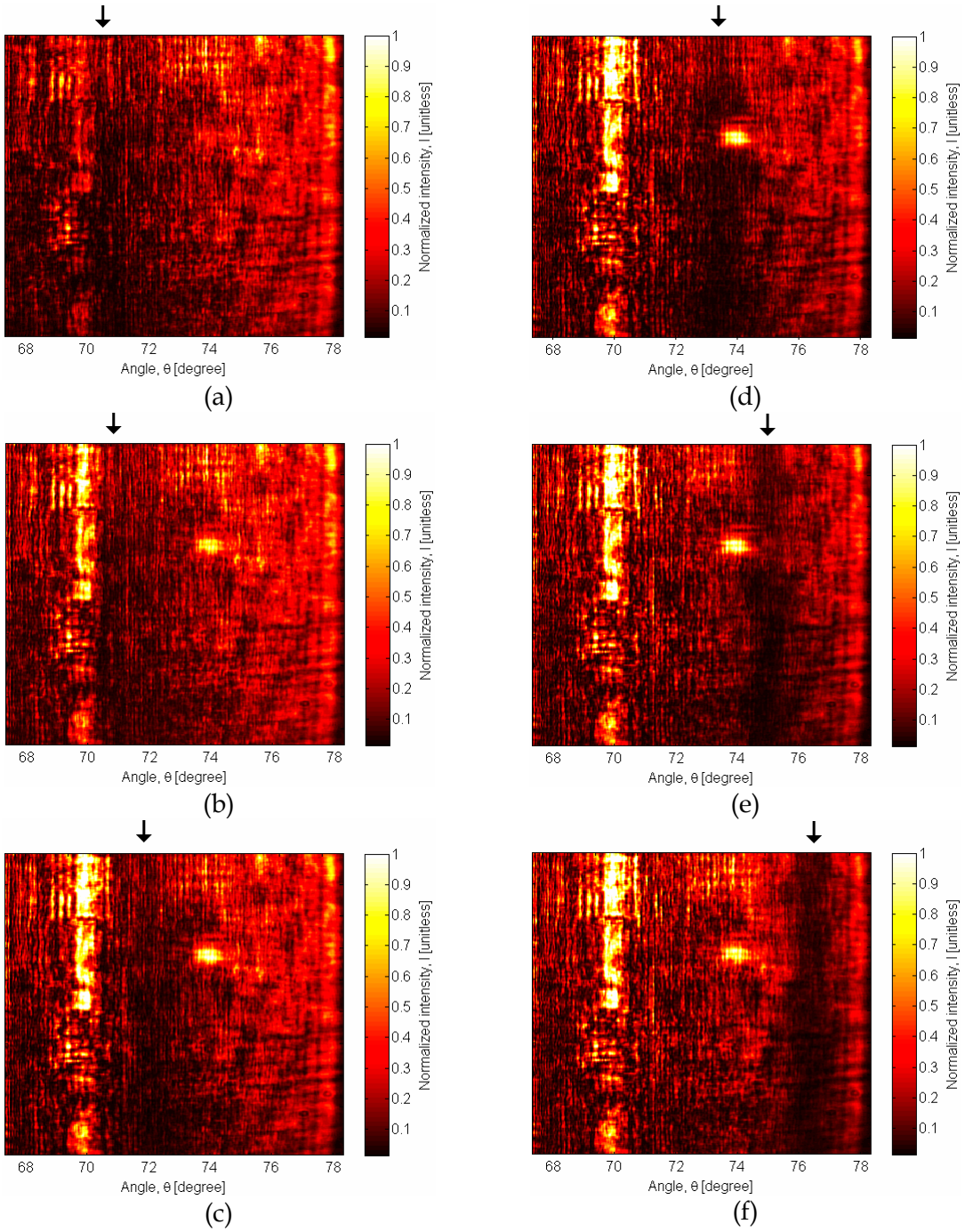

Figure 4.10 – Captured images showing the locations of the dips (denoted by arrows) caused by absorption of light by the surface plamons. Different solution media used are (a) distilled water and NaCl solution of different molarities: (b) 0.5M (c) 1M (d) 2M (e) 3M (f) 4M.

Since this sensor is a 1D imaging system, variations across the vertical axis don't convey more information. The intensity levels of the images are normalized with respect to a measurement taken when the sensing layer is air. The dark vertical line indicated by an arrow is the plasmon dip – angular positions that have a reflection intensity minimum since most of the photon energy has been transferred to the metal surface. As the resonant condition is perturbed by adding increasing molar concentration of NaCl, the angle that excites the plasmons varied, thus confirming the possibility of using surface plasmon resonance as an index-of-refraction sensor.

The quality of the images captured was affected by problems encountered, the first being that this first prototype was unintentionally designed to allow the zero-order diffraction to cause interference fringes to the output. A second problem was the manipulation of the highly sensitive surface. The experiment required swapping of samples for tests at different concentrations, and involved manually cleaning off the previous sample at each stage. Due to the softness of gold, scratches were left on the surface while manually wiping off the NaCl solutions (a bright spot caused is seen). The first prototype was tested many times using different solutions for initial characterization – the final product will be disposable and would not have such cleansing problems. Another problem resulted from the fact that the gold layer had peeled off over the period, thus needing a second deposition of gold surface with sputtered Titanium adhesion layer. In fact, this required the disassociation of the slab and the fused silica layer, and a reassembly involving an injection of index matching fluid in-between the layers. This manual process of joining the two pieces without leaking the index matching fluid into the air gap had proven to be laborious and had taken many attempts.

4.3.4 Sensitivity of the Sensor

An estimate of the sensitivity of this sensor is provided. The angular sensitivity S_θ is defined [4.1] as the slope between the angle and refractive index change, that is,

$$S_\theta = \partial\theta / \partial n \tag{4.3.1}$$

The unit for the angular sensitivity is expressed in degrees per refractive index unit (°/RIU). To automate the extraction of the angular positions of the plasmon dip from the images in Fig. 4.10, a simple centroid algorithm [4.11] is employed. Essentially, a weighted average of the intensities of all pixels along a horizontal slice with respect to a threshold value I_{th} is calculated to obtain the geometric center of the reflection intensity minimum. The mathematical expression is given by

$$\theta_{cen} = \frac{\sum_m \theta_m (I_{th} - I_m)}{\sum_m (I_{th} - I_m)} \tag{4.3.2}$$

where I_m and θ_m denote respectively the intensity and angular position at the mth pixel.

Using the known values of refractive indices from Table 4.1, the location of the plasmon dip has been extracted for a horizontal slice. In Fig. 4.11, the change in angle of incidence versus the sensing layer refractive index of the NaCl solution is plotted. A linear dependence is observed. From the trend line, the slope gives an estimated angular sensitivity of S_θ ~ 126°/RIU. As a comparison, the theoretical sensitivity for an angular SPR sensor reported in [4.12] is 97 °/RIU.

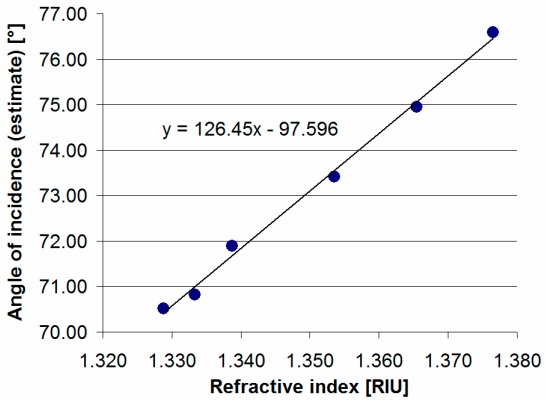

Figure 4.11 – Sensitivity curve for the integrated SPR sensor.

4.4 System #2: Combined Wavelength-Angle 2D SPR Sensor

4.4.1 Device Motivations

As a step toward the observation of a surface plasmon bandgap, we need a second SPR sensor that can provide an image of the reflection minima caused by the surface plasmons for light emerging from different angles and wavelengths near the resonance condition. In other words, there is a need for a dual modulated optical system which displays a reflectance/dispersion curve. The device which satisfies this need is presented in this section (Fig. 4.1 (b)) and shall be referred to as the "2D SPR sensor with combined wavelength-angle modulation", or for short, "2D SPR sensor". It is constructed using bulk free-space optical components.

The setup employs the Krestchmann configuration so the coupling of photons to surface plasmons can either be the simple prism coupling scheme or the indirect grating coupling scheme depending whether a flat or a corrugated gold metal is placed on top of the prism. The first step after the construction of this sensor is to observe the dispersion curve of the surface plasmons on a flat metal surface. The second step is to observe the surface plasmon bandgap offered by a sinusoidal grating. At the time of writing of this thesis, only a flat metallic gold surface has been mounted and tested. According to a numerical work from Alleyne et al. [4.7], the metal grating needs to follow a sinusoidal profile with a corrugation height in the order of tens of nanometers and a periodicity of few hundred nanometers. Such gratings can be prepared by electron-beam lithography.

4.4.2 Components of the Sensor

The essential components that are used to construct the 2D SPR sensor are described here. The optical components and their respective alignment are illustrated in Fig. 4.12. Fig. 4.13 (a)-(d) show the actual photographs of the components.

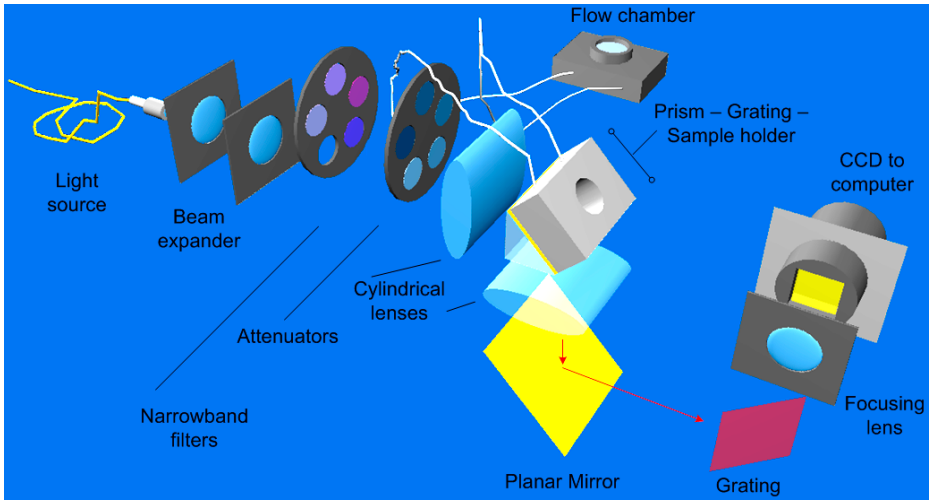

Figure 4.12 – Simplified schematics of the whole 2D sensor.

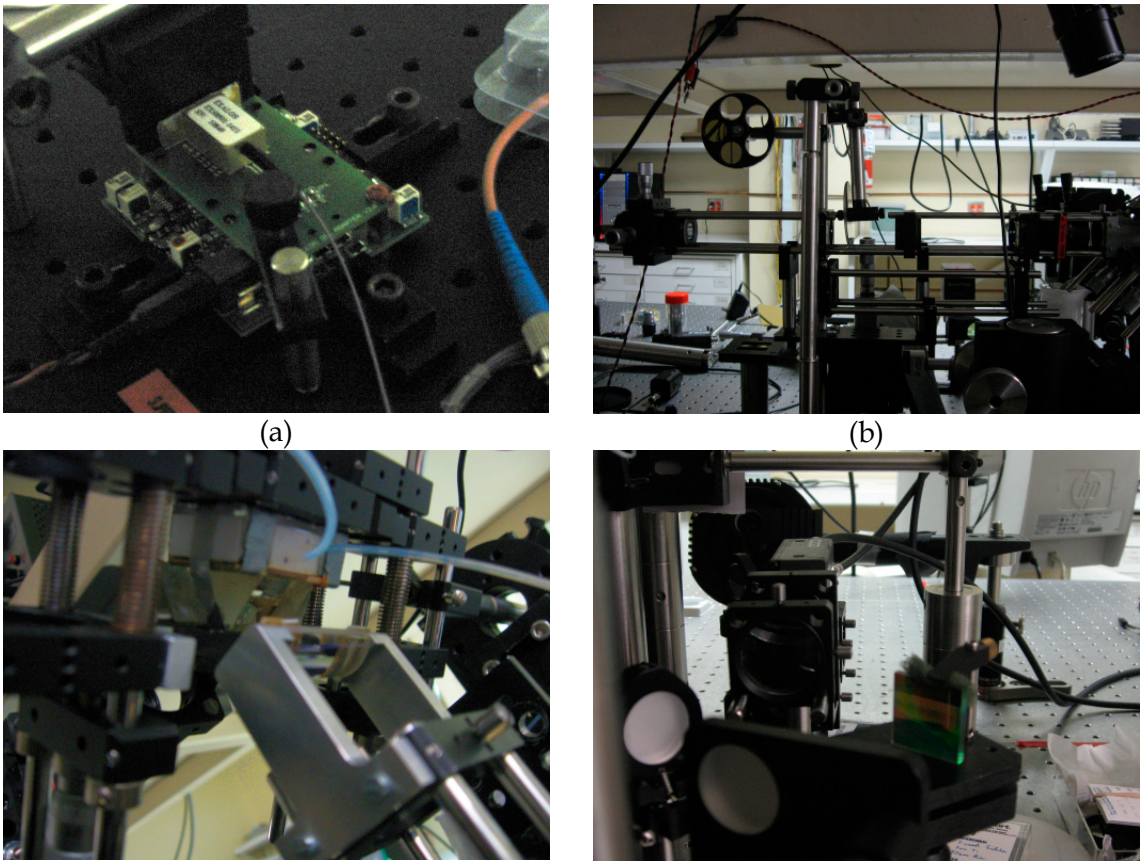

(a) (b)

(c) (d)

Figure 4.13 – Snapshots of various components of the 2D SPR Sensor: (a) Superluminescent Light Emitting Diode with its driver (b) Oz Coupler, beam expander, attenuator and filters (c) mechanical support that holds the prism, grating and the flow chamber in place, cylindrical lens (d) diffraction grating, mirrors and CCD camera.

The light source in this SPR system is a Superluminescent Light Emitting Diode (SLED) from Exalos, (EXS8501-1411) [4.13]. This light source combines the advantages of semiconductor lasers and light emitting diodes, namely: high output power, broadband spectrum and low temporal coherence. The central wavelength is 850nm and the full width at half maximum (FWHM) is 50nm. The output is through a single mode fiber, with 1.2mW of power.

A fiber optics polarization independent isolator (from Oz Optics, FOPI-11-11-850-5/125-S-40-3A3A-1-1-25 [4.14]) is connected next to the SLED to prevent damages resulting from back reflection into the light source. The isolator contains a free space Faraday rotator with some polarizing optics and is fiber pigtailed. This particular polarization independent isolator has insertion loss that is independent of input polarization. Subsequently, the propagating light (Pigtailed PolaRITE, from General Photonics [4.15]) enters a manual pigtailed fiber polarizer. This component controls the polarization of light from a single mode fiber by inducing birefringence via an applied pressure. The polarization is set to the TM mode in order to observe the plasmon dip.

Similarly to the integrated sensor, a beam expander formed by few spherical lenses and attenuators are required for beam shaping and intensity control. The collimated beam radius is about 1mm. Two identical BK7 plano-convex cylindrical lenses are responsible to focus the collimated beam with a 15° of angular spread and collimate the beam back at the reflection end. The focal length and the transverse dimensions of the cylindrical lenses are respectively 19.00mm and 32.0mm × 16.0mm. They are purchased from Thorlabs [4.16] and their part number is LJ1095L2-B.

The momentum matching to surface plasmon is achieved via an equilateral SF11 prism, as discussed earlier. After dropping a small amount of index matching fluid, a flat metallic slab is placed on top of the prism. The incident beam focus at the prism-metal interface makes an angle of 50° as shown in Fig. 4.14 below. Finally, a blazed holographic diffraction grating located in front of the CCD camera is responsible for the

spectral modulation (Edmund Optics, J47-560 [4.17]). The sensor is designed to image 50nm of wavelength and 15° of angles, centered at 850nm.

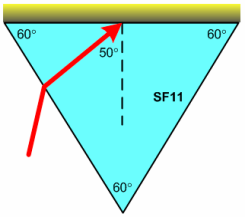

Figure 4.14 – Focusing angle at the prism-metal interface.

Standard opto-mechanical supports are used to hold the components together, with the flexibility to align the setup. The main mechanical supports that hold the cylindrical lenses and the prism-grating-sample holder are custom-made and their schematic is displayed in Appendix C. A flow chamber is connected to the sample holder in order for the solution to be pumped in and out without removing the apparatus at each change of solution.

4.4.3 Experimental Results with NaCl

The testing of the 2D SPR sensor uses the same NaCl solutions as shown in Fig. 4.7. the output light is captured using a photodetector for the distilled water and the various concentrations of NaCl. The images obtained using the 2D SPR sensor for different solutions are displayed in Fig 4.12. For this sensor, the images shown are normalized reflection intensities that vary in two axes. The vertical axis denotes the wavelength span, about 50nm around the central wavelength of 850nm. The horizontal axis gives an angular range of about 12° around the central angle of 50°. Unlike the images captured using the integrated sensor (Fig. 4.10), the images also contain the reflection intensities at other wavelengths, as this is necessary to see the dispersion curves. Again, the images are normalized with respect to that measured in air. Narrowband filters at various wavelengths were used to determine the wavelength range of the images. For the angular range, an approximation is given based on the optical components and simple ray tracings. In Fig. 4.15 (a), a reflection minimum is observed at 850nm around the center angle of 50°. As the sensing solution is replaced by

NaCl solutions of increased molarities in Fig. 4.15 (b)-(e), the shifting of the reflection minimum curves is observed, similarly to the experimental results obtained from the integrated SPR sensor. These experimental images are similar to those obtained from simulations (Fig. 4.6 (a)).

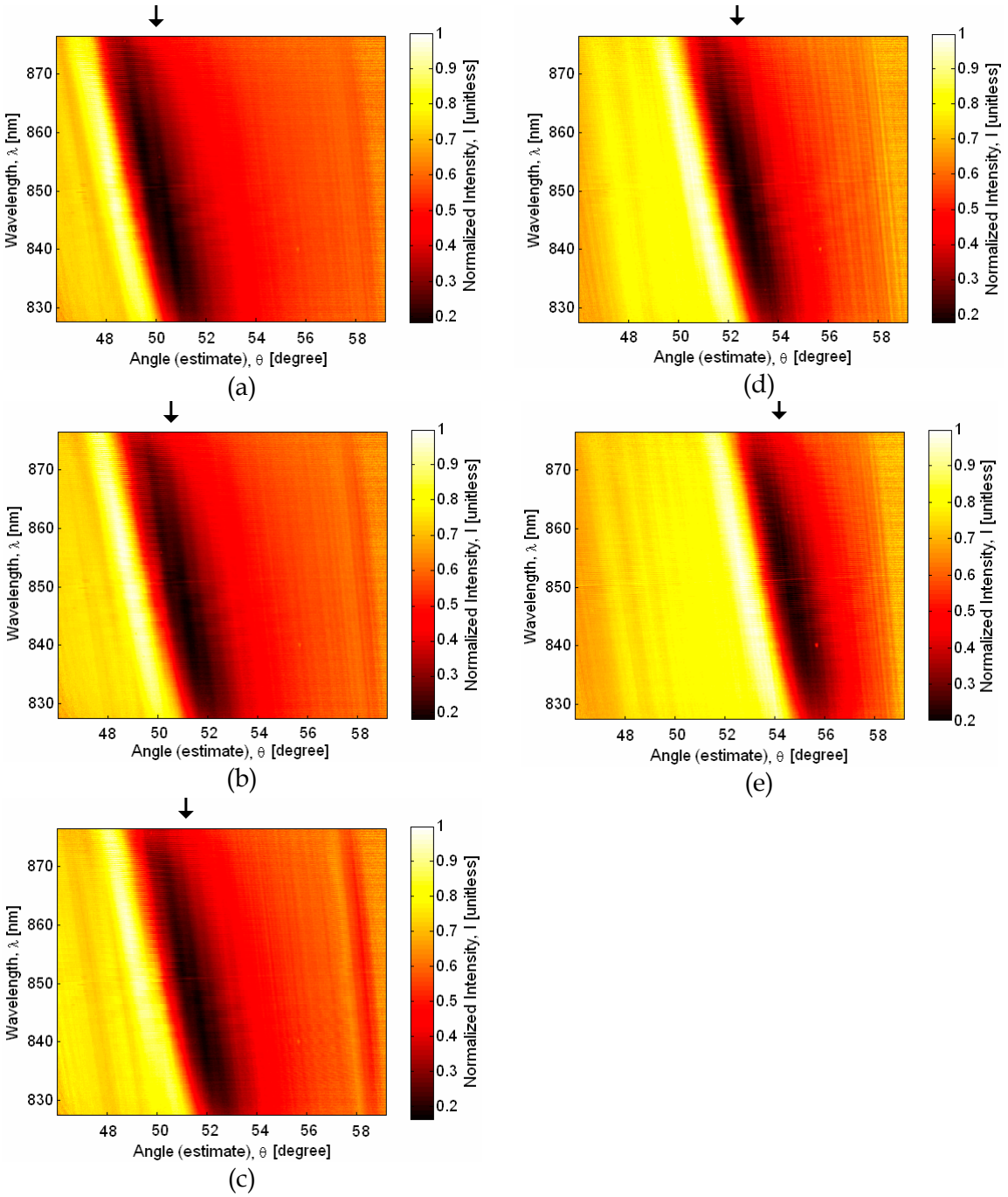

Figure 4.15 – Captured images showing the dispersion curve of the surface plasmon for different solutions: (a) distilled water (b) 0.5M NaCl solution (c) 1M NaCl solution (d) 2M NaCl solution (e) 4M NaCl solution.

4.4.4 Sensitivity of the Sensor

As a quick initial comparison between the two sensors presented in this chapter, the estimation of the angular sensitivity presented for the integrated SPR sensor (in Subsection 4.3.4) is repeated here for a horizontal slice (850nm) of the images provided in Fig. 4.15. The dependence of the angular shifts to refractive index changes in the sensing layer is linear as well.

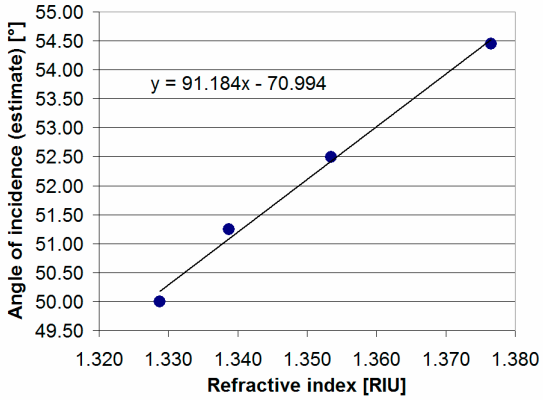

Figure 4.16 - Sensitivity curve for the 2D SPR sensor.

From the trend line of Fig. 4.16, the slope gives an estimated angular sensitivity of $S_\theta \sim 91^o$/RIU. This lower result should not be alarming since the high sensitivity of the 2D sensor is expected to arise from the observation of the surface plasmon bandgap. Only then, a thorough comparison between the 2D SPR sensor with or without a corrugated metallic surface should be made. It is also to be noted that the use of traditional one-dimensional dip-finding algorithm (such as the centroid method) does not take into account the two-dimensional nature of the dispersion curves with or without a bandgap. A complete extraction of the two-dimensional features from dispersion images will be able to identify the location of the surface plasmon bandgap. Alleyne et al. has been working on such image processing technique using principal value decomposition (PCA) [4.18].

In summary, the first step of achieving a dual-modulation SPR sensor with a flat surface is demonstrated. The next step will be the observation and the real-time tracking of the surface plasmon bandgap that is intended to provide additional sensitivity.

4.6 References

[4.1] J. Homola, ed., *Surface Plasmon Resonance Based Sensors* (Springer-Verlag, Berlin, 2006).

[4.2] E. Kretschmann, H. Raether, "Radiative decay of non-radiative surface plasmons excited by light," *Z. Naturforsch.*, vol. 23A, pp. 2135–2136, 1968.

[4.3] K. Kurihara and K. Suzuki, "Theoretical Understanding of an Absorption-based Surface Plasmon Resonance Sensor Based on Kretchmann's Theory," *Anal. Chem.*, vol. 74, pp. 696-701, 2002.

[4.4] X.D. Hoa, A.G. Kirk, and M. Tabrizian, "Towards integrated and sensitive surface plasmon resonance biosensors: A review of recent progress," *Biosensors and Bioelectronics*, vol. 23, pp. 151-160, 2007.

[4.5] W.L. Barnes, T.W. Preist, S.C. Kitson, and J.R. Sambles, "Physical origin of photonic energy gaps in the propagation of surface plasmons on gratings," Phys. Rev. B, vol. 54, pp. 6227-6244, 1996.

[4.6] W.L. Barnes, A. Dereux, and T.W. Ebbesen, "Surface Plasmon Subwavelength Optics," *Nature*, vol. 424, pp. 824-830, 2003.

[4.7] C.J. Alleyne, A.G. Kirk, R.C. McPhedran, N.-A.P. Nicorovici, and D. Maystre, "Enhanced SPR sensitivity using periodic metallic structures," *Optics Express*, vol. 15, pp. 8163-8169, 2007.

[4.8] M.Z. Khalid, *A highly integrated Surface Plasmon Resonance Sensor based on a Focusing Diffractive Optic Element* (Master's thesis, McGill University, 2007).

[4.9] Z. Khalid, X. Hoa, C. Alleyne, M. Tabrizian, J. Beauvais, P. Charette, N.A. Nicorovici, R.C. McPhedran, A. G. Kirk, "Integrated Surface Plasmon Resonance Sensor with periodic nanostructures for sensitivity enhancement," *Proceedings of SPIE*, vol. 6450, 2007.

[4.10] C. Thirstrup, W. Zong, M. Borre, H. Neff, H.C. Pedersen, and G. Holzhueter, "Diffractive optical coupling element for surface plasmon resonance sensors," Sensors and Actuators B: Chemical, vol. 100, no. 3, pp. 299-309, 2004.

[4.11] G. G. Nenninger, M. Piliarik, and J. Homola, "Data analysis for optical sensors based on spectroscopy of surface plasmons," *Measurement Science & Technology*, vol. 13, no. 12, pp. 2038-2046, 2002.

[4.12] J. Homola, S. S. Yee, and G. Gauglitz, "Surface plasmon resonance sensors: review," *Sensors and Actuators B: Chemical*, vol. 54, pp. 3-15, 1999.

[4.13] "Oz Optics," http://www.ozoptics.com.

[4.14] "Exalos," http://www.exalos.com/.

[4.15] "General Photonics," http://www.generalphotonics.com/PLC-002.htm.

[4.16] "Thorlabs Inc.," http://www.thorlabs.com/.

[4.17] "Edmund Optics," http://www.edmundoptics.com/.

[4.18] C.J. Alleyne, A.G. Kirk, P.G. Charette, "High Accuracy Numerical Method for Index of Refraction Estimation with Surface Plasmon Bandgap Structures," in *Conference on Lasers and Electro-Optics / Quantum Electronics and Laser Science Conference and Photonic Applications Systems Technologies 2008 Technical Digest* (Optical Society of America), QTuJ7, 2008.

Chapter 5 – Sensing with Surface-Enhanced Raman Scattering

5.1 Introduction

Metallic nanostructures are used to enhance radiative processes such as fluorescence or Raman scattering [5.1, 5.2]. This chapter is focused on one particular enhancement effect, that of surface-enhanced Raman scattering (SERS), obtained by efficient arrangement of metallic nanospheres. A significant challenge is the ability to provide a rigorous electromagnetic measure describing the light-matter interaction of metallic nanosphere assemblies. We will use the generalized Mie Theory (or multiple-multipole method) to analyze the enhancement of near-fields. This method has been applied previously to study light scattering in colloids, but not for structures specifically designed for near-fields enhancement. Moreover, such implementation is not an easy one and the literature is often laden with differing conventions. By incorporating the plasmonic effects discussed in Chapter 3, a single and self-consistent formulation has been organized and implemented in this respect.

In Section 5.2, the enhancement of Raman scattering is briefly explained and the heuristics for an ultra sensitive molecular sensing modality is mentioned. The details of the complete implementation of the multiple-multipole method are laid out in Section 5.3. Section 5.4 describes the design of efficient field focusing assemblies for SERS from their simulation results.

5.2 Sensing Principle

Raman scattering is a light-matter interaction that occurs when an incident photon scatters inelastically from an atom or a molecule. Unlike the elastic scattering (Rayleigh scattering), this Raman effect occurs less frequently and the energy of the incident photon is altered after interaction. If the atom or molecule absorbs some of the

energy and promotes its energy state from a lower state $|m>$ to a higher state $|k>$ as illustrated in Fig. 5.1 (a), the frequency of light is red-shifted. This process is referred to as a *Stokes shift*. On the other hand, if the system is relaxed from a higher energy state to a lower one, the frequency of light is blue-shifted. In this case, the emitted photon is more energetic than the incident photon. This process is called *anti-Stokes shift* and is illustrated in Fig. 5.1 (b). Different from the process of fluorescence, a Raman scattering does not need to occur at resonance – the effect can take place for any frequency of light. For a quantum mechanical treatment of Raman scattering, please refer to these references [5.3, 5.4].

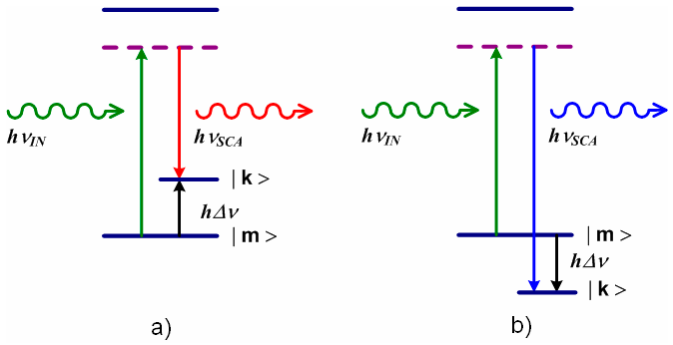

Figure 5.1 – Raman scattering Energy levels (a) Stokes shift (b) anti-Stokes shift. The dashed lines denote virtual states whereas the topmost lines represent the resonant energy levels.

In Raman spectroscopy, a laser source in the visible range is often used to illuminate the sample [5.5, 5.6]. The shift in frequency that represents the vibrational, rotational or electronic states, characteristic of the atoms or molecules under investigation, is used to identify the chemical composition of the given sample. However, despite its ability to reveal the chemical structural information, only about one in 10^5 photons is actually Raman scattered. Many samples include only minute quantities of the compounds in question, thus limiting the exercise of such weak effect. On the other hand, surface-enhanced Raman Scattering (SERS) can enhance the weak Raman scattering by several orders of magnitude by depositing the molecule under investigation near the surface of metal colloids. It is believed that the increase in Raman scattering is due to a combination of a chemical and electromagnetic enhancement mechanisms [5.7]. The chemical enhancement is explained as a charge-transfer process between the metal and the molecule - an electronic coupling between them. The

estimated enhancement is in the order of 10 to 100. On the other hand, the overlap of evanescent near-fields between metal clusters at the so-called "hot-spots" is believed to be the origin for the electromagnetic enhancement. The Raman scattered optical power due to SERS scales with the fourth power of electric field enhancement [5.8, 5.9],

$$P_S(\nu_S) \propto \left|\mathbf{E}_{focal}\right|^4 / \left|\mathbf{E}_0\right|^4 \tag{5.2.1}$$

where ν_s is the scattered photon frequency. Enhancements in the orders of 10^6 - 10^7 have been documented [5.10, 5.7]. For this reason, the question of how metal particles should be arranged with respect to each other to produce the strongest electric field enhancement at the "hot-spots" is the main problem of this part of the work.

The enhanced Raman scattering can be used for sensing [5.11]. Molecular tags with known Raman spectra such as Rhodamine 6G [5.12] presented in Fig. 5.2 can be functionalized with the molecule under investigation. Then, on the surface of metallic nanostructures that serve as SERS-active platforms [5.13], the measurement of the enhanced Raman spectra is used for identification.

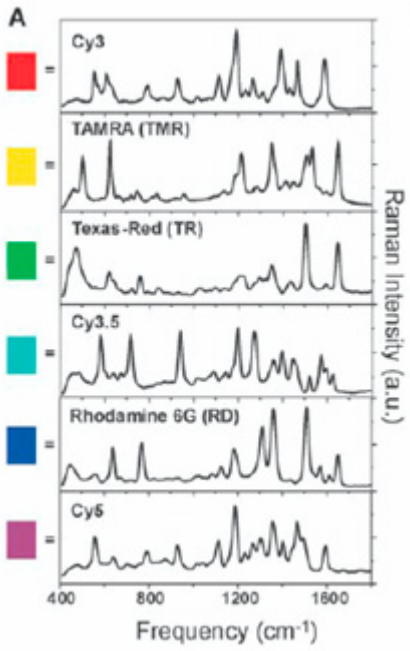

Figure 5.2 – Raman spectra of common tags [5.12].

5.3 Implementation of the Multiple-Multipole Method

5.3.1 Overall Formalism

We will now solve the electromagnetic scattering problem of aggregates of N_s small spheres, each characterized by a normalized radius $x^j = k\,a^j = 2\pi\, m_{medium}\, a^j / \lambda_{vacuum}$, a normalized position $\mathbf{R}^j = (X^j, Y^j, Z^j)$ and a relative refractive index $m^j = m^j_{abs} / m_{medium}$. We use harmonic time dependence $\exp(-i\omega t)$ for all field quantities. Mie theory accurately describes the scattering of uncoupled spheres, but generalization of Mie theory to multiple-multipoles is necessary to account for successive light scattering amongst nanospheres at sub-wavelength separations.

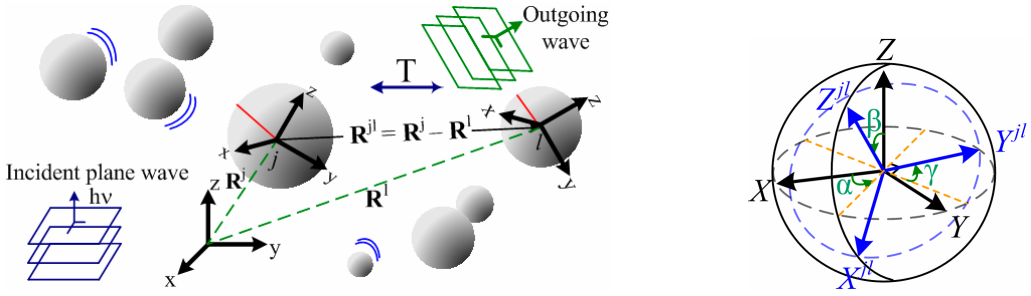

(a) (b)

Figure 5.3 – Depiction of the general problem. Each sphere is characterized by a radius a^j and refractive index m^j (a). The rotation scheme of a bisphere jl to the overall coordinate system (b).

The multiple-multipole theory, also known as the T-matrix method [5.14-5.16] begins with an expansion of the incident, scattered, and internal (to the sphere) electromagnetic field into the well known vector spherical harmonic basis $\mathbf{N}^{(1)}$, $\mathbf{M}^{(1)}$, $\mathbf{N}^{(3)}$, $\mathbf{M}^{(3)}$ [5.14, 5.17-5.19] about each sphere:

$$\begin{aligned}
\mathbf{E}^j_{sca} &= \sum_{n=1}^{\infty}\sum_{m=-n}^{n} iE_{mn}\left[a^j_{mn}\mathbf{N}^{(3)}_{mn}(j) + b^j_{mn}\mathbf{M}^{(3)}_{mn}(j)\right] \\
\mathbf{E}^j_{inc} &= -\sum_{n=1}^{\infty}\sum_{m=-n}^{n} iE_{mn}\left[p^j_{mn}\mathbf{N}^{(1)}_{mn}(j) + q^j_{mn}\mathbf{M}^{(1)}_{mn}(j)\right] \\
\mathbf{E}^j_{int} &= -\sum_{n=1}^{\infty}\sum_{m=-n}^{n} iE_{mn}\left[d^j_{mn}\mathbf{N}^{(1)}_{mn}(j) + c^j_{mn}\mathbf{M}^{(1)}_{mn}(j)\right]
\end{aligned} \tag{5.3.1}$$

$$\mathbf{H}_{sca}^{j} = \frac{1}{\eta}\sum_{n=1}^{\infty}\sum_{m=-n}^{n} E_{mn}[b_{mn}^{j}\mathbf{N}_{mn}^{(3)}(j) + a_{mn}^{j}\mathbf{M}_{mn}^{(3)}(j)]$$

$$\mathbf{H}_{inc}^{j} = -\frac{1}{\eta}\sum_{n=1}^{\infty}\sum_{m=-n}^{n} E_{mn}[q_{mn}^{j}\mathbf{N}_{mn}^{(1)}(j) + p_{mn}^{j}\mathbf{M}_{mn}^{(1)}(j)] \qquad (5.3.2)$$

$$\mathbf{H}_{int}^{j} = -\frac{1}{\eta^{j}}\sum_{n=1}^{\infty}\sum_{m=-n}^{n} E_{mn}[c_{mn}^{j}\mathbf{N}_{mn}^{(1)}(j) + d_{mn}^{j}\mathbf{M}_{mn}^{(1)}(j)]$$

where a_{mn}^{j}, b_{mn}^{j}, p_{mn}^{j}, q_{mn}^{j}, c_{mn}^{j} and d_{mn}^{j} are the expansion coefficients, $\eta = \eta_0 / m_{medium}$ is the wave impedance of the ambient medium, $\eta^{j} = \eta / m^{j}$ is the wave impedance in metal sphere *j*, and $\mathbf{N}^{(1)}$, $\mathbf{M}^{(1)}$ indicate vector spherical harmonics centered on the origin of sphere *j*. We assume here that the vector harmonics are defined at each sphere with respect to a common set of direction axes *x*, *y* and *z*. The complete scattered electric field is given by a sum over all N_s spheres,

$$\mathbf{E}_{sca} = \sum_{i}^{N_s} \mathbf{E}_{sca}^{j} \,. \qquad (5.3.3)$$

We assume a plane wave polarized in the +x-direction and propagating in the +z-direction, so that the non-trivial incident field coefficients are,

$$p_{1n}^{0} = q_{1n}^{0} = \frac{\exp(iZ^{j})}{2},\ p_{-1n}^{0} = -q_{-1n}^{0} = -\frac{\exp(iZ^{j})}{2n(n+1)} \qquad (5.3.4)$$

where we take as the spatial coordinates of the origin of sphere *j* with respect to the system origin. The prefactor $E_{mn} = |E_0| i^{n}(2n+1)(n-m)!/(n+m)!$, where $|E_0|$ is the magnitude of the incident wave, is introduced as a normalization constant to maintain numerical stability [5.14] and to maintain consistency with the single-sphere Mie theory, where $m = \pm 1$. In the above, the order *m* and the degree *n* are integers such that $-n \le m \le n$, and describes the multipole (i.e. dipole, quadrupole, etc.) nature of the electromagnetic field dressing each sphere. In numerical work, the harmonic degree is truncated to a finite number $1 \le n \le N$.

The central numerical problem is the efficient calculation of the scattered field coefficients a_{mn}^{j}, b_{mn}^{j} in a self-consistent manner that accounts for successive scattering between all nanospheres. Imposing the usual boundary conditions for electromagnetic

fields at the surfaces of the spherical particles gives a set of inhomogeneous linear equations for the coefficients a_{mn}^{j}, b_{mn}^{j} [5.14, 5.15],

$$\begin{aligned} a_{mn}^{j} &= \alpha_n^j \left(p_{mn}^{j} - \sum_{\substack{j=1 \\ j\neq l}}^{N_s} \sum_{\nu=1}^{\infty} \sum_{\mu=-\nu}^{\nu} \frac{E_{\mu\nu}}{E_{mn}} [a_{\mu\nu}^{l} A_{mn}^{\mu\nu}(\mathbf{R}^{jl}) + b_{\mu\nu}^{l} B_{mn}^{\mu\nu}(\mathbf{R}^{jl})] \right) \\ b_{mn}^{j} &= \beta_n^j \left(q_{mn}^{j} - \sum_{\substack{j=1 \\ j\neq l}}^{N_s} \sum_{\nu=1}^{\infty} \sum_{\mu=-\nu}^{\nu} \frac{E_{\mu\nu}}{E_{mn}} [a_{\mu\nu}^{l} B_{mn}^{\mu\nu}(\mathbf{R}^{jl}) + b_{\mu\nu}^{l} A_{mn}^{\mu\nu}(\mathbf{R}^{jl})] \right) \end{aligned} \tag{5.3.5}$$

where the quantities a^j_n and β^j_n are the single sphere Lorenz-Mie coefficients and $A_{mn}^{\mu\nu}$ and $B_{mn}^{\mu\nu}$ are the coefficients of the vector harmonic addition theorem [5.14, 5.15, 5.20] that are functions of the inter-origin vector $\mathbf{R}^{jl} = \mathbf{R}^{l} - \mathbf{R}^{j}$.

The system of Eq. (5.3.5) is often re-written in block form in which the matrix **T** represents an interaction operator for the vector harmonic coefficients associated with each sphere,

$$\mathbf{a}^{j} + \sum_{\substack{i=1 \\ i\neq j}}^{N_s} \mathbf{T}^{ji} \mathbf{a}^{i} = \mathbf{p}^{j} \text{ or } \left(\mathbf{1} + \mathbf{T}\right)\mathbf{a} = \mathbf{p} \tag{5.3.6}$$

with the scattering vector $\mathbf{a}^j = [a_{mn}^j \; b_{mn}^j]$, the incident field vector $\mathbf{p}^j = [\alpha_n^j \; p_{mn}^j \;\; \beta_n^j \; q_{mn}^j]$ and $\mathbf{T}^{ji}$ being composed of elements of the form $(E_{\mu\nu}/E_{mn})\alpha_n^j \; A_{mn}^{\mu\nu}$. In the limit of weak interaction between spheres, Mie theory is asymptotically recovered, $\mathbf{a} = (\mathbf{1}\text{-}\mathbf{T}\text{+}\mathbf{T}^2\text{-}\mathbf{T}^3\text{+}\ldots)\,\mathbf{p}$. The strong interaction between metal nanospheres in close proximity, illuminated close to plasmon-polariton resonance, prohibits the use of such an expansion. In our work, the linear system of Eq. (5.3.6) was solved using a biconjugate gradient method with commercially available software.

5.3.2 Numerical Evaluation of Coefficients

The Lorenz-Mie coefficients for sphere j depend on the normalized radius x^j and relative refractive index m^j as,

$$\alpha_n^j = \frac{m^j \psi_n'(x^j)\psi_n(m^j x^j) - \psi_n(x^j)\psi_n'(m^j x^j)}{m^j \xi_n'(x^j)\psi_n(m^j x^j) - \xi_n(x^j)\psi_n'(m^j x^j)}$$
$$\beta_n^j = \frac{\psi_n'(x^j)\psi_n(m^j x^j) - m^j \psi_n(x^j)\psi_n'(m^j x^j)}{\xi_n'(x^j)\psi_n(m^j x^j) - m^j \xi_n(x^j)\psi_n'(m^j x^j)} \tag{5.3.7}$$

where $\psi_n(z) = z\, j_n(z)$ and $\xi_n(z) = z\, h_n^{(1)}(z)$, with j_n and $h_n^{(1)}$ the spherical Bessel and spherical Hankel functions of first kind.

The vector harmonic addition coefficients are defined implicitly through the vector harmonic addition theorem [5.14, 5.15, 5.20, 5.21] for decomposing the harmonics $\mathbf{N}^{(3)}(j)$, $\mathbf{M}^{(3)}(j)$ about an origin at $\mathbf{R}^j$ into harmonics $\mathbf{N}^{(1)}(l)$, $\mathbf{M}^{(1)}(l)$ about the origin $\mathbf{R}^l$,

$$\mathbf{M}_{mn}^{(3)}(j) = \sum_{\nu=1}^{\infty}\sum_{\mu=-\nu}^{\nu}\left[A_{\mu\nu}^{mn}(\mathbf{R}^{jl})\,\mathbf{M}_{\mu\nu}^{(1)}(l) + B_{\mu\nu}^{mn}(\mathbf{R}^{jl})\;\mathbf{N}_{\mu\nu}^{(1)}(l)\right]$$
$$\mathbf{N}_{mn}^{(3)}(j) = \sum_{\nu=1}^{\infty}\sum_{\mu=-\nu}^{\nu}\left[B_{\mu\nu}^{mn}(\mathbf{R}^{jl})\,\mathbf{M}_{\mu\nu}^{(1)}(l) + A_{\mu\nu}^{mn}(\mathbf{R}^{jl})\,\mathbf{N}_{\mu\nu}^{(1)}(l)\right]. \tag{5.3.8}$$

A variety of methods can be used to calculate the tensor coefficients. Efficient numerical evaluation of these addition coefficients is critical. In our work we have combined several techniques briefly described in the following. We have used Mackowski's strategy of decomposing general translation coefficients into rotations and axial translations,

$$A_{\mu\nu}^{mn}(\mathbf{R}^{jl}) \leftarrow (R_{\mu m}^{(n)})^{-1} A_{\mu\nu}^{mn}\left(0,0,\left|\mathbf{R}^{jl}\right|\right) R_{\mu m}^{(n)}$$
$$B_{\mu\nu}^{mn}(\mathbf{R}^{jl}) \leftarrow (R_{\mu m}^{(n)})^{-1} B_{\mu\nu}^{mn}\left(0,0,\left|\mathbf{R}^{jl}\right|\right) R_{\mu m}^{(n)} \tag{5.3.9}$$

as illustrated in Fig. 5.3. The rotation matrix $R_{\mu m}^{(n)}(\alpha,\beta,\gamma)$ is defined by the Euler angles $\alpha = \operatorname{acos}(X^{jl}/|\mathbf{R}^{jl}|)/\sin\beta$, $\beta = \operatorname{acos}(Z^{jl}/|\mathbf{R}^{jl}|)$ and $\gamma = 0$ for rotating the angular momentum z-axis into alignment with the inter-origin vector $\mathbf{R}^{jl} = \mathbf{R}^l - \mathbf{R}^j$. The rotation matrix elements are,

$$R_{\mu m}^{(n)}(\alpha,\beta,\gamma) = \frac{E_{mn}}{E_{\mu n}}\frac{F_{\mu n}}{F_{mn}} D_{\mu m}^{(n)}(\alpha,\beta,\gamma) \tag{5.3.10}$$

with normalization constants

$$E_{mn} = \left|E_0\right| i^n (2n+1)(n-m)!/(n+m)! \tag{5.3.11}$$

$$F_{mn} = (-1)^m \sqrt{(2n+1)(n-m)!}/(4\pi(n+m)!) \tag{5.3.12}$$

and the rotation operator of quantum mechanics [5.22]

$$D^{(n)}_{\mu m}(\alpha,\beta,\gamma) = e^{ik\gamma}\, d^{(n)}_{\mu m}(\beta)\, e^{im\alpha} \tag{5.3.13}$$

$$d^{(n)}_{\mu m}(\beta) = \left[\frac{(n+\mu)!(n-\mu)!}{(n+m)!(n-m)!}\right]^{\frac{1}{2}} (\cos\frac{\beta}{2})^{\mu+m} (\sin\frac{\beta}{2})^{\mu-m} P^{(\mu-m,\mu+m)}_{n-\mu}(\cos\beta) \tag{5.3.14}$$

composed of the Jacobi Polynomial evaluated directly as,

$$P^{(\alpha,\beta)}_n(x) = 2^{-n}\sum_{\nu=0}^{n}\binom{n+\alpha}{\nu}\binom{n+\beta}{n-\nu}(x-1)^{n-\nu}(x+1)^{\nu}\ . \tag{5.3.15}$$

The symmetry relations $d^{(n)}_{\mu m}(\beta) = (-1)^{\mu-m} d^{(n)}_{-\mu-m}(\beta)$ and $d^{(n)}_{\mu m}(\beta) = (-1)^{\mu-m} d^{(n)}_{m\mu}(\beta)$ were used to further reduce computational time.

The coefficients for positive axial translation of vector harmonics by a distance $|\mathbf{R}^{jl}|$ were calculated using the following expressions [5.20],

$$A^{m\nu}_{mn} = (-1)^{m+n}\frac{2n+1}{2n(n+1)}\sum_{p=|n-\nu|}^{n+\nu}(-1)^q[n(n+1)+\nu(\nu+1)-p(p+1)]\,a(-m,n,m,\nu,p)\,h^{(1)}_p(\mathbf{R}^{jl})$$

$$B^{m\nu}_{mn} = (-1)^{m+n}\frac{2n+1}{2n(n+1)}2im\,|\mathbf{R}^{jl}|\sum_{p=|n-\nu|}^{n+\nu}(-1)^q\ a(-m,n,m,\nu,p)h^{(1)}_p(\mathbf{R}^{jl}) \tag{5.3.16}$$

$$q = (n+\nu-p)/2 \tag{5.3.17}$$

where the Gaunt coefficients $a_p = a(m',n,-m',\nu,p)$, $p = n+\nu$, $n+\nu-2,\ldots|n-\nu|$, were calculated using Bruning and Lo's recursive technique [5.16],

$$\alpha_{p-3}a_{p-4} - (\alpha_{p-2}+\alpha_{p-1}-4m'^2)a_{p-2} + \alpha_p a_p = 0 \tag{5.3.18}$$

$$\alpha_p = \frac{[(n+\nu+1)^2-p^2][p^2-(n-\nu)^2]}{4p^2-1} \tag{5.3.19}$$

$$a_{n+\nu} = \frac{(2n-1)!!(2\nu-1)!!}{(2n+2\nu-1)!!}\frac{(n+\nu)!}{(n-m')!(\nu+m')!} \tag{5.3.20}$$

$$a_{n+\nu-2} = \frac{(2n+2\nu-3)}{(2n-1)(2\nu-1)(n+\nu)}[n\nu-m'^2(2n+2\nu-1)]a_{n+\nu} \tag{5.3.21}$$

where $(2q-1)!!=(2q-1)(2q-3)\cdots 3\cdot 1\,;(-1)!!\equiv 1$. The simplicity of our chosen strategy arises from the fact that axial translations are diagonal in harmonic order $m=\mu$, while the rotations are diagonal in harmonic degree $\eta=\nu$.

5.3.3 Numerical Evaluation of Far-fields Quantities

Once the scattered wave coefficients a_{mn}^{j}, b_{mn}^{j} are calculated, quantities of direct physical interest are evaluated easily. The normalized far-field scattering, extinction and absorption cross-sections (also known as the efficiencies) were calculated [5.14, 5.15],

$$Q_{sca}=\frac{4\pi}{Gk^2}\sum_{n=1}^{\infty}\sum_{m=-n}^{n} n(n+1)(2n+1)\frac{(n-m)!}{(n+m)!}(|\,a_{mn}^{T}\,|^2+|\,b_{mn}^{T}\,|^2) \tag{5.3.22}$$

$$Q_{ext}=\frac{4\pi}{Gk^2}\sum_{n=1}^{\infty}\sum_{m=-n}^{n} n(n+1)(2n+1)\frac{(n-m)!}{(n+m)!}\mathrm{Re}\{p_{mn}^{0*}a_{mn}^{T}+q_{mn}^{0*}b_{mn}^{T}\} \tag{5.3.23}$$

$$Q_{abs}=Q_{ext}-Q_{sca} \tag{5.3.24}$$

where $G=\pi\sum_{j}^{N_s}(a^j)^2$ is the geometric area of each assembly under broadside illumination. Eqs. (5.3.22) and (5.3.24) make use of a single set of total scattered field coefficients a_{mn}^{T}, b_{mn}^{T} for an expansion about a sphere (centered at $\mathbf{R}^l$) that is chosen as an origin,

$$\begin{aligned} a_{mn}^{T}&=\sum_{j=1}^{N_s}\sum_{\nu=1}^{\infty}\sum_{\mu=-\nu}^{\nu}[A'^{\mu\nu}_{mn}(\mathbf{R}^{jl})\,a_{\mu\nu}^{j}+B'^{\mu\nu}_{mn}(\mathbf{R}^{jl})\,b_{\mu\nu}^{j}]\\ b_{mn}^{T}&=\sum_{j=1}^{N_s}\sum_{\nu=1}^{\infty}\sum_{\mu=-\nu}^{\nu}[A'^{\mu\nu}_{mn}(\mathbf{R}^{jl})\,b_{\mu\nu}^{j}+B'^{\mu\nu}_{mn}(\mathbf{R}^{jl})\,a_{\mu\nu}^{j}]\,. \end{aligned} \tag{5.3.25}$$

where the $A'^{\mu\nu}_{mn}$, $B'^{\mu\nu}_{mn}$ coefficients are calculated as $A^{\mu\nu}_{mn}$, $B^{\mu\nu}_{mn}$, but with spherical Hankel functions $h_n^{(1)}$ replaced by spherical Bessel functions j_n in Eqs. (5.3.16), as appropriate to translation of outward propagating vector harmonics $\mathbf{N}^{(3)}$, $\mathbf{M}^{(3)}$ [5.20].

5.3.4 Numerical Evaluation of Near-fields

In order to compare the enhancement efficiencies from sets of nanosphere assemblies, the electric field enhancement, defined as the ratio of $|\,\mathbf{E}_{sca}+\mathbf{E}_{inc}\,|\,/\,|\,\mathbf{E}_{inc}\,|$

and the time average Poynting vector $\langle S \rangle = 1/2\,\mathrm{Re}\{\mathbf{E} \times \mathbf{H}^*\}$ are required. The evaluation of the electromagnetic fields **E** and **H** at one point (X, Y, Z) in the normalized space, as described in equations (5.3.1) and (5.3.2), requires an extensive preparation of the vector spherical harmonics $\mathbf{M}_{mn}$ and $\mathbf{N}_{mn}$ and many coordinate transformations.

The contribution of each sphere *j* needs to be considered separately. A first step is to transform the Cartesian coordinate set $(\Delta X^j, \Delta Y^j, \Delta Z^j)$ (distance between the point of evaluation and the center (X^j, Y^j, Z^j) of the contributing sphere *j*) into a spherical tuple (r^j, θ^j, ϕ^j). The vector spherical basis for each sphere, $\mathbf{M}_{mn}^{(L)}$ and $\mathbf{N}_{mn}^{(L)}$ (with *L* = 1, 3), is defined around the scalar generating function of vector harmonics [5.18, 5.19],

$$u_{mn}(r^j, \theta^j, \phi^j) = e^{im\phi^j}\; P_n^m(\cos\theta^j)\; z_n(kr^j) \tag{5.3.26}$$

where $P_n^m(\cos\theta)$ is the associated Legendre function of the first kind and $z_n(kr)$ is selected from the spherical Bessel or Hankel function of the first kind, j_n or $h_n^{(1)}$ respectively, depending on whether the evaluation point lies inside or outside the sphere (scattered or internal fields). Note that the generating function u_{mn} is a solution of the scalar Helmoltz equation in spherical coordinates,

$$(\nabla^2 + k^2)u = 0\,. \tag{5.3.27}$$

The vector $\mathbf{M}_{mn}$ and $\mathbf{N}_{mn,}$ expressed in spherical coordinate unit vectors are expanded as

$$\begin{aligned} \mathbf{M}_{mn} &= \nabla \times (r^j\, u_{mn}) \\ &= 0\;\hat{\mathbf{e}}_r^j + ie^{im\phi^j}\; z_n(kr^j)\,\pi_{mn}(\cos\theta^j)\,\hat{\mathbf{e}}_\theta^j + -e^{im\phi^j}\; z_n(kr^j)\,\tau_{mn}(\cos\theta^j)\,\hat{\mathbf{e}}_\phi^j \end{aligned} \tag{5.3.28}$$

$$\begin{aligned} \mathbf{N}_{mn} &= (1/k)\nabla \times \mathbf{M}_{mn} \\ &= e^{im\phi^j}\; n(n+1)\,\frac{1}{kr^j} z_n(kr^j)\; P_n^m(\cos\theta^j)\,\hat{\mathbf{e}}_r^j \\ &\quad + e^{im\phi^j}\;\frac{1}{kr^j}[z_n(kr^j) + r\; z_n^{'}(kr^j)]\,\tau_{mn}(\cos\theta^j)\,\hat{\mathbf{e}}_\theta^j \\ &\quad + ie^{im\phi^j}\;\frac{1}{kr^j}[z_n(kr^j) + r\; z_n^{'}(kr^j)]\,\pi_{mn}(\cos\theta^j)\,\hat{\mathbf{e}}_\phi^j \end{aligned} \tag{5.3.29}$$

with the functions π_{mn} and τ_{mn} defined around the associated Legendre function by [5.14],

$$\pi_{mn}(\cos\theta) = \frac{mP_n^m(\cos\theta)}{\sin\theta} \tag{5.3.30}$$

$$\tau_{mn}(\cos\theta) = \frac{dP_n^m(\cos\theta)}{d\theta}. \tag{5.3.31}$$

These two functions determine the radiation patterns and they can be computed recursively [5.14]. From the initial conditions defined below,

$$\begin{aligned} &\pi_{00} = 0, \quad \pi_{01} = 0, \quad \pi_{10} = 0, \quad \pi_{11} = 1 \\ &\tau_{00} = 0, \quad \tau_{01} = -(1-\cos^2\theta)^{1/2}, \quad \tau_{10} = 0, \quad \tau_{11} = \cos\theta \end{aligned} \tag{5.3.32}$$

$$\pi_{mn}(\pm 1) = \begin{cases} (\pm 1)^{n+1}\dfrac{1}{2} & m = -1 \\ (\pm 1)^{n+1}\dfrac{n(n+1)}{2} & m = 1 \\ 0 & otherwise \end{cases} \tag{5.3.33}$$

$$\tau_{mn}(\pm 1) = \begin{cases} -(\pm 1)^{n}\dfrac{1}{2} & m = -1 \\ (\pm 1)^{n}\dfrac{n(n+1)}{2} & m = 1 \\ 0 & otherwise \end{cases}. \tag{5.3.34}$$

The evaluation of π_{mn} is possible from

$$\pi_{mn}(\cos\theta) = \frac{(2n-1)}{(n-m)}\cos\theta\,\pi_{mn-1}(\cos\theta) - \frac{(n+m-1)}{(n-m)}\pi_{mn-2}(\cos\theta) \tag{5.3.35}$$

when incrementing in index *n*, or from

$$\pi_{mn}(\cos\theta) = \frac{2m\cos\theta}{(1-\cos^2\theta)^{1/2}}\pi_{m-1n}(\cos\theta) - \frac{m(n+m-1)(n-m+2)}{(m-2)}\pi_{m-2n}(\cos\theta) \tag{5.3.36}$$

when incrementing in index *m*. The function τ_{mn} uses the values calculated from π_{mn}, as

$$\tau_{mn}(\cos\theta) = \frac{n}{m}\cos\theta\,\pi_{mn}(\cos\theta) - \frac{n+m}{m}\pi_{mn-1}(\cos\theta) \tag{5.3.37}$$

For a given decomposition at maximum harmonic order *N*, at one evaluation point and for each sphere contribution, it is more efficient to precompute the values of π_{mn} and

τ_{mn} and store them in arrays using similar data structure as will be discussed in section 5.3.5 before using them in Eqs. (5.3.28) and (5.3.29). An example of polar plots of π_{mn} and τ_{mn} up to order N = 5 are included in Appendix D.

Finally, the vector spherical harmonic basis $\mathbf{M}_{mn}$ and $\mathbf{N}_{mn}$ needs to be converted to its equivalent in rectangular coordinates before performing the weighing and summation operations described in the decomposition of **E** and **H** by equations (5.3.1) and (5.3.2). The summation is carried in rectangular coordinates because the basis vectors relative to each sphere are spatially invariant in that coordinates, that is

$$\left\{\hat{\mathbf{e}}_x^j, \hat{\mathbf{e}}_y^j, \hat{\mathbf{e}}_z^j\right\} = \left\{\hat{\mathbf{e}}_x, \hat{\mathbf{e}}_y, \hat{\mathbf{e}}_z\right\}. \tag{5.3.38}$$

The coordinate transformation of $\mathbf{M}_{mn}$ and $\mathbf{N}_{mn}$ is therefore

$$\begin{aligned}\begin{bmatrix}\mathbf{M}_{mn} & \mathbf{N}_{mn}\end{bmatrix} &= \begin{bmatrix} M_{mn,r} & M_{mn,\theta} & M_{mn,\phi} \\ N_{mn,r} & N_{mn,\theta} & N_{mn,\phi}\end{bmatrix}\begin{pmatrix}\hat{\mathbf{e}}_r^j \\ \hat{\mathbf{e}}_\theta^j \\ \hat{\mathbf{e}}_\phi^j\end{pmatrix} \\ &= \begin{bmatrix} M_{mn,r} & M_{mn,\theta} & M_{mn,\phi} \\ N_{mn,r} & N_{mn,\theta} & N_{mn,\phi}\end{bmatrix}\frac{\partial(r^i,\theta^i,\phi^i)}{\partial(\Delta X^j,\Delta Y^i,\Delta Z^i)}\begin{pmatrix}\hat{\mathbf{e}}_x^j \\ \hat{\mathbf{e}}_y^j \\ \hat{\mathbf{e}}_z^j\end{pmatrix} \\ &= \begin{bmatrix} M_{mn,x} & M_{mn,y} & M_{mn,z} \\ N_{mn,x} & N_{mn,y} & N_{mn,z}\end{bmatrix}\begin{pmatrix}\hat{\mathbf{e}}_x \\ \hat{\mathbf{e}}_y \\ \hat{\mathbf{e}}_z\end{pmatrix}.\end{aligned} \tag{5.3.39}$$

The Jacobian matrix (or the directional cosines) [5.19] provides a conversion of basis via

$$\frac{\partial(r^i,\theta^i,\phi^i)}{\partial(\Delta X^j,\Delta Y^i,\Delta Z^i)} = \begin{bmatrix} \sin\theta^j\cos\phi^j & \sin\theta^j\sin\phi^j & \cos\theta^j \\ -\cos\theta^j\cos\phi^j & \cos\theta^j\sin\phi^j & -\sin\theta^j \\ -\sin\phi^j & \cos\phi^j & 0\end{bmatrix}. \tag{5.3.40}$$

5.3.5 Data Structures Employed

Correctly implementing the multiple-multipole method is also complicated by the prevalence of tensors (multidimensional arrays) of variable size (the associated Legendre polynomials contain variable number of terms as the spherical harmonics

order n increases). A set of representational rules using suitable and consistent data structures is therefore indispensable.

In a two-index variable such as a_{mn}, usually represented by a two-dimensional array, a given set of integers m and n corresponds to one single basis function containing Legendre polynomials, that is denoted herein by a single ket $|mn\rangle$ [5.19]. To reduce the complexity of accessing multidimensional arrays in a field decomposition using up to N order of harmonics (recall that the bounds of a given ket $|mn\rangle$ are $1 \le n \le N$ and $-n \le m \le n$), some linearization of array is performed. For instance, a two-dimensional variable of the form a_{mn} is stored in memory as an one-dimensional vector $a_{mn} \to a_{|mn\rangle}$,

$$a_r = [\quad a_{-11}\, a_{01}\, a_{11} \quad a_{-22}\, a_{-12}\, a_{02}\, a_{12}\, a_{22} \quad a_{-33} a_{-23}\, a_{-13}\, a_{-03}\, a_{13}\, a_{23}\, a_{33} \quad \ldots \quad] \qquad (5.3.41)$$

with a total length $N(N+2)$ and the tuple (m, n) is mapped to the single index r by $r = n(n+1) + m$. A four-index tensor such as the coefficients appearing in the addition theorem is stored in memory as matrix $A^{mn}_{\mu\nu} \to A^{|mn\rangle}_{|\mu\nu\rangle}$, with the expanded structure,

$$A^r_s = \begin{bmatrix} A^{-11}_{-11}\, A^{01}_{-11}\, A^{11}_{-11} & A^{-22}_{-11}\, A^{-12}_{-11}\, A^{02}_{-11}\, A^{12}_{-11}\, A^{22}_{-11} & \ldots \\ A^{-11}_{01}\, A^{01}_{01}\, A^{11}_{01} & A^{-22}_{01}\, A^{-12}_{01}\, A^{02}_{01}\, A^{12}_{01}\, A^{22}_{01} & \ldots \\ A^{-11}_{11}\, A^{01}_{11}\, A^{11}_{11} & A^{-22}_{11}\, A^{-12}_{11}\, A^{02}_{11}\, A^{12}_{11}\, A^{22}_{11} & \ldots \\ \\ A^{-11}_{-22}\, A^{01}_{-22}\, A^{11}_{-22} & A^{-22}_{-22}\, A^{-12}_{-22}\, A^{02}_{-22}\, A^{12}_{-22}\, A^{22}_{-22} & \ldots \\ A^{-11}_{-12}\, A^{01}_{-12}\, A^{11}_{-12} & A^{-22}_{-12}\, A^{-12}_{-12}\, A^{02}_{-12}\, A^{12}_{-12}\, A^{22}_{-12} & \ldots \\ A^{-11}_{02}\, A^{01}_{02}\, A^{11}_{02} & A^{-22}_{02}\, A^{-12}_{02}\, A^{02}_{02}\, A^{12}_{02}\, A^{22}_{02} & \ldots \\ A^{-11}_{12}\, A^{01}_{12}\, A^{11}_{12} & A^{-22}_{12}\, A^{-12}_{12}\, A^{02}_{12}\, A^{12}_{12}\, A^{22}_{12} & \ldots \\ A^{-11}_{22}\, A^{01}_{22}\, A^{11}_{22} & A^{-22}_{22}\, A^{-12}_{22}\, A^{02}_{22}\, A^{12}_{22}\, A^{22}_{22} & \ldots \\ \\ \ldots & \ldots & \ldots \end{bmatrix}. \qquad (5.3.42)$$

Extending the one-dimensional version, this matrix contains $N(N+2)$ by $N(N+2)$ scalar elements and access to the indices $(m, n; \mu, \nu)$ is via

$$\begin{aligned} r &= n(n+1) + m \\ s &= \nu(\nu+1) + \mu \,. \end{aligned} \qquad (5.3.43)$$

The number of non-trivial elements inside a generic fourth-order tensor $A_{\mu\nu}^{mn}$ can be further reduced by providing additional conditions on the indices. For instance, when $m = u$, the array $A_{m\nu}^{mn}$ has only non-trivial diagonals in each block identified by (n,ν). A second example is given by the rotation operator, denoted by $R_{\mu m}^{(n)}$, that contains non-zero elements only when $n = \nu$, thus making the represented matrix block diagonal.

In the formulation of the T-matrix in Eq. (5.3.6), an interleaved quantity like $\mathbf{a} = [a_{mn}\ b_{mn}]$, is represented using the following scheme, that is $[a_{|mn\rangle}\ b_{|mn\rangle}] \rightarrow a_s$ and

$$a_s = [\quad a_{-11}\, a_{01}\, a_{11}\quad b_{-11}\, b_{01}\, b_{11}\quad a_{-22}\, a_{-12}\, a_{02}\, a_{12}\, a_{22}\quad b_{-22}\, b_{-12}\, b_{02}\, b_{12}\, b_{22}\quad \ldots\quad] \tag{5.3.44}$$

with a doubled length as compared to equation (5.3.41). An element of indices (*m*, *n*) is located at the address *r* by

$$r = \begin{Bmatrix} (n+1)(2n-1)+m & for\ a_{mn} \\ n(2n+3)+m & for\ b_{mn} \end{Bmatrix}. \tag{5.3.45}$$

For a given harmonic (*m, n*), the subtraction between the addresses of an element at b_{mn} and at a_{mn} is $2n+1$, the size of block at a given *n* contains elements running from $-n \le m \le n$ (i.e. for *n* = 3, the index *m* runs from -3 to 3, thus containing 2(3) + 1 scalar terms). The above mentioned array indexing scheme is also followed for the two-dimensional analogue "T-matrix", which has the following structure

$$\mathbf{T} = \begin{bmatrix} A_{\mu\nu}^{mn} & B_{\mu\nu}^{mn} \\ C_{\mu\nu}^{mn} & D_{\mu\nu}^{mn} \end{bmatrix}. \tag{5.3.46}$$

5.3.6 Overall Program Flow

The program flow of the multiple-multipole method is displayed in Fig. 5.4 below. The whole procedure calculates the electromagnetic fields at a spatial point for one single sphere, given a certain configuration of spheres, specified at the beginning of a simulation. Iterations are needed to scan the spectrum or to calculate the points on a planar screen.

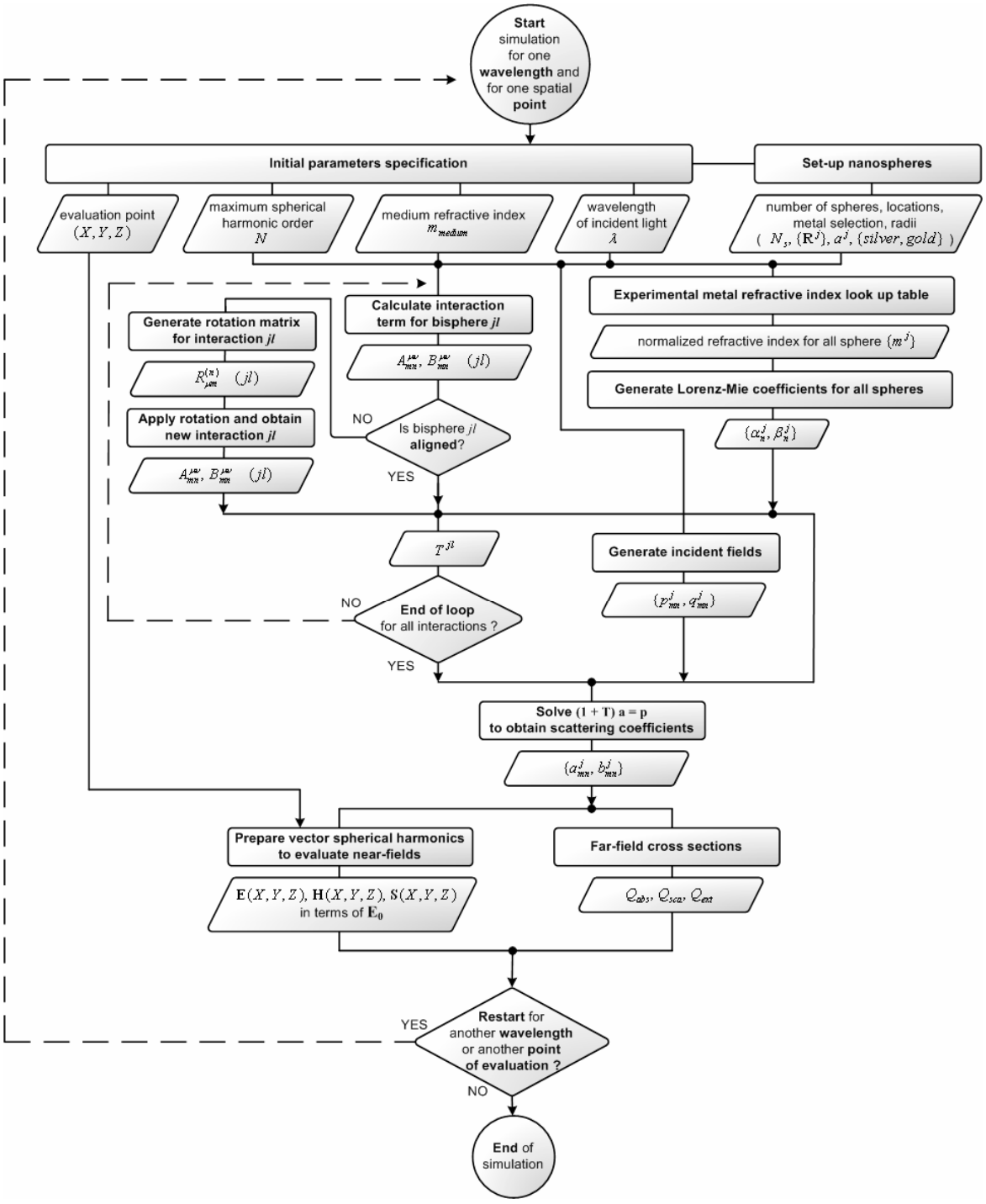

Figure 5.4 – Overall program flow.

5.4 Design of Efficient Metallic Nanoparticles for SERS

5.4.1 Geometries Setup and Convergence

The simulations were performed on systems of gold and silver nanoparticles assembled into various geometries and immersed in an aqueous medium (m_{medium} =1.3342). The dielectric properties of the silver and gold nanoparticles were assumed to be that of bulk material; measured bulk dielectric values reported by Johnson and Christy (Chapter 3) were used in all calculations and interpolated as needed. The problem setup is depicted in Fig. 5.3, where the incident field is propagating in the z-direction and polarized along the x-direction. The structures are always oriented in such a way that the maximum charge polarization, along x, is obtained. The seed structure in the center of our systems, where the "hot-spot" is located, consists of a bisphere whose spheres have 5nm radii and a separation of 0.5nm – close to the limit of what DNA based self-assembly might achieve [5.23]. Field enhancement is taken as the ratio of the local electric field at the "hot-spot", the center of the seed bisphere, to the electric field strength in the illuminating field.

While the multiple-multipole theory has been described in the exact case where all harmonic degrees and orders are included, practical computation truncates harmonic degree to $1 \le n \le N$. In our work, to achieve convergence in near field enhancement at the level of <5%, we have used $N = 10$. This corresponds to a total of $2N(N+1) = 220$ vector harmonic expansion components *per sphere*. An example of the convergence in field enhancement is given in Fig. 5.5. below. The structure employed is a self-similar series of 12 nanospheres with a geometric growth factor $\kappa = 0.831$ (see section 5.4.3 for definition). Both the cases of gold and silver particles are illustrated.

The contribution of high degree multipoles is obviously important for the accurate prediction of resonant wavelengths at which field enhancement is maximum, in agreement with Khlebtsov et al. findings [5.24] that the dipole approximation is inadequate. The physical reason is simple, electric fields confined to a characteristic size

d are decomposed into harmonics extending to up to degree $N \propto a / d$, with a particle radius a.

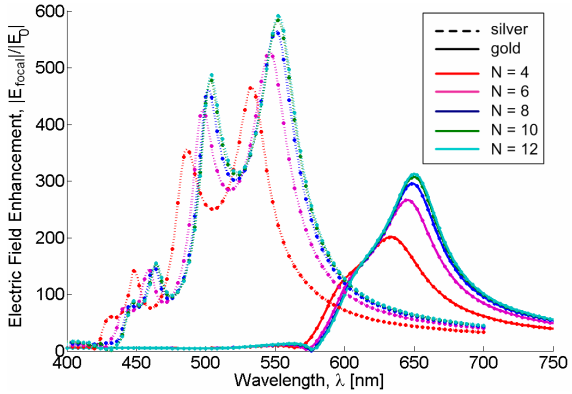

Figure 5.5 – An example showing the convergence of near-field enhancement at the focal point for varying maximum degree N of spherical harmonics included in the simulation.

5.4.2 Linear Chains

The linear chain geometry simulated here consists of identical gold or silver nanospheres with 5nm radius and interparticle gap of 0.5nm, shown in Fig. 5.6. Field enhancement is maximum at the middle gap. As the number of spheres N_s is increased from 2 to 20, the resonant wavelength is red-shifted and the quality factor of the field enhancement resonance increases, as shown in Figs. 5.7 and 5.8.

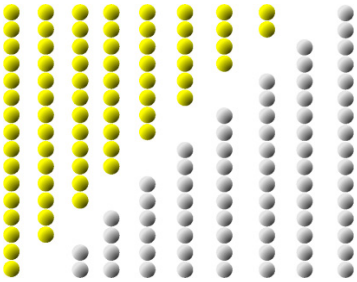

Figure 5.6 – Linear chain geometries of identical gold or silver nanospheres.

The field enhancement is calculated as the ratio of the electric field magnitude at the focal spot of the structure to the incident plan wave electric field magnitude. The linear particle chain functions as an optical antenna, similar to the continuous metal wire exhibiting a plasma resonance [5.25], but with an effective resonance determined by the

phase velocity of a plasma excitation propagating along a chain of particles. The field enhancement response of gold linear chains is suppressed at free space optical wavelengths shorter than 600nm, due to a reduction in gold dielectric quality factor, $Q = d(\omega\varepsilon')/d\omega \;/\; 2\varepsilon''$ where ε', ε'' are real and imaginary parts of the dielectric constant [5.26], resulting from the onset of interband absorption at 2eV [5.27]. The greater material quality factor of silver versus gold is further evidenced by the sharper resonances in field enhancement observed for the silver particle array.

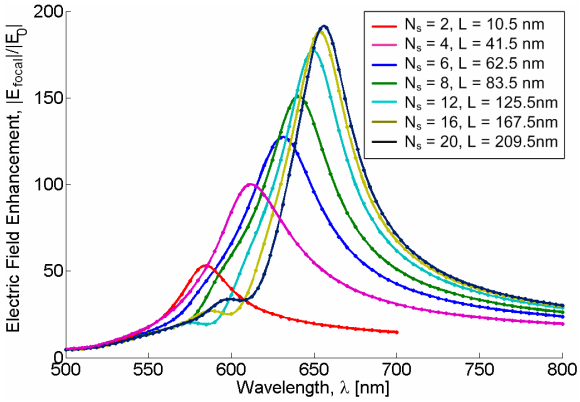

Figure 5.7 – Enhancement of near-field at focal point among linear chains with varying number of gold nanospheres.

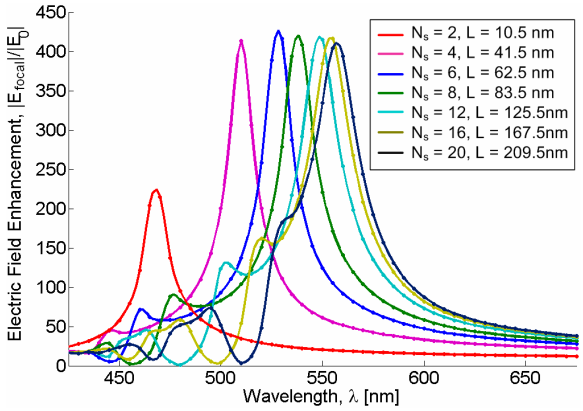

Figure 5.8 – Enhancement of near-field at focal point among linear chains with varying number of silver nanospheres.

5.4.3 Self-similar Structures with Constant Number of Spheres

The self-similar configuration of metal nanospheres first proposed by Li, Stockman and Bergman [5.28] and shown to be efficient at focusing optical near fields using quasi-static simulations. The self-similar structure is defined with a central bisphere with sphere radii a^0 (taken to be 5nm) and interparticle gap d^0 (taken to be 0.5nm). Successive spheres are added to the structure in geometric series with radii a^j and nearest neighbour gap d^j enlarged by a factor $1/\kappa$, such that $a^{j+1} = a^j / \kappa$ and $d^{j+1} = d^j / \kappa$. Note that in the limit where $\kappa = 1$, the linear chain is recovered. We compared the response of arrays with a fixed number of spheres N_s=4 and 6 and varying geometric factor κ and length L, illustrated to scale in Fig. 5.9 and 5.10. Since the complexity of self-assembly processes increases with number of particles per discrete unit, optimizing field enhancement for fixed particle number N_s is important.

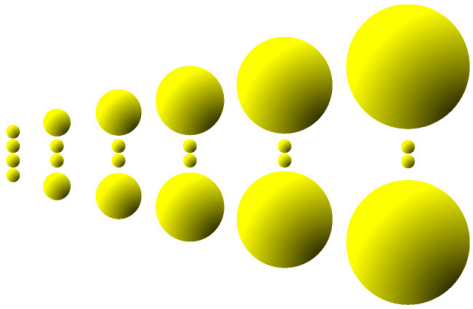

Figure 5.9 – A 4-sphere with varying geometric progression growth factors κ = 1, 0.5, 0.3, 0.2, 0.143 and 0.111.

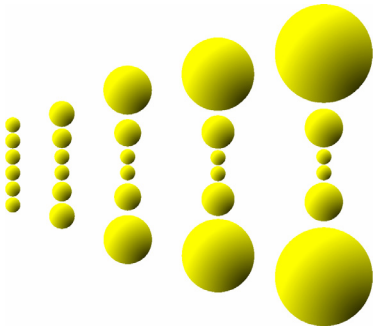

Figure 5.10 – A 6-sphere with varying geometric progression growth factors κ = 1, 0.768, 0.558, 0.456, and 0.393.

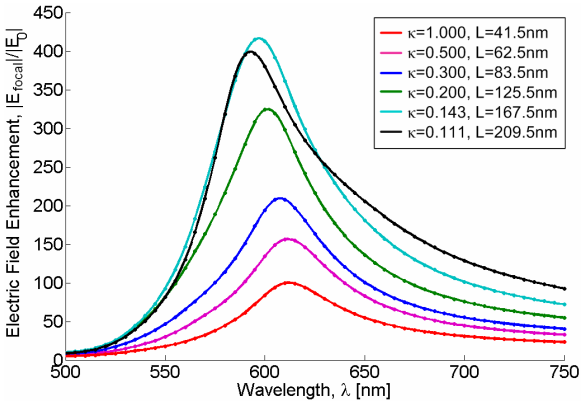

Figure 5.11 – Enhancement of near-field at focal point among various geometric progressions of 4 gold nanospheres as the geometric parameter κ is varied.

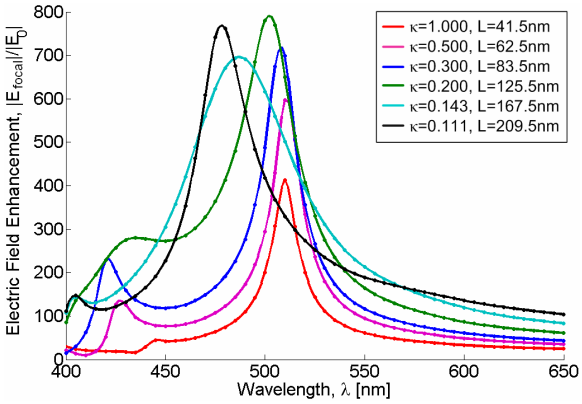

Figure 5.12 – Enhancement of near-field at focal point among various geometric progressions of 4 silver nanospheres. as the geometric parameter κ is varied.

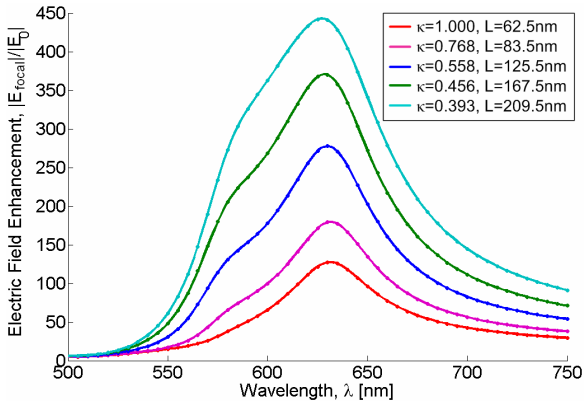

Figure 5.13 – Enhancement of near-field at focal point among various geometric progressions of 6 gold nanospheres as the geometric growth parameter κ is varied.

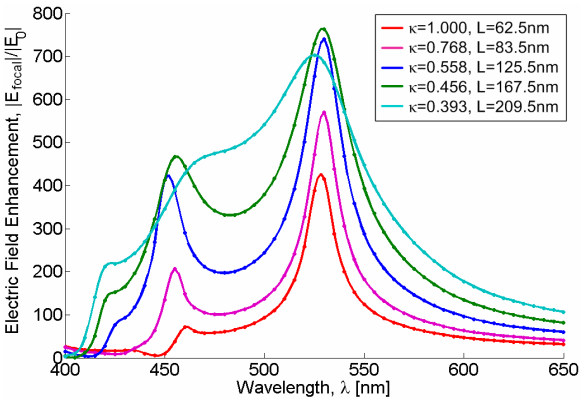

Figure 5.14 – Enhancement of near-field at focal point among various geometric progressions of 6 silver nanospheres as the geometric growth parameter κ is varied.

The simulated field enhancements for 4-sphere and 6-sphere structures composed of gold and silver particles are plotted in Figs. 5.11-5.14. The higher material Q of silver compared to gold is apparent in the widths of field enhancement resonances, and also in the clear presence of higher order resonances for silver structures but not gold. Interband absorption in gold above 2eV suppresses field enhancement at $\lambda < 600$nm. The improved efficiency of the geometric series of spheres over the linear chain is due to the increased metallic volume that expels a greater amount of optical energy, and the reduced number of gaps into which optical energy is focused. Importantly, these simulated field enhancement plots reveal that the geometric scale factor κ (which implicitly defines structure length for a fixed number of spheres N_s) that maximizes field enhancement is a non-trivial function of both sphere material and number of spheres. Full electromagnetic simulation without resorting to the quasi-static approximation is required to accurately model the resonances of the plasma wave excitation along a self-similar structure.

5.4.4 Self-similar Structures of Fixed Length

Simulation of structures of fixed length and varying growth factor κ and sphere number N_s, illustrated in Fig. 5.15, were also performed. The optimization of structures of fixed linear extent is important for *in-vivo* applications [5.29], where the retention or expulsion of particles is dependent on size. The electric field enhancement is plotted in Figs. 5.16-5.19 for self-similar structures with length 167.5nm (209.5nm), the length of linear chains of 16 (20) spheres of 5nm radius and 0.5nm interparticle gap.

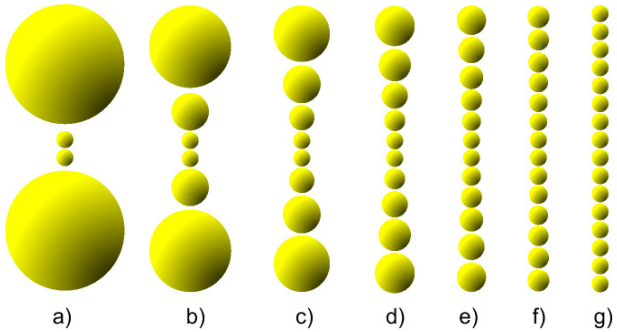

Figure 5.15 – Geometric progression of nanospheres in self-similar structures whose total lengths are fixed to that of a 16-sphere linear chain (167.5nm).

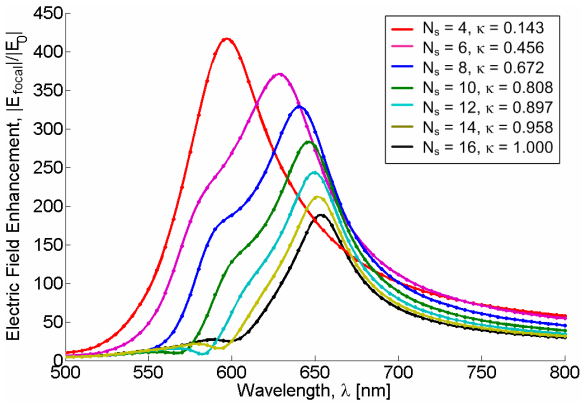

Figure 5.16 – Focal point electric field-enhancement for gold self-similar structures equal in length to a 16-sphere linear chain (167.5nm).

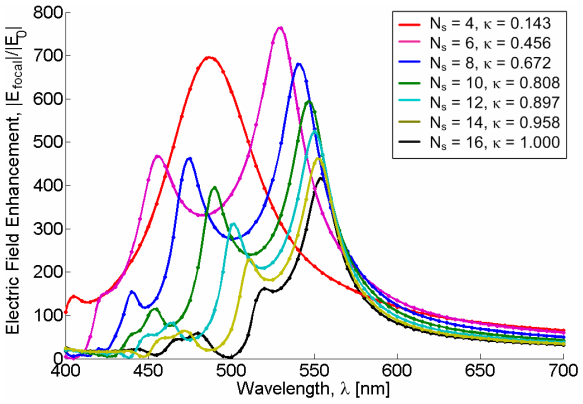

Figure 5.17 – Focal point electric field-enhancement for silver self-similar structures equal in length to a 16-sphere linear chain (167.5nm).

The field enhancement resonances are red-shifted as the structures approach linear chains (geometric factor $\kappa \to 1$). The red-shift can be interpreted as arising from the increase in hybridization of the plasma resonances associated with individual spheres, and hence a reduction in frequency of the lowest order plasma oscillation distributed over the structure [5.30]. The linear chain does not provide the same field enhancement as self-similar structures with $\kappa < 1$. The precise value of κ (which implicitly defines number of spheres N_s for a fixed length structure) that maximizes field enhancement depends upon both sphere material and physical length of the structure, but the general trend is improved efficiency with smaller κ (fewer spheres N_s).

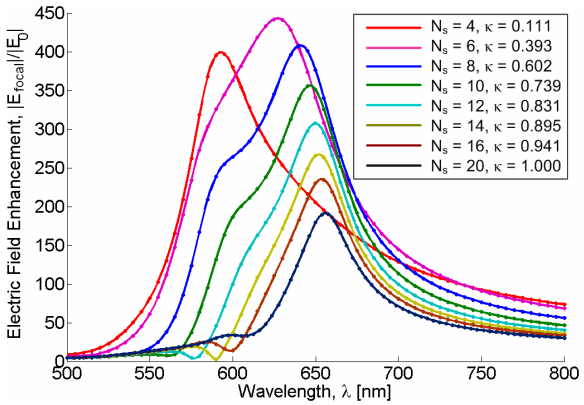

Figure 5.18 – Focal point electric field-enhancement for gold self-similar structures equal in length to a 20-sphere linear chain (209.5nm).

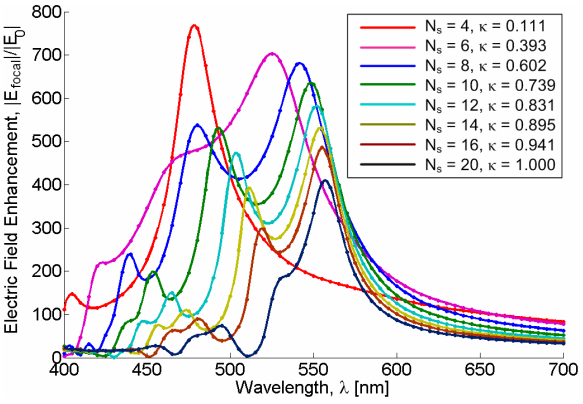

Figure 5.19 – Focal point electric field-enhancement for silver self-similar structures equal in length to a 20-sphere linear chain (209.5nm).

5.4.5 Near-field Distributions in Self-similar Structures

The spatial distribution of electric field enhancement $| \mathbf{E}_{sca} + \mathbf{E}_{inc} | / | \mathbf{E}_{inc} |$ in the vicinity of the self-similar structures is useful in explaining the role of structure in near-field enhancement and the importance of vector multipole calculation. Field enhancements in the x-z and x-y planes (the x-z plane is the plane of incidence) for self-similar gold structures of 167.5nm length are presented on a logarithmic scale in Figs. 5.20, 5.21. The internal field of each sphere is not shown. Each field enhancement plot is taken with incident light at the wavelength that maximizes field enhancement at the focal spot of the structure, summarized in Table 5.1. These plots reveal the "hot-spots" associated with each structure, with those structures that approach the linear chain having a preponderance of "hot-spots". Structures with small κ are dominated by the large volume spheres, which serve to enhance field in a reduced number of "hot-spots". The higher dielectric quality factor Q of silver versus gold is evident in the increased field enhancement about the silver structures.

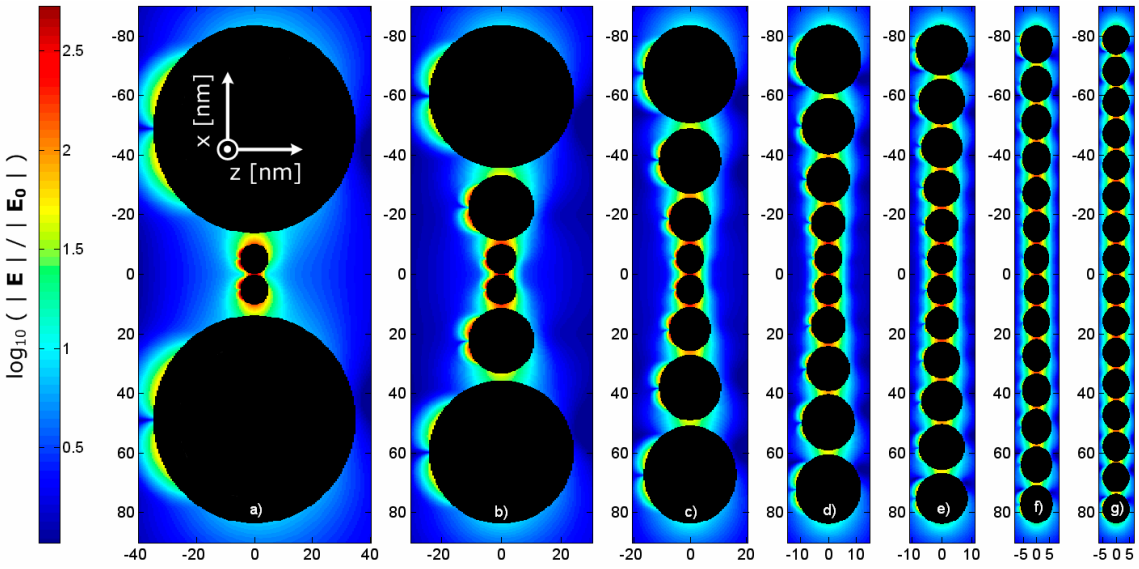

Figure 5.20 – The electric field enhancement in the xz-plane for self-similar gold assemblies of length 167.5nm.

The near-field plots also reveal the importance of multiple-multipole calculations. The incident side of the nanospheres show field enhancement associated with the charge polarization induced by the incident electric field. Although this induced charge

distribution is dipolar in nature, the field distribution about spheres is clearly not dipolar due to the strong coupling amongst them. Furthermore, there is a clear distinction in Fig. 5.20 between the incident side and the shadow side of the nanospheres, a direct manifestation of the retardation of fields. The near-fields of Fig. 5.20 indicate clearly that as the condition for the quasi-static approximation, $x << 2\pi m_{medium}\, a\, /\, \lambda$, is better satisfied, by smaller spheres (in the linear chains), field retardation is reduced and the distinction between incident side near-field and shadow side near-field is diminished.

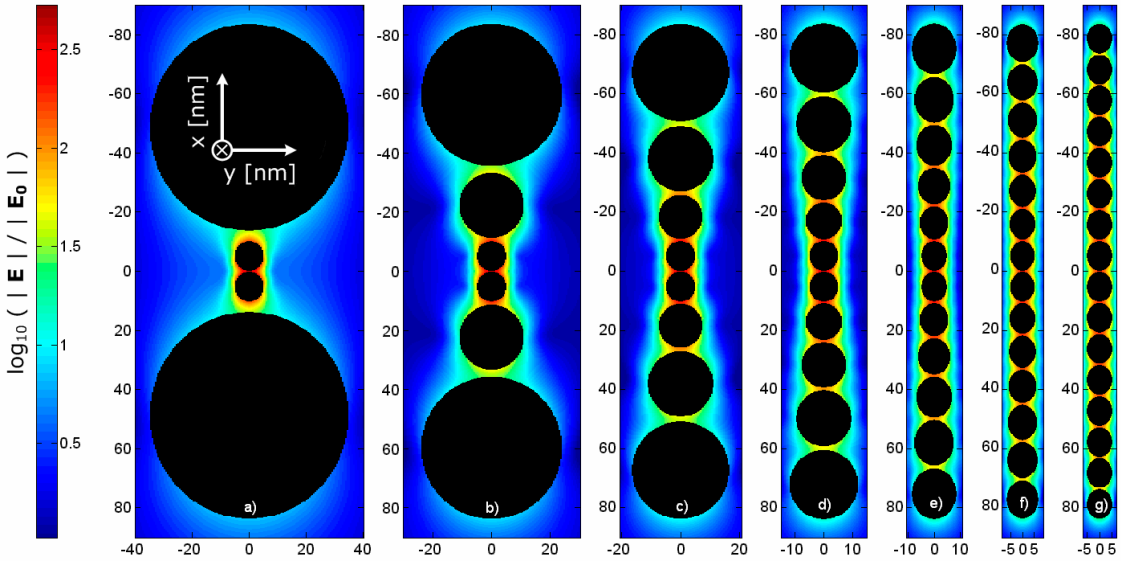

Figure 5.21 – The electric field enhancement in the xy-plane for self-similar gold assemblies of length 167.5nm.

		(a)	(b)	(c)	(d)	(e)	(f)	(g)
N_s		4	6	8	10	12	14	16
κ		0.143	0.456	0.672	0.808	0.897	0.958	1.000
near-field peak λ [nm]	gold	597	628	640	647	650	652	654
	silver	487	530	542	547	550	552	553
absorption peak λ [nm]	gold	598	627	638	645	648	650	652
	silver	487	530	542	547	550	552	553
scattering peak λ [nm]	gold	612	637	645	648	652	653	653
	silver	513	533	543	548	552	553	555

Table 5.1 – Summary of resonance peaks for self-similar structures of length 167.5nm taken from data plotted in Figs. 5.16, 5.17, 5.24, 5.25. Near-field distributions are plotted at near-field enhancement peaks.

The retardation of fields is also seen in the time average Poynting vector $\langle S \rangle = 1/2\,\mathrm{Re}\{\mathbf{E}\times\mathbf{H}^*\}$. The Poynting vector magnitude is plotted in Fig. 5.22 for self similar gold structures of 167.5 nm length. Energy is clearly drawn into the structures on the incident side, casting shadow regions for spheres as small as 5nm in radius. It should be noted that although isolated spheres may be well modeled under the quasi-static approximation, the complete structure need not be well modeled using a quasi-static approximation. Shadows in the Poynting vector are indeed visible for each structure in Fig. 5.22.

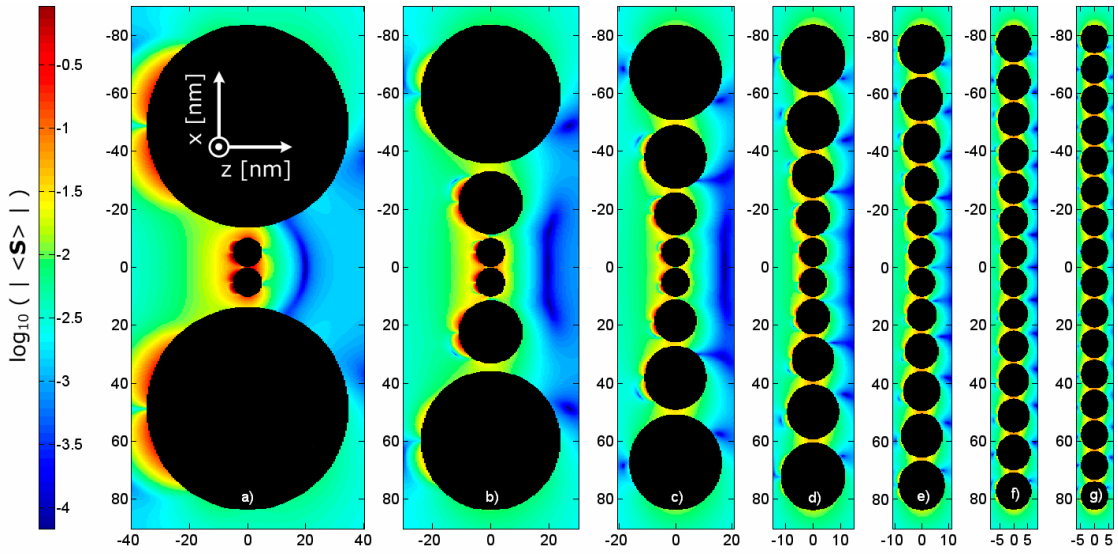

Figure 5.22 – The time-average Poynting vector magnitude in the xz-plane for self-similar gold assemblies of length 167.5nm. The reference incident power is situated at -2.58 = log $(1/\eta)$.

The higher order resonances of self-similar structures are complex in nature. The spatial distribution of near-field enhancement in the incident plane for a silver N_s=8, κ=0.672 self-similar structure is plotted in Fig. 5.22 for the three lowest order resonances in near-field enhancement (taken from Fig. 5.19). The three near-field resonances appear to be distinguished by different hybridizations of dipolar plasma excitations on the individual spheres. The geometric series structure does not lend itself to a simple quantitative description of resonances expected for a linear chain.

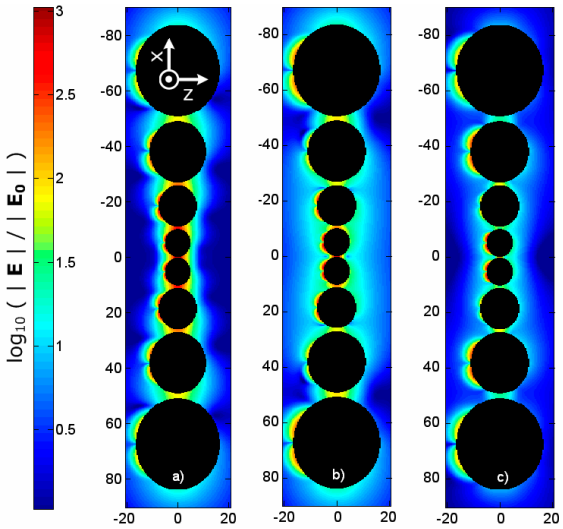

Figure 5.23 – Electric field enhancement in the xz-plane for the silver N_s=8-self-similar structure at three different wavelengths. (a) 542nm, (b) 474nm, (c) 440nm.

5.4.6 Far-field Properties of Self-similar Structures

The far-field scattering efficiency Q_{sca} of single spheres in the Rayleigh limit can be measured using linear dark-field microscopy techniques [5.31] and provide indirect information about field enhancement properties [5.32]. Near-field enhancement and far-field scattering are not simply related in more general metal nanostructures such as nanosphere assemblies. Both the absorption efficiency Q_{abs} and far-field scattering efficiency are plotted in Figs. 5.24-5.27 for self-similar structures with a length of 167.5nm.

The absorption efficiency and near-field enhancement are resonant at approximately equal wavelengths (refer to Table 5.1). The co-location of resonances is in agreement with studies of small individual spheres [5.32]. We also note that linear structures have N_s-1 gaps where field enhancement is comparable to that at the central focus (Figs. 5.20, 5.21), resulting in significantly increased absorption at the near-field enhancement resonance in comparison to structures with $\kappa < 1$. Strong interband absorption at wavelengths $\lambda < 600$nm is evident for gold particle assemblies with small κ, where absorption is expected to be dominated by the largest spheres.

The resonances in scattering efficiency of self-similar structures in the linear chain limit $\kappa \to 1$ closely follow the resonances in field enhancement and absorption

efficiency. However, in the limit of small geometric factor κ, the scattering efficiency peaks acquire a significant red-shift with respect to the near-field enhancement. The physical origin of this red-shift is unknown, but has been observed in numerical studies of single sphere scattering [5.32]. The red-shift was found in [5.32] to increase with sphere size, in agreement with our finding of increased red-shift with decreasing κ (and hence larger spheres in the structure). Elastic light scattering data, such as that collected with dark-field microscopy, will therefore need to be carefully interpreted when inferring near-field enhancement properties of self-similar structures with geometric factor $\kappa << 1$.

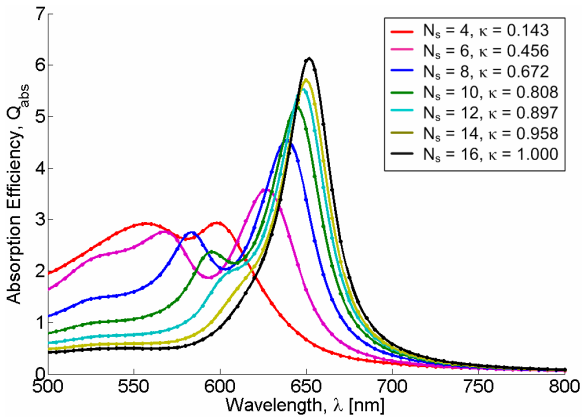

Figure 5.24 – Absorption efficiency among various geometric progressions of gold nanospheres whose lengths are fixed to that of a 16-sphere linear chain.

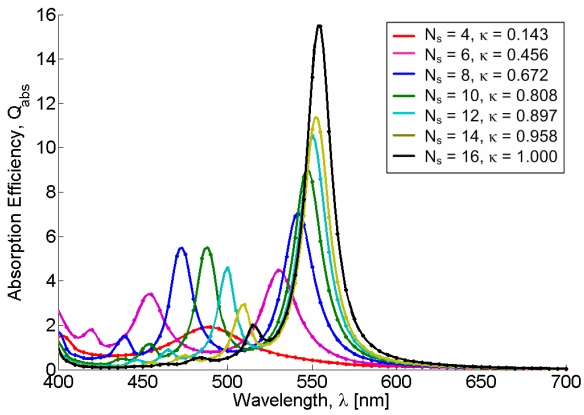

Figure 5.25 – Absorption efficiency among various geometric progressions of silver nanospheres whose lengths are fixed to that of a 16-sphere linear chain.

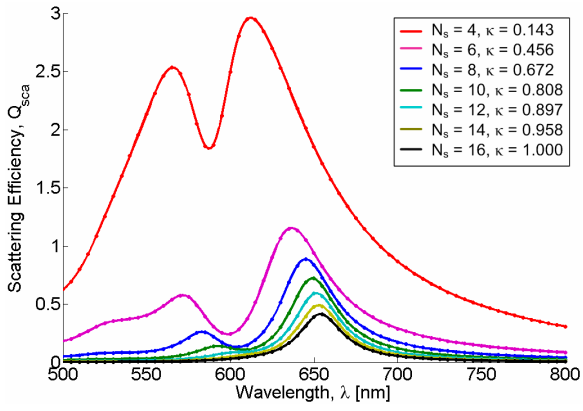

Figure 5.26 – Scattering efficiency among various geometric progressions of gold nanospheres whose lengths are fixed to that of a 16-sphere linear chain.

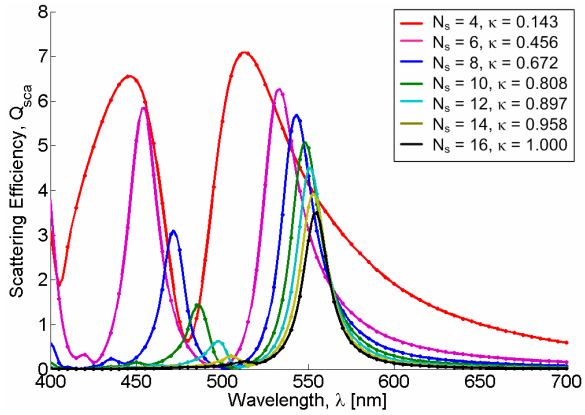

Figure 5.27 – Scattering efficiency among various geometric progressions of silver nanospheres whose lengths are fixed to that of a 16-sphere linear chain.

5.4.7 Other Geometries

Three other geometries were investigated, as illustrated in Fig. 5.28: the discrete nanosphere approximations of a cone, pyramid and triangular truss. The near-field enhancement versus wavelength for structures composed of 5nm radius gold nanoparticles with 0.5nm minimum interparticle gaps are illustrated in Fig. 5.29. As in the case of linear chains, the field is distributed amongst the interparticle gaps whose preponderance results in field enhancement inferior to the self-similar structure.

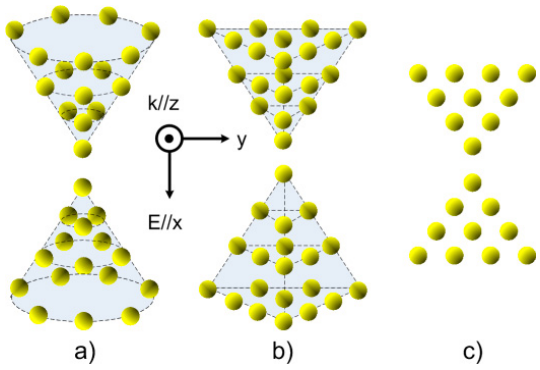

Figure 5.28 – Discrete approximation of (a) cone, (b) pyramid and (c) triangular truss.

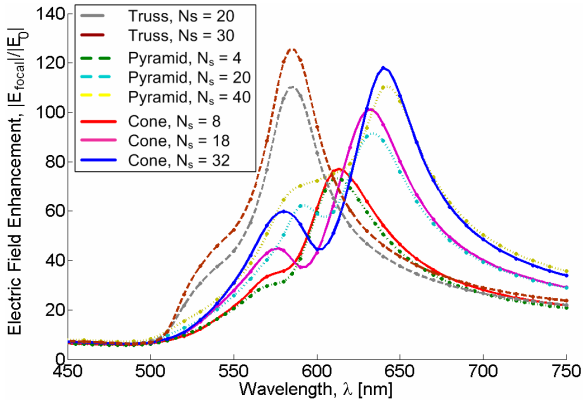

Figure 5.29 – Enhancement of near-field at focal point among the cone, pyramid and truss geometries.

5.6 References

[5.1] P.N. Prasad, *Nanophotonics* (Wiley-Interscience, New Jersey, 2004).

[5.2] J.R. Lakowicz, "Plasmonics in Biology and Plasmon-Controlled Fluorscence," *Plasmonics*, vol. 1, pp. 5-33, 2006.

[5.3] D.P. Craig, T. Thirunamachandran, *Molecular Quantum Electrodynamics* (Dover Publications, 1998).

[5.4] G.C. Schatz, M.A. Ratner, *Quantum Mechanics in Chemistry* (Dover Publications, New York, 2002).

[5.5] P. Atkins, J. de Paula, Physical Chemistry for Life Sciences (Oxford University Press, New York, 2006).

[5.6] P.N. Prasad, *Biophotonics* (Wiley-Interscience, New Jersey, 2003).

[5.7] K. Kneipp, H. Kneipp, I. Itzkan, R.R. Dasari, M.S. Feld, "Ultrasensitive Chemical Analysis by Raman Spectroscopy," *Chem. Rev.*, vol. 99, pp. 2957-2975, 1999.

[5.8] K. Kneipp, M. Moskovits and H. Kneipp, *Surface-Enhanced Raman Scattering: Physics and Applications* (Springer, Berlin, 2006).

[5.9] S.A. Maier, *Plasmonics – Fundamentals and Applications* (Springer, Bath, 2007).

[5.10] L. Novotny and B.Hecht, *Principles of Nano-Optics* (University Press, Cambridge, 2006).

[5.11] T.A. Klar, "Biosensing with plasmonic nanoparticles," in *Nanophotonics with Surface Plasmons*, V.M. Shalaev, and S. Kawata, ed. (Elsevier, 2007), pp. 219-270.

[5.12] Y.W.C. Cao, R. Jin, C.A. Mirkin, "Nanoparticles with Raman Spectroscopic Fingerprints for DNA and RNA Detection," *Science*, vol. 297, pp. 1536-1540, 2002.

[5.13] T. Vo-Dynh, D.L. Stokes, G.D. Griffin, M. Volkan, U.J. Kim, and M.I. Simon, "Surface-enhanced Raman Scattering (SERS) Method and Instrumentation for Genomics and Biomedical Analysis," *J. Raman Spectrosc.*, vol. 30, pp. 785-793, 1999.

[5.14] Y. Xu, "Electromagnetic scattering by an aggregate of spheres," *Appl. Opt.*, vol. 34, pp. 4573-4588, 1995.

[5.15] D. W. Mackowski, "Analysis of radiative scattering for multiple sphere configurations," *Proc. R. Soc. London Ser. A*, vol. 433, pp. 599-614, 1991.

[5.16] J. H. Bruning and Y. T. Lo, "Multiple Scattering of EM Waves by Spheres Part I – Multipole Expansion and Ray-Optical Solutions," *IEEE Tran. Antennas Propag.*, vol. AP-19, pp. 378-390, 1971.

[5.17] H.C. van de Hulst, *Light Scattering by Small Particles* (Dover, New York, 1981).

[5.18] C.F. Bohren and D.R. Huffman, *Absorption and Scattering of Light by Small Particles* (Wiley, New York, 1983).

[5.19] G. Arfken and H. J. Weber, *Mathematical Methods for Physicists*, 6th. ed. (Academic, Orlando, 2005).

[5.20] Y. Xu, "Calculation of the Addition Coefficients in Electromagnetic Multisphere-Scattering Theory," *J. Comput. Phys.*, vol. 127, pp. 285-298, 1996.

[5.21] D. W. Mackowski, "Calculation of total cross sections of multiple-sphere clusters," *J. Opt. Soc. Am. A*, vol. 11, pp. 2851-2861, 1994.

[5.22] A. R. Edmond, *Angular Momentum in Quantum Mechanics* (Princeton University Press, Princeton, 1957).

[5.23] F.A. Aldaye, H.F. Sleiman, "Dynamic DNA Templates for Discrete Gold Nanoparticle Assemblies: Control of Geometry, Modularity, Write/Erase and Structural Switching," *J. Am. Chem. Soc.*, vol. 129, pp. 4130-4131, 2007.

[5.24] B. Khlebtsov, A. Melnikov, V. Zharov, and N. Khlebtsov, "Absorption and scattering of light by a dimer of metal nanospheres: comparison of dipole and multipole approaches," *Nanotechnology*, vol. 17, pp. 1437-1445, 2006.

[5.25] L. Novotny, "Effective Wavelength Scaling for Optical Antennas," *Phys. Rev. Lett.*, vol. 98, pp. 266802, 2007.

[5.26] F. Wang, and Y. Ron Shen, "General Properties of Local Plasmons in Metal Nanostructures," *Phys. Rev. Lett.*, vol. 97, pp. 206806, 2006.

[5.27] P.B. Johnson and R.W. Christy, "Optical constants of the noble metals," *Phys. Rev. B*, vol. 6, pp. 4370-4379, 1972.

[5.28] K. Li., M.I. Stockman, and D.J. Bergman, "Self-similar chain of metal nanospheres as an efficient nanolens," *Phys. Rev. Lett.*, vol. 91, pp. 227402, 2003.

[5.29] I. H. El-Sayed, X. Huang and M. A. El-Sayed, "Selective laser photo-thermal therapy of epithelial carcinoma using anti-EGFR antibody conjugated gold nanoparticles," *Cancer Lett.*, vol. 239, pp. 129-135, 2006.

[5.30] E. Prodan, C. Radloff, N. J. Halas and P. Nordlander, "A Hybridization Model for the Plasmon Response of Complex Nanostructures," *Science*, vol. 302, pp. 419 – 422, 2003.

[5.31] C. Sönnichsen, T. Franzl, T. Wilk, G. von Plessen, and J. Feldmann, "Drastic Reduction of Plasmon Damping in Gold Nanorods," *Phys. Rev. Lett.*, vol. 88, pp. 077402, 2002.

[5.32] B. J. Messinger, K. U. von Raben, R. K. Chang and P. W. Barber, "Local fields at the surface of noble-metal microspheres," *Phys. Rev. B*, vol. 24, pp. 649-657, 1981.

Chapter 6 – Conclusion

In this thesis, we explored two sensing modalities that exploit surface plasmons - the localized subwavelength electromagnetic fields that occur on metallic-dielectric interfaces. On planar surface geometries, the surface plasmon resonance (SPR) sensors are widely used as local index-of-refraction sensors for studying biomolecular interactions. In this respect, optical systems monitor the resonance condition to report the presence of molecules. Alternatively, surface plasmons that are confined on the surfaces of metallic subwavelength particles – in this thesis, assemblies of nanospheres – are also used to enhance evanescent near-fields. The enhancement of these nanometer fields is used to produce non-linear effects such as surface-enhanced Raman scattering (SERS), which has also shown great promise for molecular detection.

Two SPR sensors were reported: the integrated sensor and the 2D combined wavelength-angular modulated one. The work in this part involved the construction of the 2D sensor and the testing of both devices using NaCl solutions. The linear dependence of the angular shift in the plasmon dip with respect to NaCl molarity, observed in both systems, was used to estimate the angular sensitivity of the sensors. In fact, the integrated sensor and the 2D sensor (when the dip is tracked only for a specific wavelength) were estimated to have an angular sensitivity of ~ 126°/RIU and ~ 91°/RIU, respectively. Furthermore, a multiple-multipole method was implemented in order to characterize the near-field enhancement properties of discrete assemblies of metal nanospheres. Among the nanostructures considered, we found that the self-similar geometric series of spheres, first proposed by Li, Stockman and Bergman were significantly more efficient than linear chains or other discrete approximation of cone, pyramid or triangular struss. Through electromagnetics simulations, we showed that optical frequency electric fields can be enhanced in gold nanoparticle assemblies by an order of ~450 in nanometer volumes. This is within a factor of 2 of field enhancements achievable in nanostructures composed of lower resistance silver.

In the future, many further experimental works can be conducted along the line of this thesis. For example, in SPR sensing, the sensors are now ready to be tested with biological solutions. The shifts of plasmon dip sampled with respect to time, which are characteristics of biomolecular bindings, can be measured to detect, for example, biomarkers of Sepsis. The flat metallic surface in the 2D SPR sensor is also ready to be replaced with a properly designed grating to observe the opening of a bandgap in the surface plasmon dispersion curve. This surface plasmon bandgap is anticipated to increase sensitivity. On the other hand, for the surface plasmons localized on small spheres, there is hope that recent advances in DNA based self-assembly techniques for fabrication of discrete metal nanoparticle structures will lead to the physical realization of some of the efficient near-field focusing structures analyzed herein. Thereafter, a series of experiments can be conducted to demonstrate the control of optical near-fields with DNA-gold nanoparticle self-assemblies prepared by the Sleiman's group. For example, dark-field microscopy can be used to perform far-field measurements of Rayleigh scattering. We can also consider Raman scattering measurements on Raman active molecules bonded to an efficient, realizable nanoparticle assembly.

Appendix A – The Importance of Near-fields

A.1 Introduction

Using simple arguments from Fourier analysis, we shall introduce the angular spectrum representation of optical fields [A.1-A.3]. In this framework, the fields can be thought as a superposition of plane waves and evanescent waves. This picture for describing optical fields in the reciprocal space provides meaningful insights for understanding the significant role played by the evanescent near-fields in nano-optics and justifies the motivation for numerous apparatus designed to operate on sub-wavelength optical manipulation.

A.2 Superposing Evanescent and Planar Waves

Consider a generic type of problem where an incident electric field $\mathbf{E}_{inc}(x,y,z)$ illuminates an object and causes light to scatter, resulting in a scattered field $\mathbf{E}_{sca}(x,y,z)$. We are interested in the total field, $\mathbf{E} = \mathbf{E}_{inc} + \mathbf{E}_{sca}$, projected on a screen located at some position z, as illustrated in Fig. 3.1.

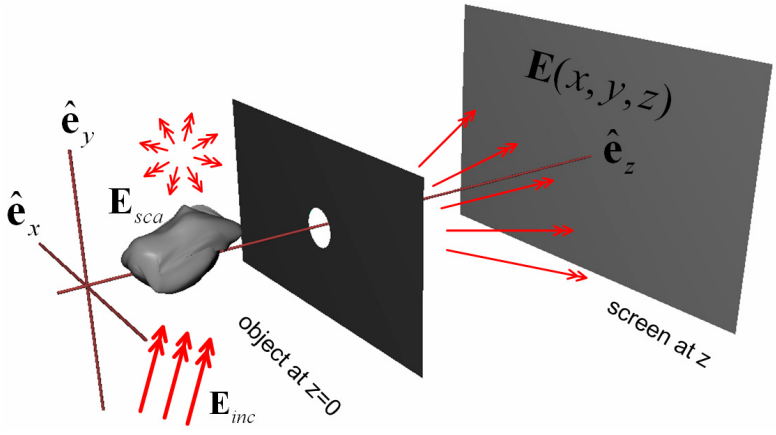

Figure A.1 – Generic optical problem.

We will first assume a time-harmonic optical field inside a homogeneous, isotropic, linear and source-free medium, using the familiar $\mathbf{E}(x,y,z,t) = \mathrm{Re}\{\mathbf{E}(x,y,z)e^{-i\omega t}\}$, satisfying the vector Helmoltz equation,

$$(\nabla^2 + k^2)\,\mathbf{E}(x,y,z) = 0\,. \tag{A.1}$$

The Fourier transform pairs of the optical field $\mathbf{E}(x,y,z)$ at the planar screen are given by [A.4, A.5]

$$\mathbf{E}(x,y,z) = \int\int_{-\infty}^{+\infty} \hat{\mathbf{E}}(k_x,k_y;z)\,e^{i[k_x x + k_y y]}dk_x\,dk_y \tag{A.2a}$$

$$\hat{\mathbf{E}}(k_x,k_y;z) = \frac{1}{4\pi^2}\int\int_{-\infty}^{+\infty} \mathbf{E}(x,y,z)\,e^{-i[k_x x + k_y y]}dx\,dy \tag{A.2b}$$

where the sets (x,y,z) and $(k_x,k_y;z)$ denote respectively the two-dimensional Cartesian coordinates and reciprocal space (or spatial frequencies) at the screen position *z*. By comparing (A.1) and (A.2), it is straightforward to arrive to the following ordinary second-order differential equation of the spectrum $\hat{\mathbf{E}}(k_x,k_y;z)$,

$$\left(\frac{d^2}{dz^2} + (k^2 - {k_x}^2 - {k_y}^2)\right)\hat{\mathbf{E}}(k_x,k_y;z) = 0\,. \tag{A.3}$$

A simple solution to (A.3) is in the form of

$$\hat{\mathbf{E}}(k_x,k_y;z) = \hat{\mathbf{E}}(k_x,k_y;0)\,e^{\pm ik_z z} \tag{A.4}$$

where the wavenumber k_z along the propagation direction *z* is defined as $k_z = (k^2 - {k_x}^2 - {k_y}^2)^{1/2}$, and the exponential factor is known as the *propagator* in reciprocal space or the *optical transfer function* (OTF) in free-space [A.5, A.6, A.3]. This factor, inside the Fourier transform integral, serves to evolve the optical field spectrum $\hat{\mathbf{E}}(k_x,k_y;0)$ from the origin (*z = 0*) up to the point *z* on the screen. The ± sign in front of the wavenumber component in z-axis indicates that forward and backward propagating waves (depending on the polarity of *z*) are to be considered.

Following the above formalism, the general electromagnetic fields are rewritten using the angular spectrum representation as

$$\mathbf{E}(x,y,z) = \int\int_{-\infty}^{+\infty} \hat{\mathbf{E}}(k_x,k_y;0)\, e^{i[k_x x + k_y y \pm k_z z]} dk_x\, dk_y \tag{A.5}$$

$$\mathbf{H}(x,y,z) = \int\int_{-\infty}^{+\infty} \hat{\mathbf{H}}(k_x,k_y;0)\, e^{i[k_x x + k_y y \pm k_z z]} dk_x\, dk_y . \tag{A.6}$$

By examining the sign of the radicand in k_z, we quickly realize that the exponential factor represents two kinds of waves (to simplify the discussion, let us consider for now only a lossless medium with a purely real refractive index m, so the wavenumber can be safely narrowed to being either a purely imaginary or a purely real quantity). If the components of the wavenumbers lying on the object plane are fairly small, that is, $k^2 \geq k_x^{\,2} + k_y^{\,2}$, then the wavenumber k_z is purely real and the exponential factor $e^{\pm i|k_z|z}$ represents an oscillatory term that accounts for propagation. On the other hand, if $k^2 < k_x^{\,2} + k_y^{\,2}$, then the wavenumber k_z turns into an imaginary number and the factor $e^{-|k_z||z|}$ is a fast exponentially decaying function. The above two terms are referred to respectively as *plane waves* and *evanescent waves*. As a result, the angular spectrum representation revealed in the expressions (A.5) and (A.6) suggests that optical fields are formed by a superposition of these two types of basis functions, weighted by their optical spectrum.

A.3 Field Propagation as a Filtering Process

The angular spectrum representation allows us to picture the evolution of the optical fields in free-space using a linear response approach [A.4, A.5]. From the two-dimensional spatial Fourier transform pairs introduced in section A.2, the optical field at the screen located at z can be imagined as the result of filtering the field at the origin ($z = 0$), that is [A.1] ,

$$\begin{aligned}\mathbf{E}(x,y,z) &= \int\int_{-\infty}^{+\infty} \hat{\mathbf{E}}(k_x,k_y;0)\, e^{i[k_x x + k_y y \pm k_z z]} dk_x\, dk_y \\ &= \frac{1}{4\pi^2} \int\int_{-\infty}^{+\infty} \int\int_{-\infty}^{+\infty} \mathbf{E}(x',y',0)\, e^{+i[k_x x + k_y y \pm k_z z]} e^{-i[k_x x' + k_y y']} dx'\, dy'\, dk_x\, dk_y \\ &= \mathbf{E}(x,y,0) * H(x,y,z)\end{aligned} \tag{A.7}$$

The convolution operation between the input field $\mathbf{E}(x,y,0)$ and the impulse response $H(x,y,z)$, characteristic of the propagation medium, is performed in the spatial domain.

The filter, described by the following pairs,

$$\hat{H}(k_x, k_y; z) = e^{\pm i k_z z} \tag{A.8}$$

$$H(x, y, z) = \int\int_{-\infty}^{+\infty} e^{+i[k_x x + k_y y \pm k_z z]}\, dk_x\, dk_y \tag{A.9}$$

modifies the spatial frequencies components of the input field $\mathbf{E}(x, y, 0)$. The input and output diagram and the physical situation are illustrated in Fig. A.2 below.

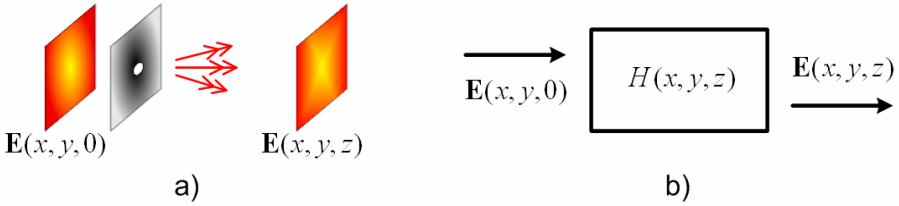

Figure A.2 – Spatial filtering process: (a) physical situation (b) linear system representation.

If the screen is located very far away from the object under illumination such as in many traditional optical imaging systems, the contribution from the exponentially decaying evanescent fields is practically none. As a consequence, only the far-field with transverse wavenumber $k_z = (k^2 - k_x^2 - k_y^2)^{1/2}$ where $k^2 \geq k_x^2 + k_y^2$ and $k = n\omega / c$ will be imaged onto the screen at coordinate z. In the language of linear response theory, we thus say that the original field $\mathbf{E}(x, y, 0)$ has been *low pass filtered* since the high spatial frequencies components carried by the evanescent fields have been suppressed. A three-dimensional reciprocal space showing the evanescent and plane waves regions is drawn in Fig. A.3. A loss of information is thus inevitable when considering light propagation from near-field to far-field, and hence an intrinsic resolution limit is imposed. The general heuristic in near-field optics is to increase the bandwidth of the reciprocal space of a given optical system by collecting as much near-fields as possible.

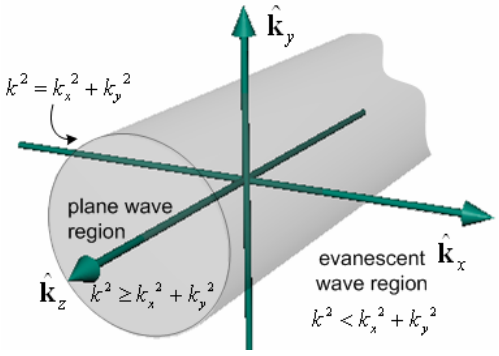

Figure A.3 – Reciprocal space.

A.4 Beyond the Resolution Limits: Subwavelength Fields

In a typical imaging system, light emitted from a point on a sample under illumination is mapped onto a screen by an electromagnetic impulse response described by the point spread function [A.1, A.6]. Asking how closely two points on the object plane can be distinguished is trying to determine how well two of such point spread responses overlap on the image plane. From the uncertainty principle, the minimum resolvable distance on the object plane $\Delta r_t = (\Delta x^2 + \Delta y^2)^{1/2}$ is related to the bandwidth of the optical system $\Delta k_t = (\Delta k_x{}^2 + \Delta k_y{}^2)^{1/2}$ by

$$\Delta r_t \, \Delta k_t \geq 1 . \tag{A.10}$$

In far-field optics, where only the contributions from the propagating plane waves are collected, a stringent limit is set. According to Abbe, the diffraction limit of light through a circular aperture with an Airy response is [A.4]

$$\min\{\Delta r_t\} = 0.6098 \frac{\lambda}{NA} \tag{A.11}$$

where λ and NA denote respectively the wavelength of illumination and the numerical aperture of the system. The situation is depicted in Fig. A.4, where two Airy discs are shown.

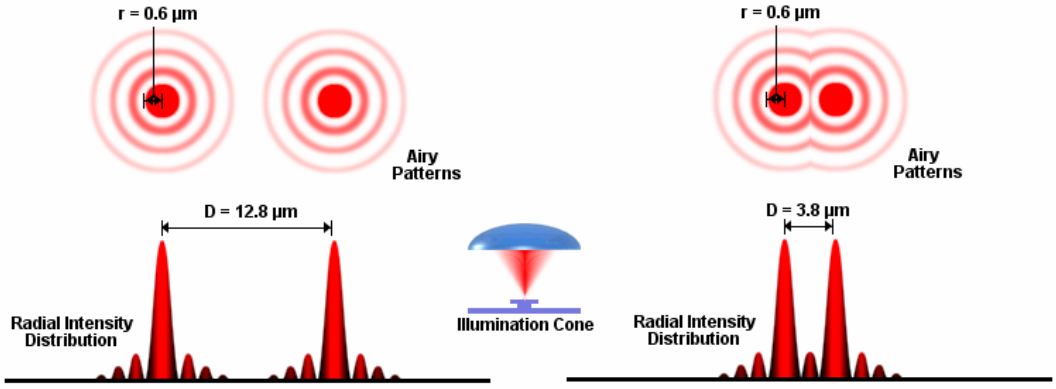

Figure A.4 – Overlap of point spread functions. Image obtained from [A.7].

As a rule of thumb, it is difficult to resolve light smaller than half of its wavelength using traditional far-field approach. Nonetheless, near-fields optics can be used as a remedy. In principle, by increasing the bandwidth (by retaining more evanescent fields) it is possible to achieve a better spatial resolution. This can be seen

from the inequality (A.10): if the bandwidth Δk_t can be significantly extended, the minimal distance between two resolvable points Δr_t can decrease. There are many tricks to achieve better resolution, such as near-field scanning microscopy techniques [A.1, A.7]. We restrict ourselves in this work only to local fields enhanced by a plasmon resonance phenomenon. In fact, recent advances in nanofabrication and nanotechnology have made possible the controlled deposition of metallic thin films and synthesis of self-assembled metallic nanoparticles buried in dielectrics. It is therefore desirable to use these recent techniques to go beyond the diffraction limit of light and allow the use of plasmonic effects to confine optical fields at the subwavelength nanometer scale. This sub-area of nanophotonics brings new exciting applications. For a survey of nanophotonic applications, please refer to [A.1, A.8].

A.5 References

[A.1] L. Novotny and B.Hecht, *Principles of Nano-Optics* (University Press, Cambridge, 2006).

[A.2] M. Ohtsu, H. Hori, *Near-Field Nano-Optics: From Basic Principles to Nano-Fabrication and Nano-Photonics* (Springer, 1999)

[A.3] T.-C. Poon, T. Kim, *Engineering Optics with Matlab* (World Scientific Publishing Company, 2006).

[A.4] B.E.A. Saleh, M.C. Teich, *Fundamentals of Photonics*, 2nd ed. (Wiley-Interscience, 2007)

[A.5] J.W. Goodman, *Introduction to Fourier Optics*, 3rd ed. (Roberts & Company Publishers, 2004)

[A.6] E.L. O'Neill, *Introduction to Statistical Optics* (Dover Publications, 2004)

[A.7] "Olympus FluoView Resource Center: Airy Patterns and Rayleigh Criterion", http://www.olympusfluoview.com/java/rayleighdisks/index.html

[A.8] A.V. Zayats and I.I. Smolyaninov, "Near-field photonics: surface plasmon polaritons and localized surface plasmons," *J. Opt. A: Pure Appl. Opt.*, vol. 5, pp. 16-50, 2003.

Appendix B – Permittivity from Measurements

Wavelength	Gold (Au)		Silver (Ag)		Copper (Cu)	
λ [nm]	ε'	ε''	ε'	ε''	ε'	ε''
1216	-66.219	5.701	-77.925	1.589	-67.750	7.915
1088	-51.050	3.861	-60.760	0.624	-51.955	5.196
985	-40.274	2.794	-48.886	0.559	-41.127	4.109
893	-32.041	1.925	-39.840	0.505	-33.180	3.461
822	-25.811	1.627	-32.797	0.458	-26.765	2.694
757	-20.610	1.272	-27.478	0.315	-21.705	2.239
705	-16.818	1.067	-23.405	0.387	-17.638	1.766
660	-13.648	1.035	-20.095	0.448	-13.992	1.649
617	-10.662	1.374	-17.236	0.498	-10.182	1.923
583	-8.113	1.661	-14.882	0.386	-6.822	3.786
549	-5.842	2.111	-12.856	0.430	-5.601	5.257
521	-3.946	2.580	-11.046	0.332	-5.409	6.155
496	-2.278	3.813	-9.564	0.309	-5.086	6.256
472	-1.703	4.844	-8.229	0.287	-4.603	6.208
451	-1.759	5.283	-7.058	0.213	-4.208	5.945
431	-1.692	5.649	-6.060	0.197	-3.751	5.763
414	-1.702	5.717	-5.173	0.228	-3.232	5.650
398	-1.649	5.739	-4.282	0.207	-2.735	5.586
382	-1.605	5.644	-3.472	0.186	-2.413	5.440
368	-1.401	5.609	-2.741	0.232	-2.051	5.372
355	-1.232	5.598	-2.004	0.284	-1.794	5.250
343	-1.310	5.538	-1.285	0.320	-1.625	5.070
332	-1.355	5.574	-0.658	0.282	-1.520	4.880
321	-1.231	5.846	0.502	0.635	-1.275	4.921
311	-1.243	5.793	0.897	1.392	-1.085	4.772
301	-1.227	5.780	0.866	2.584	-0.859	4.701

Table B.1 – Tabulated values of permittivity from optical measurements for three metals (gold, silver and copper) around the optical and near-infrared ranges [B.1].

References

[B.1] P.B. Johnson and R.W. Christy, "Optical constants of the noble metals," *Phys. Rev. B*, vol. 6, pp. 4370-4379, 1972.

Appendix C – Custom-Made Mechanical Pieces

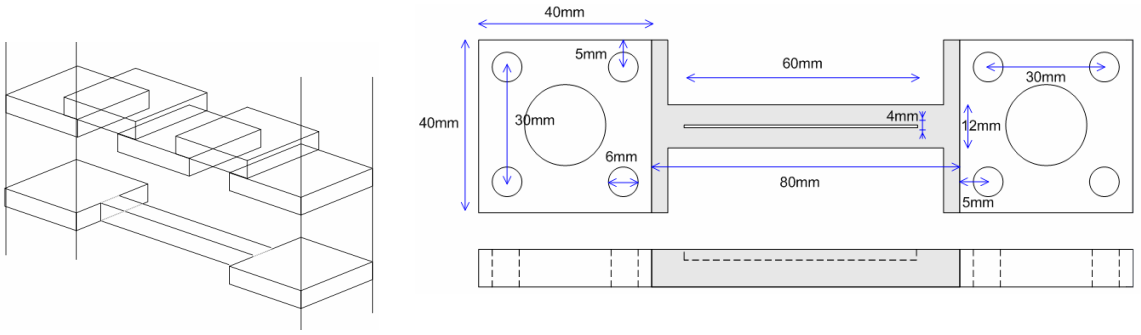

Figure C.1 – The mechanical support that holds the prism, grating and sample holder tight together using conventional cage plates (a) the whole support (b) the custom-made gray part holds the bottom of the equilateral prism.

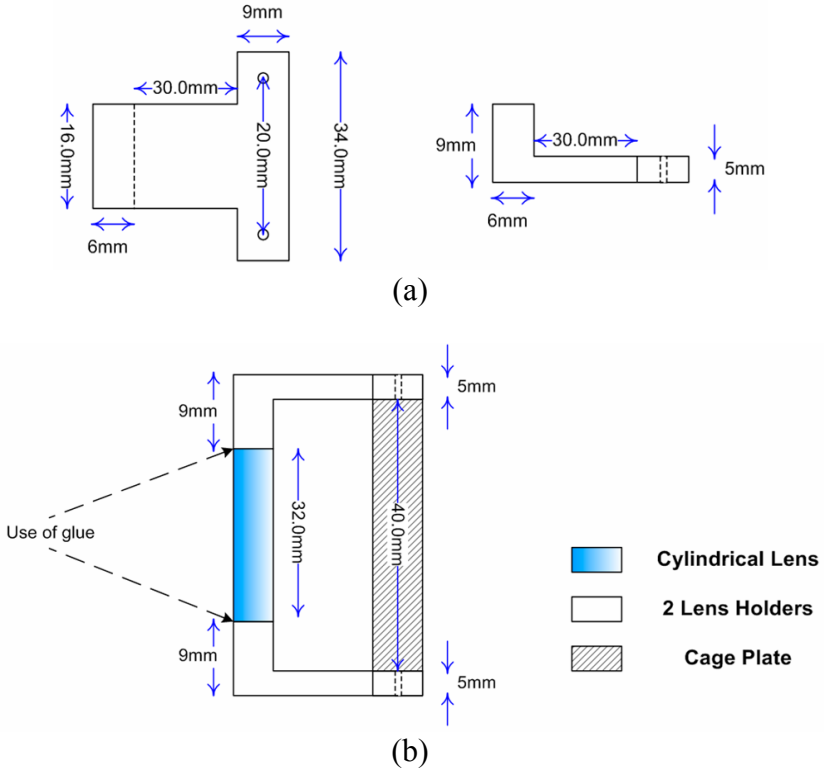

Figure C.2 – The cylindrical lens holder: (a) the custom-made piece on the sides of cylindrical lens (b) assembled pieces.

Appendix D – Plots of $\tau_{nm}(\theta)$ and $\pi_{nm}(\theta)$ up to $N=5$

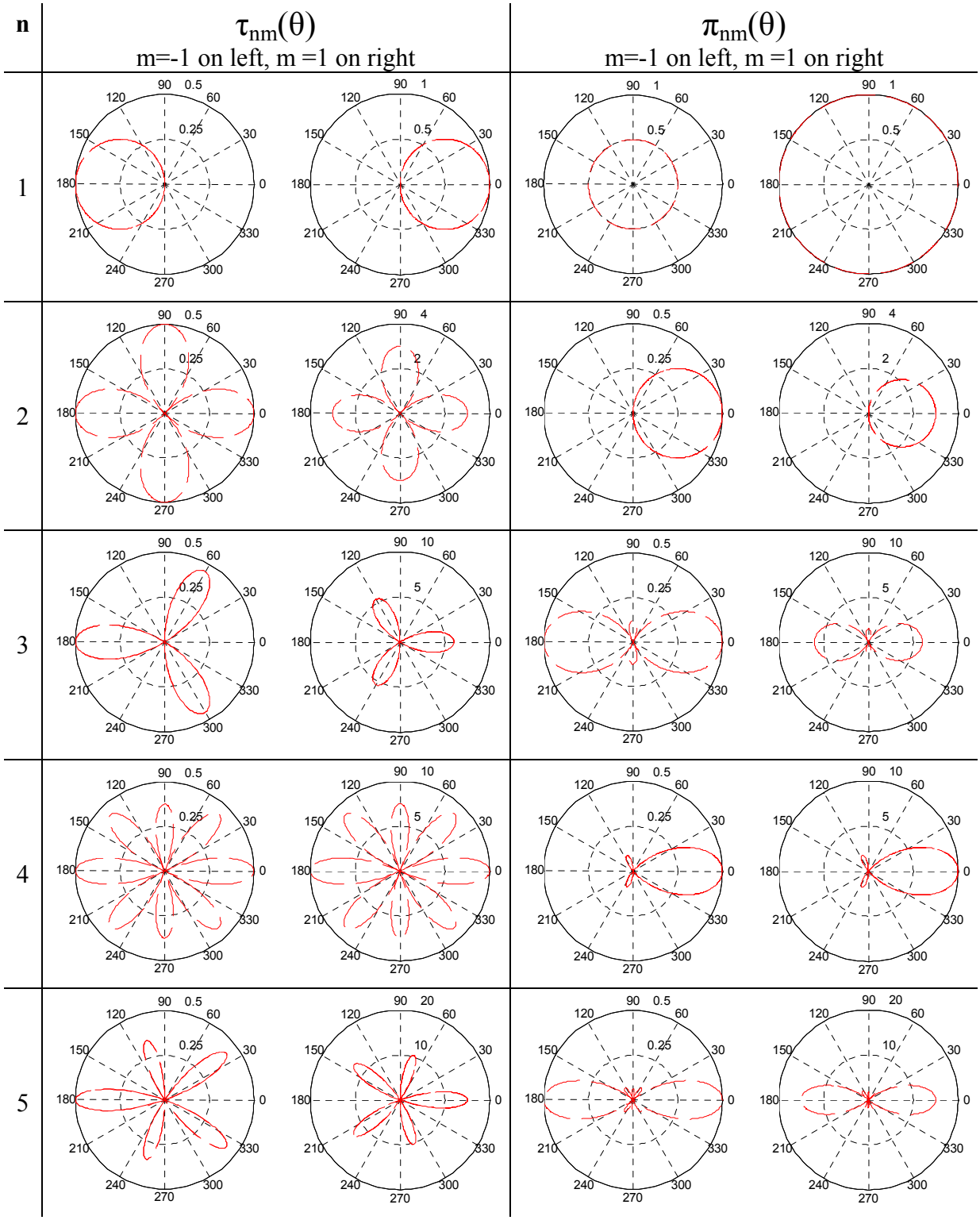

Figure D.1 – Polar plots of the functions $\tau_{nm}(\theta)$ and $\pi_{nm}(\theta)$. They provide the angular radiation patterns. The orders n are indicated on the left. The maximum order is $N=5$.